

Indiana State University
Sycamore Scholars

[All-Inclusive List of Electronic Theses and Dissertations](#)

2024

**Pleistocene Nutrient And Sediment Burial In The Agulhas Current:
Links To Regional And Global Climate Variability**

Paige Havener
Indiana State University

Follow this and additional works at: <https://scholars.indianastate.edu/etds>

Recommended Citation

Havener, Paige, "Pleistocene Nutrient And Sediment Burial In The Agulhas Current: Links To Regional And Global Climate Variability" (2024). *All-Inclusive List of Electronic Theses and Dissertations*. 2024.
<https://scholars.indianastate.edu/etds/2024>

This Dissertation is brought to you for free and open access by Sycamore Scholars. It has been accepted for inclusion in All-Inclusive List of Electronic Theses and Dissertations by an authorized administrator of Sycamore Scholars. For more information, please contact dana.swinford@indstate.edu.

**PLEISTOCENE NUTRIENT AND SEDIMENT BURIAL IN THE AGULHAS
CURRENT: LINKS TO REGIONAL AND GLOBAL CLIMATE VARIABILITY**

A Thesis

Presented to

The College of Art and Sciences

Department of Earth and Environmental Systems

Indiana State University

Terre Haute, Indiana

In Partial Fulfillment

of the Requirements for the Degree

Master of Science

by

Paige Havener

August 2024

© Paige Havener 2024

Keywords: Pleistocene, Agulhas Current, Southern Africa, Paleoclimate, Phosphorus, Biogeochemistry

COMMITTEE MEMBERS

Committee Chair: Jennifer C. Latimer, PhD

Chair and Professor, Department of Earth and Environmental Systems
Indiana State University

Committee Member: Jeffery R. Stone, PhD

Professor, Department of Earth and Environmental Systems
Indiana State University

Committee Member: Chad L. Yost, PhD

Assistant Professor, Department of Earth and Environmental Systems
Indiana State University

ABSTRACT

The Agulhas Current is one of the strongest currents in the southern hemisphere and is responsible for the transport of waters along the southeastern coast of Africa. The sediment load of the Agulhas Current and its interactions with other water masses in the region are essential to primary productivity along Africa's southern coast. Despite this importance, there are still many discrepancies in our understanding of how sediment burial and nutrient variability have been impacted by regional and global changes in climate. The focus of this research is to explore the connections between climate and elemental burial from the Pleistocene through the Holocene, with an emphasis on phosphorus and metal burial over the last 1.1 mya.

Two ocean sediment cores from the International Ocean Discovery Program (IODP) Expedition 361 were selected based on their proximity to the Agulhas Current. Site U1474 lies within the flow of the current, while Site U1479 lies within the Agulhas Ring Corridor, outside of its direct influence. Different downcore elemental concentrations were collected using a combination of X-Ray Fluorescence (XRF) and UV-Visible Spectroscopy. Site U1474 displayed strong dependence on southeastern African hydroclimate changes and orbital eccentricity. Site U1479 also displayed dependence on these processes, in addition to changes in the strength of Agulhas Leakage and glacial-interglacial variability. Additionally, we explore the teleconnections between both core sites and how processes upstream can affect productivity and terrigenous burial dynamics downstream.

ACKNOWLEDGEMENTS

First and foremost, I would like to thank my advisor, Dr. Latimer, for her endless support and encouragement over the last two years. I would not have completed this project or learned as much as I did without your guidance. I am also eternally grateful for the support of my other two committee members, Dr. Stone and Dr. Yost. Both of you have helped me grow tremendously as a student and as a person inside and outside of the classroom.

I would be nowhere without the help of my labmates in the biogeochemistry lab. We have spent countless hours cleaning dishes, analyzing samples, and agonizing over data together, and I am so grateful to have worked with such a wonderful group of people. I want to extend a massive thank you especially to Destiny Legg, for your help last summer with my total P data collection. Your help was instrumental to my project, and I can never repay you for everything you did. Outside of the lab, I am very grateful for each and every member of the EES department, with whom I have shared so many incredible experiences with. You welcomed me into a community, and I am forever grateful to you all.

Some of the most important people in my life live back home in New York and have encouraged and supported me every step of this journey. Thank you especially to Sammy, Josh, Emily, Teak, Gav, Jack, Lila, and the rest of NASA. You all have been here through so many ups and downs, from the day I made the decision to apply for a Master's program through to my graduation. I could never have done any of this without you.

Finally, and most importantly, I am forever grateful to my parents, my family, and my other loved ones for helping me through this entire crazy chapter of my life. You lift me up and inspire me to keep going every day.

TABLE OF CONTENTS

ABSTRACT	iii
ACKNOWLEDGEMENTS	iv
LIST OF TABLES	vii
LIST OF FIGURES	viii
INTRODUCTION	10
The Agulhas Current.....	10
Expedition 361 - Sites U1474 and U1479	12
Southeast African bedrock geology, river systems, and climate	14
Ocean nutrients and the marine phosphorus cycle.....	20
RESEARCH QUESTIONS AND OBJECTIVES	23
METHODS	25
Core descriptions and sample age calculations.....	25
Initial sample preparation and preliminary XRF analysis	26
Total phosphorus preparation and analysis.....	27
Sequential phosphorus extraction and analysis.....	28
Data Analysis	29
Data Accuracy.....	30
RESULTS – U1474	32
XRF analysis results	32
Total P and Sequential P analysis results.....	36
Elemental ratio data	40
Correlation coefficients.....	44
PCA and GAM results	46
Spectral analysis.....	50
RESULTS – U1479	51
XRF analysis results	51

Total P and Sequential P analysis results.....	54
Elemental ratio data	58
Correlation Coefficients.....	58
PCA and GAM Analysis.....	61
DISCUSSION	63
Downcore comparisons, U1474 and U1479	63
Elemental burial variability: potential causes, mechanisms, and implications.....	65
Site U1474 and the Natal Bight	66
Site U1479 and the Agulhas Leakage	70
CONCLUSIONS.....	80
REFERENCES	82
DATA APPENDICES	95
Appendix A – U1474 XRF and P _{TOT} data, full record.....	95
Appendix B – U1479 XRF and P _{TOT} data, full record.....	103
Appendix C – U1474 P _{EXT} data, 500 kya	113
Appendix D – U1479 P _{EXT} data, 500 kya	116

LIST OF TABLES

Table 1: Sequential P extraction steps	29
Table 2: Descriptive statistics of select XRF data, U1474	33
Table 3: Descriptive statistics of P data, U1474	37
Table 4: Pearson correlation coefficients, 1110 to 0.5 kya, U1474	45
Table 5: Change in Pearson correlation coefficients, U1474	46
Table 6: Descriptive statistics of select XRF data, U1479	52
Table 7: Descriptive statistics of P data, U1479	55
Table 8: Pearson correlation coefficients, 1112 to 0.8 kya, U1479	60
Table 9: Change in Pearson correlation coefficients, U1479	61

LIST OF FIGURES

Figure 1: Site map, IODP Expedition 361	12
Figure 2: Major river configurations of southern Africa.....	20
Figure 3: Shipboard age models, U1474 and U1479	26
Figure 4: XRF and P _{TOT} box and whisker plots, U1474 and U1479	34
Figure 5: XRF and P _{TOT} concentrations, U1474	35
Figure 6: Detailed P geochemistry plots, U1474.....	38
Figure 7: Fraction of P _{TOT} by sequential extraction step, U1474	39
Figure 8: Select XRF ratio comparison plots, U1474 and U1479	41
Figure 9: Select P _{TOT} and elemental ratio comparison plots, U1474 and U1479	42
Figure 10: Detrital P/Zr ratio plots, U1474 and U1479	43
Figure 11: U1474 PCA data report and biplot	47
Figure 12: PC1 score plots, U1474 and U1479	48
Figure 13: GAMs of PC1 score plots, U1474 and U1479	49
Figure 14: REDFIT Analysis of U1474 PC1	50
Figure 15: XRF and P _{TOT} concentrations, U1479	53
Figure 16: Detailed P geochemistry plots, U1479	56
Figure 17: Fraction of P _{TOT} by sequential extraction step, U1479	57
Figure 18: U1479 PCA data report and biplot	62
Figure 19: P _{TOT} comparison plots, U1474 and U1479	65
Figure 20: Southern African hydroclimate and insolation curves, U1474	69
Figure 21: Agulhas leakage and ocean overturning strength links, from Caley et al. (2012)....	77

Figure 22: XRF and P data with glacial period correlations, U1479 78

Figure 23: Timeline of changes at site U1479 79

CHAPTER 1

INTRODUCTION

The Agulhas Current

The Agulhas Current, located in the Indian Ocean, is the strongest western boundary current in the Southern Hemisphere (Figure 1; Hall, Hemming, LeVay et al., 2017c). The Agulhas Current transports approximately 70 Sv (1 Sverdrup = $1 \times 10^6 \text{ cm}^3 \text{s}^{-1}$) of warm, highly saline tropical surface waters from the Mozambique Channel along the continental shelf towards the cape of Africa (Beal & Bryden, 1999; Lutjeharms, 2007). The Agulhas Current can be broken up into two distinct sections, the northern and southern currents, which differ from each other based on their flow characteristics (Lutjeharms, 2007). Once the current reaches the southern cape of Africa, it retroflects and turns east, forming the southern border of the Indian Ocean (Lutjeharms, 2007).

At its retroflection point, the Agulhas Current sheds rings of water into the Atlantic at a rate of roughly 21.3 Sv annually, called the Agulhas Leakage (Fig. 1; Daher et al., 2020; van Leeuwen et al., 2000). This salt leakage is thought to have a profound effect on Atlantic Meridional Overturning Circulation (AMOC) and potentially served to “jump start” thermohaline circulation during times where AMOC had significantly slowed due to glacial and interglacial changes (Dyez et al., 2014; Marino et al., 2013; Simon et al., 2013). The Agulhas Leakage itself also varies on glacial-interglacial and longer timescales, likely due to the periodic latitudinal migration of the Subtropical Front (STF) and Antarctic Polar Front (APF) (Bard & Rickaby, 2009; Biastoch et al., 2008; Caley et al., 2012; Cartagena-Sierra et al., 2021; Simon et

al., 2013; Turney & Jones, 2010). This variation is known to have a strong influence on southern African weather and climate systems (Babin, 2023; Castañeda et al., 2016; Dupont et al., 2011, 2022; Hall, Hemming, LeVay et al., 2017c; Lutjeharms, 2007).

Below the surficial Agulhas Current is the Agulhas Undercurrent, which transports North Atlantic Deep Water (NADW) at depth also along the southern coast of Africa and into the Atlantic basin (Hall, Hemming, LeVay et al., 2017c; Lutjeharms, 2007). The Agulhas Current encounters many areas of localized upwelling along its course, though the current itself is known to be low in nutrient content (Lutjeharms, 2007). Persistent upwelling occurs at the headwaters of the current near Port Elizabeth, South Africa, while wind-driven instances of upwelling occur in areas where the shape of the coastline allows for it (Lutjeharms, 2007; Schumann, 1982). The Agulhas Current also experiences a phenomenon known as Natal Pulses, which are large meanders beginning in the Natal Bight that then flow southwest along the coast and create cold water eddies close to the coast that cause upwelling (Goschen et al., 2015; van Leeuwen et al., 2000). These pulses occur between 1 and 6 times per year and can influence the ocean climate of the Agulhas Bank for up to 110 days (Krug et al., 2014). This study will look at two different core sites within the Agulhas Current, one from the Agulhas Leakage and one from the Natal Bight (Fig. 1).

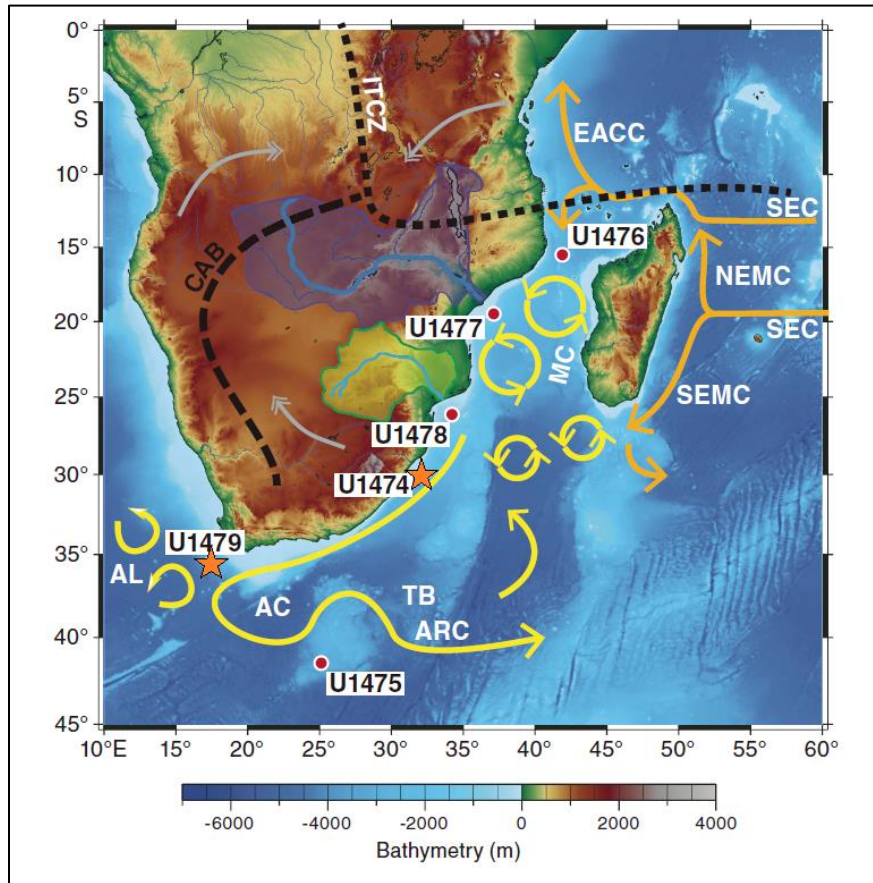


Figure 1: Site Map, IODP Expedition 361 Map of sites studied by IODP Expedition 361 and their relative proximities to the Agulhas Current and other main currents of the southwest Indian Ocean. Orange stars denote the locations of sites U1474 and U1479 used in this research. AC=Agulhas Current, SEC=South Equatorial Current, SEMC= Southeast Madagascar Current, NEMC= Northeast Madagascar Current, EACC= East Africa Coastal Current, TB=Transkei Basin, ARC= Agulhas Return Current, AL= Agulhas Leakage, ITCZ=Intertropical Convergence Zone, CAB=Congo Air Boundary. Adapted from Hall, Hemming, LeVay et al., 2017c.

Expedition 361 - Sites U1474 and U1479

International Ocean Discovery Program (IODP) Expedition 361 recovered sediment cores from the southern African continental margin between January 30 and March 31, 2016 (Hall, Hemming, LeVay et al., 2017c). Six sites were selected for the expedition covering the full extent of the Agulhas Current, from the Mozambique Channel to the return section along the southeastern boundary of the Indian Ocean (Fig. 1). The objectives of the expedition were to (i)

explore the influence of the Agulhas Current on the climate changes experienced during the Pliocene-Pleistocene, with specific focus on its effect on Indian-Atlantic gateway circulation, (ii) address how AMOC and the Agulhas Current are connected, and (iii) to look at the influence of the Agulhas Current on African continental climate dynamics (Hall, Hemming, LeVay et al., 2017c).

For the research proposed here, samples from sites U1474 and U1479 were analyzed. Site U1474 is in the most northern part of the Natal Valley at a water depth of 3034 m (Fig. 2; Hall, Hemming, LeVay et al., 2017b). This region of the ocean is supplied with sediment primarily from the nearby Tugela River, as well as the more distant Limpopo and Zambezi River systems to the north (Babin, 2023; Hall, Hemming, LeVay et al., 2017b). Site U1474 is of interest because of its proximity to the headwaters of the Agulhas Current and the previously mentioned major rivers in southeastern Africa. Site U1474 is also in an ideal location to detect changes in continental African climate over time.

Site U1479 is located at the retroflection point of the Agulhas current and within the Agulhas ring corridor, at a water depth of 2615 m (Hall, Hemming, LeVay et al., 2017b). Near U1479, the Agulhas sheds ~400 km wide rings of warm, saline surface water as it turns back on itself from the Indian Ocean into the Atlantic, with the potential to greatly influence climate in the region (Hall, Hemming, LeVay et al., 2017b). This region also lies within the transport zone of NADW from the Atlantic into the Southern and Indian Oceans. The interactions of these powerful rings of warm, saline-rich but nutrient-depleted waters with the cold, nutrient-rich waters of the Benguela Current and NADW cause complex mixing along the Agulhas Bank region, leading to upwelling and high productivity off the cape of South Africa today (Hutchings

et al., 2009; Lutjeharms, 2007; Lutjeharms et al., 2000). It is because of this mixing and the intricate interactions between these water bodies that this site was chosen for this study.

Though the two core sites are separated by approximately 1,500 km, they are strongly connected today by both the transport dynamics of the current and the formation of Natal Pulses. Agulhas ring formation has been shown to be heavily influenced by pulse formation in the Natal Bight, which causes the Agulhas Current to retroreflect early and increases leakage from the Indian to the Atlantic Ocean (Schubert et al., 2021; van Leeuwen et al., 2000). Additionally, studies have shown that riverine sediments entering the Agulhas Current system near the Natal Bight have the capacity to be transported through the Agulhas Leakage and into the Cape Basin in the Atlantic Ocean, thousands of kilometers away (Franzese et al., 2006, 2009). Because of this teleconnection between the Natal Bight and the Agulhas Leakage corridor, it is logical to conclude that changes to the strength or flow of the current, its sediment supply, or climate of the adjacent southeast African continent near Site U1474 would also cause changes near Site U1479. For these reasons, both sites were selected for study here, and their similarities and differences in downcore biogeochemistry were explored in depth.

Southeast African bedrock geology, river systems, and climate

Southern Africa is a geologically and climatically diverse region. Records of climate and vegetation variability from the area indicate a close relationship with glacial/interglacial cycles and other drivers of long-term variability (Dupont et al., 2011; Hahn et al., 2018; Scott & Neumann, 2018). Changes in the hydroclimate of southern Africa account for fluctuations in precipitation, and by extension erosion and sediment transport by rivers in the region both now and throughout the Quaternary. Thus, it is important to know the bedrock composition and sediment geochemistry of the catchments of the major rivers that feed into the Agulhas Current

upstream of the two study sites. Also, understanding both the present and past climate regimes that influence southern Africa is critical to this project, to help explore the patterns visible in our record through time. Next is a discussion of the river systems and their associated catchment bedrock geology composition, as well as the past and present climate regimes of southern Africa.

There are several river systems along the southeastern coast of Africa that discharge into the Mozambique Channel and Agulhas Current (Fig. 2). To the south, three primary rivers flow out of the Drakensberg Mountains, the minor Mfolozo and Mkumazi rivers and the major Tugela River (Babin, 2023). These three rivers are underlain by rocks in the Karoo Supergroup, which consist of glacial, fluvio-deltaic, and eolian deposits, capped by the extensive Drakensberg flood basalts and Jurassic-aged dolerites (Catuneanu et al., 2005; Hahn et al., 2018). The Tugela River transports approximately 7 MT of sediment per year to the Indian Ocean (Milliman & Meade, 1983).

In northeastern South Africa, the most influential river that drains into the Mozambique Channel is the Limpopo River, which is estimated to transport 33 MT of sediment per year (Fig. 2; Milliman & Meade, 1983). The dominant stratigraphic units that underly the Limpopo catchment are the Karoo Supergroup, the Mozambique coastal belt, and the Kaapvaal Craton (Hahn et al., 2018). The Mozambique coastal belt is composed predominantly of sedimentary rocks of marine origin, interspersed with eroded material that originated from Namaqua-Natal Belt metamorphic rocks (Hahn et al., 2018). Importantly, the Namaqua-Natal belt contains large deposits of titanium- and zirconium--bearing minerals, especially rutile, ilmenite, and zircon (Hahn et al., 2018). The Kaapvaal Craton contains Archean gneisses and granitoids, with a lesser volume of metamorphosed volcano-sedimentary rocks (Eglington & Armstrong, 2004).

The largest and most influential river in southern Africa is the Zambezi River. It drains roughly 44 MT of sediment into the Indian Ocean each year and cuts through a diverse group of geologic units (Fig. 2; Milliman & Meade, 1983). The primary geologic units the Zambezi overlays are the Zimbabwe Craton, the Kaapvaal Craton, the Lufilian Arc, the Zambezi Belt, and the Karoo Supergroup (Garzanti et al., 2021 and 2022). The Zimbabwe Craton consists of Archaean-aged high-grade metamorphic rocks, volcanic units, and conglomerates, and is flanked by greenstone belts (Garzanti et al., 2021). The Lufilian Arc is made up of Neoproterozoic low to high-grade metasedimentary and metaigneous rocks, and notably contain abundant deposits of copper, cobalt, uranium, lead, and zinc (Garzanti et al., 2022; John et al., 2004). The Zambezi Belt is predominantly made up of volcano-sedimentary rocks (Garzanti et al., 2021).

These are the primary rivers feeding into the Agulhas Current today; however, in the past there is evidence for local river outflow on the Agulhas Bank during glacial lowstands (Dingle & Rogers, 1972). The lower sea levels during glacial periods, especially following the Mid-Pleistocene Transition (MPT), allowed the rivers to become longer and wider and have higher rates of discharge (Dingle & Rogers, 1972). Sea level low stands also led to grassland and forest development on the bank (Dupont et al., 2011). During exposures, the Agulhas Bank is commonly referred to as the Paleo-Agulhas Plain (Dupont et al., 2011). The rivers that flow over the Paleo-Agulhas Plain flow over formations that are part of the Karoo Supergroup, namely a subgroup called the Bokkeveld Shales (Dingle & Rogers, 1972). When the Agulhas Bank is exposed, these rivers potentially provide additional sediment to the flow of the Agulhas Current that can be observed at Site U1479 but not Site U1474. Additionally, repeated exposures of this continental shelf during glacial cycles may lead to increased erosion and re-release of nutrients

and detrital material stored on the continental shelf. This is known as the Glacial Shelf-Nutrient Hypothesis (Filippelli et al., 2007).

Regarding climate, modern southern Africa has a wide array of climate regimes, with predominantly dry conditions prevalent on the eastern coast and wetter conditions on the western coast of the continent. These conditions, today and in the past, are strongly influenced by ocean-atmospheric exchanges of the Agulhas and Benguela Currents with the tropical easterly winds, as well as Walker Circulation patterns, the Southern Indian Ocean Dipole, and El-Niño Southern Oscillation (Babin, 2023; Hall, Hemming, LeVay et al., 2017c; Kaboth-Bahr et al., 2021). In most of South Africa, particularly in the east, the majority of rainfall occurs in the austral summer, while in the Cape Region, most rainfall occurs in the austral winter (Dupont et al., 2022). On the eastern coast of southern Africa, precipitation displays a north-south gradient, with high rainfall occurring in the Zambezi catchment and lower rainfall occurring in the Drakensberg Mountain-derived river catchments (Hahn et al., 2018). A stronger east-west dipole also exists in southern Africa. Today, humid conditions prevail on the east coast, while arid conditions prevail to the west (Hahn et al., 2018). Rainfall also decreases inwards from coastal regions, reflected by changes in vegetation from forests and C₃ plants to grasslands and savanna biomes towards the center of the continent in the Kalahari Desert region (Dupont et al., 2011, 2022; Hahn et al., 2018). Because of the east-west climate dipole, southwest Africa features two prominent deserts, the Namib on the west coast of Namibia and the Kalahari in South Africa, Botswana, and eastern Namibia. Additionally, the cape region is dominated by a Mediterranean-type climate regime (Hahn et al., 2018). Southern Africa is highly sensitive to changes in hydroclimate, reflected in pollen records from marine sediment cores off the coast (Dupont et al., 2011, 2022). Fluctuations can also be seen on glacial-interglacial timescales and on longer timescales in numerous

paleorecords (Caley et al., 2012, 2018; Castañeda et al., 2016; Dupont et al., 2022; Kaboth-Bahr et al., 2021).

The Pleistocene experienced several large-scale global changes in climate. Two of these are the MPT and the Mid-Brunhes Event (MBE). The MPT involves a shift in orbital cyclicity from an obliquity-dominated cycle to an eccentricity-dominated cycle (Imbrie et al., 1993). This switch began around 1.2 mya and was completed by 700 kya. Following the MPT, glacial cycles became longer and more intense, with larger ice sheet growth and major drops in global sea level (Imbrie et al., 1993). The Mid-Brunhes event began around 420 kya and is primarily characterized by increased variability in ice volume at the poles (Lisiecki & Raymo, 2005), higher CO₂ levels, and warmer temperatures during interglacials (Cartagena-Sierra et al., 2021). The effects of the MPT and the MBE are seen in many paleorecords from southern Africa and the Indian Ocean. These include evidence for generally drier conditions following the MBE in the southern hemisphere, grassland expansion especially in the interior of continental Africa, prolonged northward shifts of the STF that affected sea-surface temperatures and productivity in the southwestern Indian Ocean, and more prominent eccentricity and precession cyclicity in records (Ao et al., 2020; Babin, 2023; Bard & Rickaby, 2009; Cartagena-Sierra et al., 2021; Dupont et al., 2011).

A recent study by Babin (2023) explored sediments from U1474 in the Natal Bight using endmember modeling of clay ⁴⁰K/⁴⁰Ar provenance age and mineralogy. They estimated that the respective contributions of the Zambezi, Tugela, and Limpopo Rivers to the Natal Bight average 56%, 27%, and 17% (respectively) over the last 825 kya (Babin, 2023). This study suggests that changes in sediment provenance on longer than glacial-interglacial timescales is due to changes in southern African hydroclimate, which is driven by orbital precession (Babin, 2023). Other

records from the region have found strong relationships between climatological and biogeochemical processes in southern Africa and orbital cycles. Migrations in the Subtropical Front (STF) and the dynamics of the Agulhas Leakage over the last 1.1 mya have been linked to variations in obliquity and eccentricity, while southern African rainfall and hydroclimate is dominated by long-term eccentricity in addition to precession (Caley et al., 2011; Cartagena-Sierra et al., 2021; Dupont et al., 2022; Kaboth-Bahr et al., 2021).

Because rivers are the dominant sources of terrestrially-derived sediment to the Agulhas Current, it is important to understand variations in their individual inputs, the bedrock geology of their catchments, and how local, regional, and global climate change affect them over time. This study explored all these aspects and their potential influences on the geochemical records at Site U1474 and U1479.

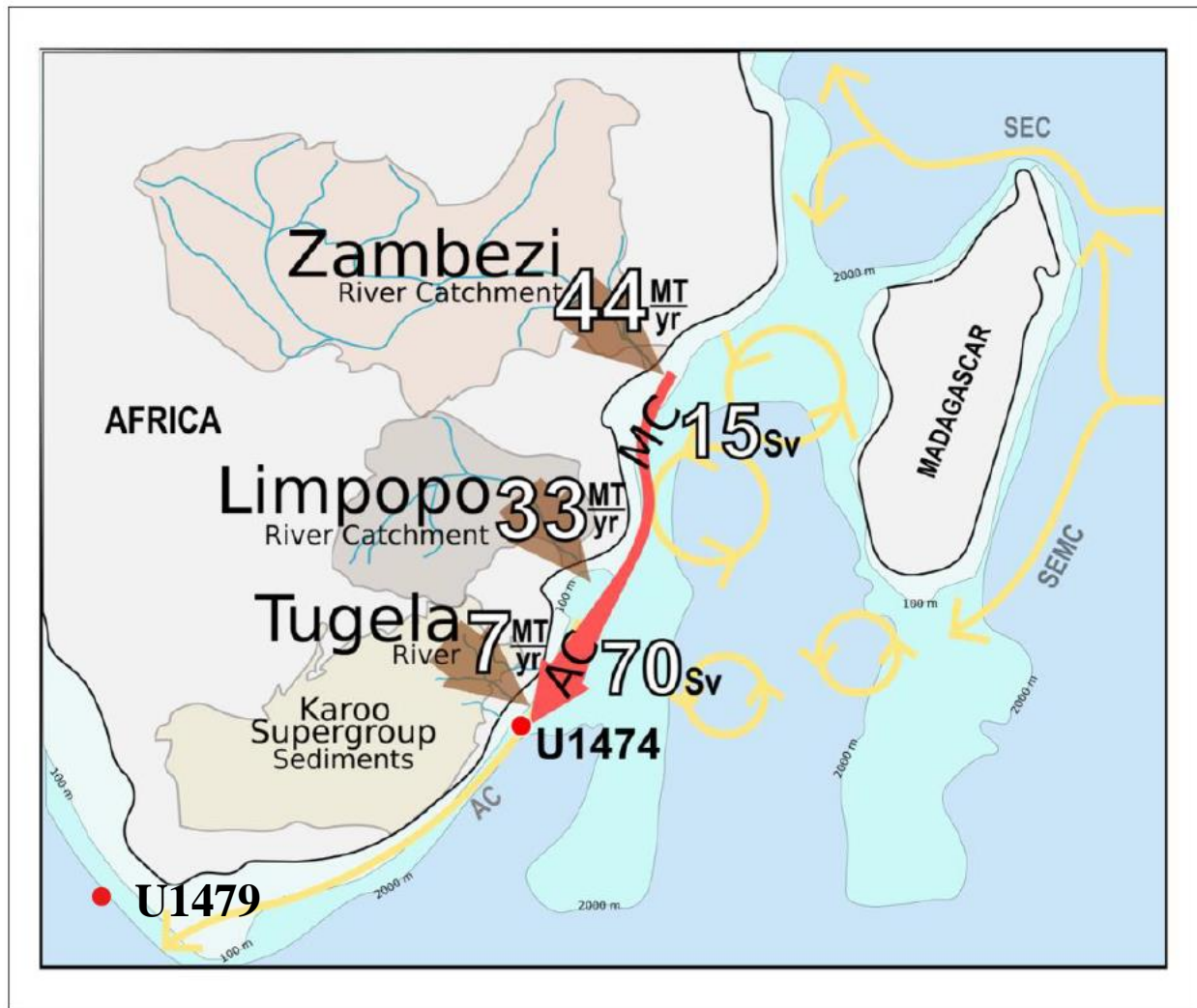


Figure 2. Major rivers, their catchment areas, and ocean current configurations of southern Africa. The approximate locations of U1474 and U1479 are denoted by red dots on the map. AC = Agulhas Current, MC = Mozambique Channel, SEC = South Equatorial Current, SEMC = Southeast Madagascar Current. Adapted from Babin (2023).

Ocean nutrients and the marine phosphorus cycle

The cycling of carbon (C) and essential macronutrients such as nitrogen (N) and phosphorus (P) constrain biological productivity and control how ecosystems are structured. In the oceans, the stoichiometric ratio of C:N:P (106:16:1) in phytoplankton links these three elements biogeochemically and is important to our understanding of how nutrient flux and

primary productivity are related to each other in the world's oceans over geologic timescales (Arrigo, 2005; Redfield, 1958). The Redfield ratio is also useful when considering what nutrients are considered limiting for the biosphere. Locally, nutrient limitation can be attributed to the availability of N, P, silicon (Si), or micronutrients like iron (Fe) (Tyrrell, 1999). On geologic timescales, however, many scientists believe that P acts as an ultimate limiting nutrient over N in both terrestrial and aquatic environments (Tyrrell, 1999). The weathering rate of apatite, the most significant P mineral, is slow on land, and limits the supply in marine settings (Benitez-Nelson, 2000; Paytan & McLaughlin, 2007; Tyrrell, 1999). The links that exist between the marine P and C cycles make P a useful proxy for the study of ocean primary productivity over time. Because of these links and its relatively simple cycle, P will be the primary nutrient studied in this project.

P is an essential building block for all living organisms, playing a critical role in DNA and RNA production and the transport of chemical energy through the ATP molecule, as well as in the formation of cell membranes, teeth, and bones (Paytan & McLaughlin, 2007). The marine P cycle, unlike other nutrient cycles, has very few input modes, limited almost entirely to riverine input of weathered continental material (Benitez-Nelson, 2000; Paytan & McLaughlin, 2007; Tyrrell, 1999). In the ocean, P can exist as dissolved or particulate P and as either organic or inorganic P (Benitez-Nelson, 2000; Paytan & McLaughlin, 2007). Uptake of P by microorganisms in the water column causes significant transformations of P (Defforey & Paytan, 2018; Duhamel et al., 2021; Paytan & McLaughlin, 2007). P recycling has been shown to take place rapidly and efficiently, so that even during times of low P availability, primary production rates can remain relatively high (Paytan & McLaughlin, 2007).

The main sink for P is via sediment burial; typically, as sinking organic matter incorporated in marine snow or fecal pellets (Benitez-Nelson, 2000; Paytan & McLaughlin,

2007). In the modern oceans, most P burial (>50%) takes place on continental margins and consists primarily of nonreactive, inorganic forms of P (Paytan & McLaughlin, 2007; Ruttenberg, 1993). In open ocean settings, the major component of P burial flux is reactive forms of P (Benitez-Nelson, 2000; Paytan & McLaughlin, 2007; Ruttenberg, 1993).

Reactive P in sediments is P that was either once bioavailable or was associated with biologically-related P components in the water column prior to burial, while nonreactive P is composed of detrital terrigenous material (Paytan & McLaughlin, 2007; Ruttenberg, 1993). Phosphorus associated with organic matter can undergo several transformations both prior to and during burial and diagenesis. This organic-associated P can become associated with Fe and manganese (Mn) oxide and oxyhydroxides, be adsorbed, or remineralize as authigenic carbonate fluorapatites (CFAs) and other phosphate minerals (Filippelli et al., 2007; Latimer et al., 2006b; Paytan & McLaughlin, 2007; Ruttenberg, 1993; Ruttenberg & Berner, 1993). Total reactive P, the sum of organic-associated P, authigenic P, adsorbed P, and oxide-associated P, can be used to evaluate burial of what was once organic P and its relationships with export production and nutrient utilization over time (Filippelli et al., 2007; Latimer et al., 2006b).

CHAPTER 2

RESEARCH QUESTIONS AND OBJECTIVES

The goal of this research is to determine how nutrient and associated elemental burial varied over the last 1 mya in the Indian Ocean, and what relationships exist between southern African continental climate trends and those seen in the marine records. There are three main questions we hope to answer:

1. How did nutrient and associated elemental burial vary over the last 1.1 mya in the western Indian Ocean?
2. What relationships exist between global climate trends and the patterns seen in these marine records?
3. What relationships exist between southern African continental climate trends and the patterns seen in these marine records?

To answer question 1, sedimentary P data was collected and analyzed to characterize P burial through time in the headwaters and retroflection point of the Agulhas Current, and how the two regions differ from each other. Additional geochemical proxy and indicator data was collected and used in conjunction with this P data, to determine other key processes such as export production and terrigenous provenance. To answer questions 2 and 3, the collected downcore elemental concentration and ratio data is compared with existing continental and marine paleoclimate records from the region. The purpose of these statistical analyses is to understand how biogeochemical cycling in the Agulhas influenced and was influenced by variations in the climate of southern Africa, and how the modern teleconnections seen between the headwaters and leakage of the Agulhas Current varied over much of the Quaternary.

Some hypotheses related to these questions are:

1. Export production (organic matter fixed by photosynthesis) was consistently higher in U1479 than U1474 over the last 1.1 mya, but continental sediment influx was consistently higher in U1474 than U1479.
2. Orbital cycle variability strongly influenced nutrient and associated elemental cycling in the Agulhas Current over the last 1.1 mya.
3. U1479 and U1474 may not always have been affected by strong teleconnections and may have even been disconnected during glacial lowstands, accounting for differences in each record.

Nutrient and metal cycling is still poorly understood for the Agulhas Current, especially over long timescales. The answers to these questions will help bridge these gaps in understanding.

CHAPTER 3

METHODS

Core descriptions and sample age calculations

For this study, samples from IODP Expedition 361 sites U1474 (n=421) and U1479 (n=301) were analyzed. Site U1474's sediments are composed of terrigenous clay and biogenic material, while the sediments at site U1479 are dominated by calcareous ooze, interspersed sparsely with thin layers of very fine sand (Hall, Hemming, LeVay et al., 2017a and 2017b). The composite core for Site U1479 is approximately 239 m long. Sampling intervals for this study averaged 14 cm for the top 57 m of core and 9 cm (higher temporal resolution) for the last 500 kya of the core. The average sedimentation rate was estimated to be 5.3 cm/kya (Figure 3b; Hall, Hemming, LeVay et al., 2017b). The age model used in this study is based on $\delta^{18}\text{O}$ stratigraphy (Charles, 2024). The composite core for Site U1474 is ~ 254 m long with an average sample resolution of 14 cm for the top 40.5 m of core. This section of core represents approximately 1.1 mya and has an average sedimentation rate of 3.7 cm/kya, according to the shipboard age model (Figure 3a; Hall, Hemming, LeVay et al., 2017a). A refined age model has not yet been completed for U1474; therefore, the original shipboard age model was used for this study. Each sample at U1479 represents ~190 years of material, and each sample of U1474 represents ~270 years of material. Sample ages were calculated from their respective age models and sample top depth in the composite cores using the simple cubic spline Interpolate/Extrapolate Y from X tool in OriginPro (*OriginPro*, 2024)

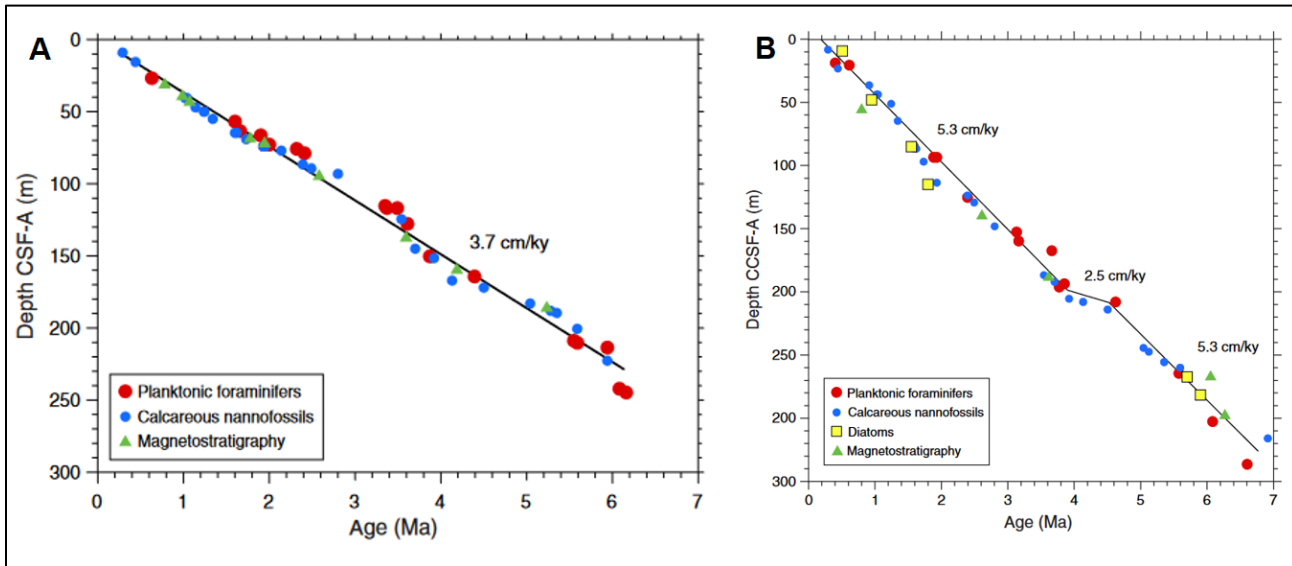


Figure 3. Shipboard Age models, Site U1474 (A) and Site U1479 (B), IODP Expedition 361.

Age-depth relationships for both are based upon planktonic foraminifers, calcareous nannofossils, diatoms, and magnetostratigraphic boundaries. **A)** Regression lines are a linear fit to all data and forced through the origin, indicating a sedimentation rate of 3.7 cm/kya. Adapted from Hall, Hemming, LeVay et al. (2017a). **B)** Line segment fits are interpretive, with the younger two segments based on foraminifera ages and the older based on all chronostratigraphic datums combined. Adapted from Hall, Hemming, LeVay et al. (2017b).

Initial sample preparation and preliminary XRF analysis

During sample preparation, core samples were dried at 70°C for 24 hours then powdered and homogenized to <106 µm using an agate mortar and pestle. Elemental concentrations were determined using a portable ThermoScientific Niton XL3t Gold+ XRF analyzer. To ensure analytical accuracy, standard reference material (SRM) National Institute of Standards and Technology (NIST) 1646a (estuarine sediment) was analyzed three times at the start of each round of testing and again every 15 samples. The elements targeted in this XRF analysis were Fe, titanium (Ti), calcium (Ca), potassium (K), and zirconium (Zr). Ti, K, and Zr are used as proxies for terrigenous material input (Delany et al., 1967). Because the carbonate-rich component of the sediments are almost entirely composed of calcareous nannofossils, Ca is used in our study as a proxy for surface ocean biomass changes. Fe and K in marine sediments are

also commonly used terrigenous material indicators, and can be combined with other elements to assess weathering rates on land (Böning et al., 2007; Galvão et al., 2023). Using this bulk data, ratios such as Ti/Zr and Ti/Ca were calculated and will be used to evaluate changes in terrigenous provenance, to assess dissolution within the cores, and to observe variability in CaCO₃ content in the sediments (Gottschalk et al., 2018; Latimer, et al., 2006a). Additionally, the P/Ti ratio is a proxy for export production, and thus looks at changes in P burial (Filippelli et al., 2007). The P/Ti ratio is also useful because it is not as strongly impacted by sediment focusing as P accumulation rates (Flores et al., 2012).

Total phosphorus preparation and analysis

Total phosphorus concentrations for U1474 and U1479 were analyzed using a Shimadzu UV-1900i UV-Visible Spectrophotometer following extraction with 2M HCl. Approximately 0.1g of sediment was weighed into porcelain crucibles and ashed in a muffle furnace at 550°C for 2 hours to remove organic material. The samples were reacted with 10 mL of 2M HCl in new 15 mL polyethylene centrifuge tubes, shaken for 16 hours, and centrifuged. In addition to the core samples, SRM NIST 1646a and random duplicates of the core samples were prepared every 23 samples for quality assurance. Acid blanks were also prepared for each sample batch for later dilution and determination of analytical detection limits.

Prior to analysis, the samples were diluted in nanopure water and reacted with 1 mL of Color Developing Reagent (CDR), created using the molybdate blue method outlined by Strickland & Parsons (1972). Phosphorus standards were made for each batch of 46 samples at a dilution of 1:10 and at concentrations of 0 µM, 2 µM, 4 µM and 8 µM. Total P concentrations were measured at a wavelength of 880 nm.

Sequential phosphorus extraction and analysis

Sequential phosphorus extractions were completed following the methods outlined in Anderson & Delaney (2000) and Ruttenberg (1992) to separate out four major sedimentary components of P for analysis (Table 1). The reactive component of P is the sum of the step I, II, and IV, while the remaining nonreactive P is the detrital component (step III). Approximately 0.1 g of dried and powdered samples were weighed into new 15 mL centrifuge tubes. For each step, sediment samples and reagents were shaken on an orbital shaker for the required amount of time then centrifuged. Following this, reacted samples were then decanted into appropriately sized, acid cleaned polyethylene bottles, pooled, and stored for later dilution and analysis. As with total P, random duplicates and blanks were prepared and analyzed following this method for quality assurance purposes. Samples from Step II, III, and IV used the same method as total P for analysis. Step I samples required additional processing following extraction prior to UV analysis to break down organic interferences with color development (MacDonald, 2013). This extra step involved a further reaction with 12M hydrochloric acid and 50% w/v MgNO₃. The solutions were dried and crystallized on a hotplate at 80°C, then ashed in a muffle furnace at 550°C for two hours. Finally, they were reacted again with 1M hydrochloric acid and shaken on an orbital shaker for 16 hours, after which they were ready to be diluted and analyzed via the molybdate blue method on the UV-Visible spectrophotometer.

Sequential phosphorus extractions were completed for a subset of samples from Sites U1474 and U1479 that represent the last 500 kya, due to a notable drop in sample resolution after this point in samples from both sites. The sample sets were further cut in half, so that every other sample in sequence was analyzed using this method. U1474's subset consists of 89 samples, and U1479's subset contains 143 samples.

Table 1. Sequential P extraction steps ((adapted from Latimer et al. (2006b); after Mortlock & Froelich (1989); Ruttenberg (1992); Anderson & Delaney (2000)).

Step	Reagents	P Component Isolated
Oxide-Associated (I)	10 mL CDB solution (6 h) (0.22M Na citrate, 1 M NaHCO ₃ , 0.13 M Na-dithionite), 10 mL of 1 M MgCl ₂ (2 h), 10 mL H ₂ O (2 h)	Adsorbed and reducible or reactive Fe-bound P
Authigenic (II)	10 mL of 1 M Na-acetate buffered to pH 4 w/acetic acid, 10 mL of 1 M MgCl ₂ (2 h)-twice, 10 mL H ₂ O (2 h)	Carbonate fluorapatite (CFA), biogenic hydroxy apatite, and CaCO ₃ -bound P
Detrital (III)	10 mL of 1 M HCl (16 h)	Detrital P
Organic (IV)	1 mL 50% (w/v) Mg(NO ₃) ₂ , dry in low oven, ash at 550° C (2 h), add 10 mL of 1 M HCl (16 h)	Organic P

Data Analysis

Stacked plots of downcore elemental concentrations versus their calculated ages were made in OriginPro 2024. Important elemental ratios were also calculated and plotted in the same manner. In all stacked plots, the approximate timings of marine isotope stages were overlain on the data, using the ages denoted in Lisiecki & Raymo (2005), calculated from a composite of 57 globally-distributed benthic δ¹⁸O records. Box plots to compare the spread of individual elemental concentrations between cores were created, and Pearson correlation coefficients were calculated using the built-in descriptive statistics functions in OriginLab.

For more advanced statistical analysis, principal components analyses (PCAs) for each site were completed using Origin, to elucidate the dominant elemental patterns in U1474 and U1479. To better refine the observed patterns in the PCA, Generalized Additive Models (GAMs) were created using the scores of the first principal components of the records. GAM analysis was also performed in Origin, using the pyGAM package developed by Servén et al. (2018) and OriginPro's built-in Python interface. The advantage of applying a GAM to the PCA is that it

accounts for the uneven timesteps of an age model, allowing for much smoother, more precise time series analysis (Simpson, 2018). Applying a GAM here also allows us to identify significant changes more easily in the data temporally. Using the first derivatives of the fitted GAMs, values that deviate from 0 are considered significant changes in our elemental concentration data (Simpson, 2018).

For our spectral time series analysis, only the proxy data from U1474 was explored further. This is because U1474's age model is not orbitally tuned, allowing for an unbiased assessment of any orbital cycle periodicities that naturally exist within the data. U1479's refined age model is orbitally tuned to precession, and therefore was omitted from this section of the data analysis. To investigate any periodicity present within our proxy data, the REDFIT tool in the software package PAST (PAleontological STatistics) was used, following linear interpolation of the data to create even timesteps of 3.71 kya (Hammer et al., 2001).

Data Accuracy

Across all steps of analysis, laboratory standards and replicates were used to assess the accuracy of our results. Laboratory standard NIST 1646a (estuarine sediment) was analyzed 65 times over the course of our XRF analysis. Our K and Ti data were excellent, averaging a relative error of 4% and 3%, respectively. Our Ca values were less accurate and were always higher than the accepted value for 1646a, averaging a relative error of 14.1%. Because our sediments for Site U1474 and U1479 were very high in Ca, we believe that any residue left on the XRF would have caused enough contamination to skew the relatively lower concentrations of Ca in the standard to a higher concentration. Our worst average relative error was Fe, with a value of 43.7%. Despite this large discrepancy, the standard deviation for Fe was 155.2, indicating that its data spread was consistent and therefore usable for our purposes.

Using the sample laboratory standard from our XRF analysis, our SRM measurements were excellent, with a standard deviation from accepted values of 8.8 and an average relative error of 3%. Replicates from our P_{TOT} and P_{EXT} steps yielded moderately good results, with average relative errors of 7.8% and 11.9%, respectively. Potential sources of error during these steps were incomplete digestion of sediments or over-digestion of sediments during sequential analysis, which would have skewed our results. Using three times the standard deviation of our blank samples, the detection limit for P on the UV-Visible spectrophotometer was 1.7 ppm.

CHAPTER 4

RESULTS – U1474**XRF analysis results**

In U1474, Ca concentration values are the highest, ranging from 10-27 wt%, while Zr has the lowest concentration values, ranging from 83 to 172 ppm (Table 2; Fig. 4). All our data plots display a millennial-scale increasing and decreasing pattern throughout the 1.1 mya record (Fig. 5). Our Ca record first decreases to a minimum from 1110 to 950 kya, then increases to a maximum from 950 to 500 kya. It then decreases again to a similar minimum concentration from 500 to 150 kya, and finally increases through the end of our record (Fig. 5). The Ca and Ti concentration plots have a strong inverse relationship, and the Ti concentration record mirrors Ca closely (Fig. 5).

Ti, K, and Zr are all commonly used indicators of terrigenous input, and for the record at U1474 they follow similar trends from 1110 to 0.5 kya (Fig. 5); they follow a long-term pattern that gradually decreases in concentration from 1110 to 500 kya where they reach a minimum. They then increase in concentration from 500 to around 150 kya, where a maximum is reached across each elemental concentration record; finally they all decrease in concentration through 0.5 kya (Fig. 5). Ti and K have the most similar trends and have more pronounced maxima and minima values, while Zr has less pronounced variability in its trend. The Fe record also follows this long-term terrigenous indicator pattern for U1474 (Fig. 5). Ca displays an inverse trend to the other XRF-derived elements, varying opposite the terrigenous indicator elements (Fig. 5).

The inverse relationships we observe in biomass (Ca) and terrigenous indicators are likely caused by a dilution effect. A decrease in the input of terrigenous material to U1474

causes the relative biogenic CaCO₃ content of the sediment to increase. Likewise, an increase in terrigenous material to the core sites would cause the relative Ca concentration to decrease. A change in biomass would have no effect on the input of sediment, and so terrigenous input changes are the most likely driving mechanism behind this observed trend.

Table 2. Descriptive statistics of select XRF data, U1474. Values were computed using OriginPro's built-in "Descriptive Statistics on Columns" function.

Element	Mean	Median	Minimum	Maximum
Ca (wt. %)	17.7	17.5	10.1	26.7
Ti (wt. %)	0.23	0.23	0.11	0.39
Zr (ppm)	154.5	153.6	83.3	351.3
Fe (wt. %)	2.4	2.4	1.2	4.2
K (wt. %)	1.3	1.3	0.9	1.7

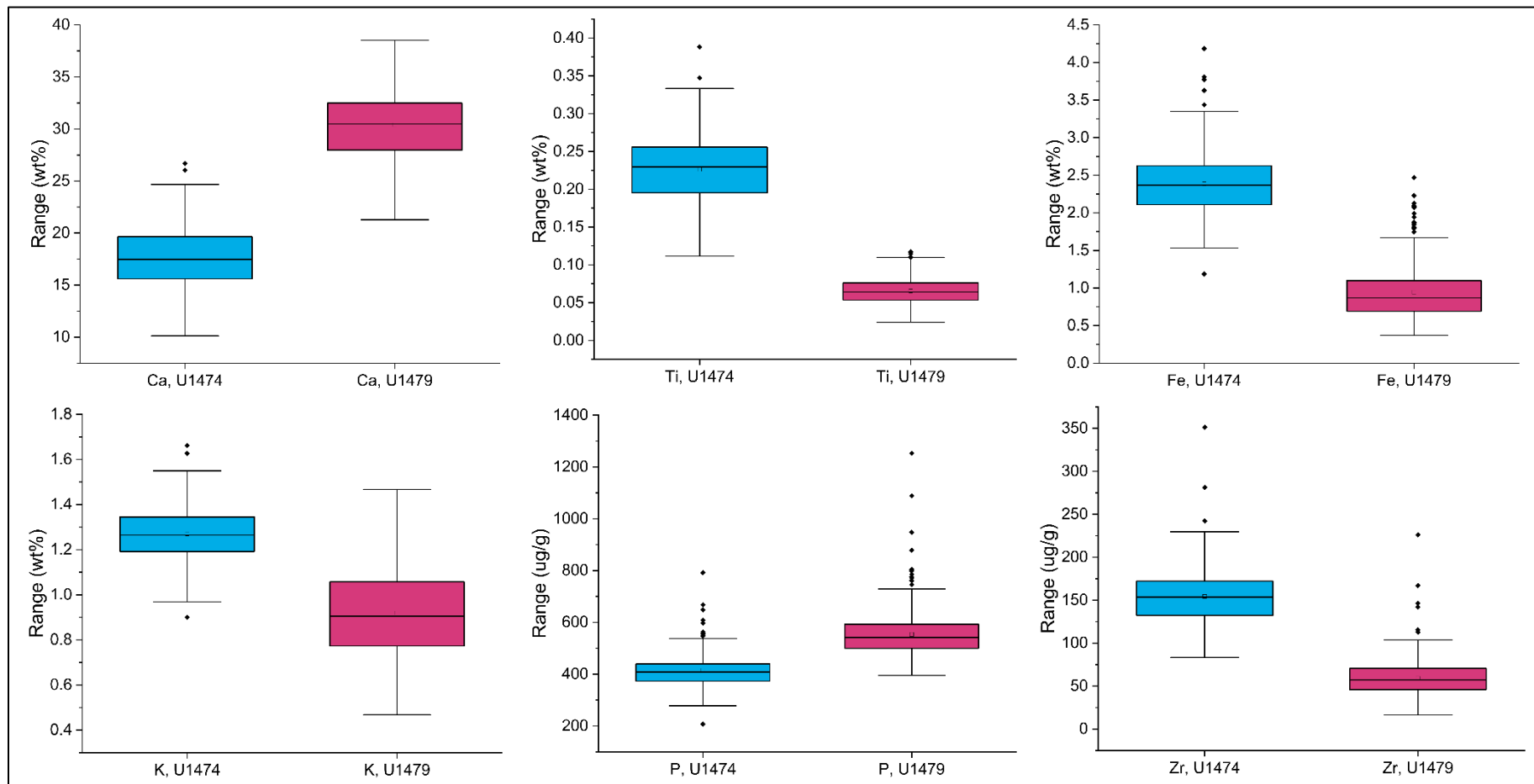


Figure 4. XRF and P_{TOT} box and whisker plots, U1474 and U1479. Ca, Ti, Fe, and K plots have units of wt%, and P_{TOT} and Zr have units in ug/g. Individual points above and below whiskers are outlier values of each dataset. Produced using OriginPro graphing software.

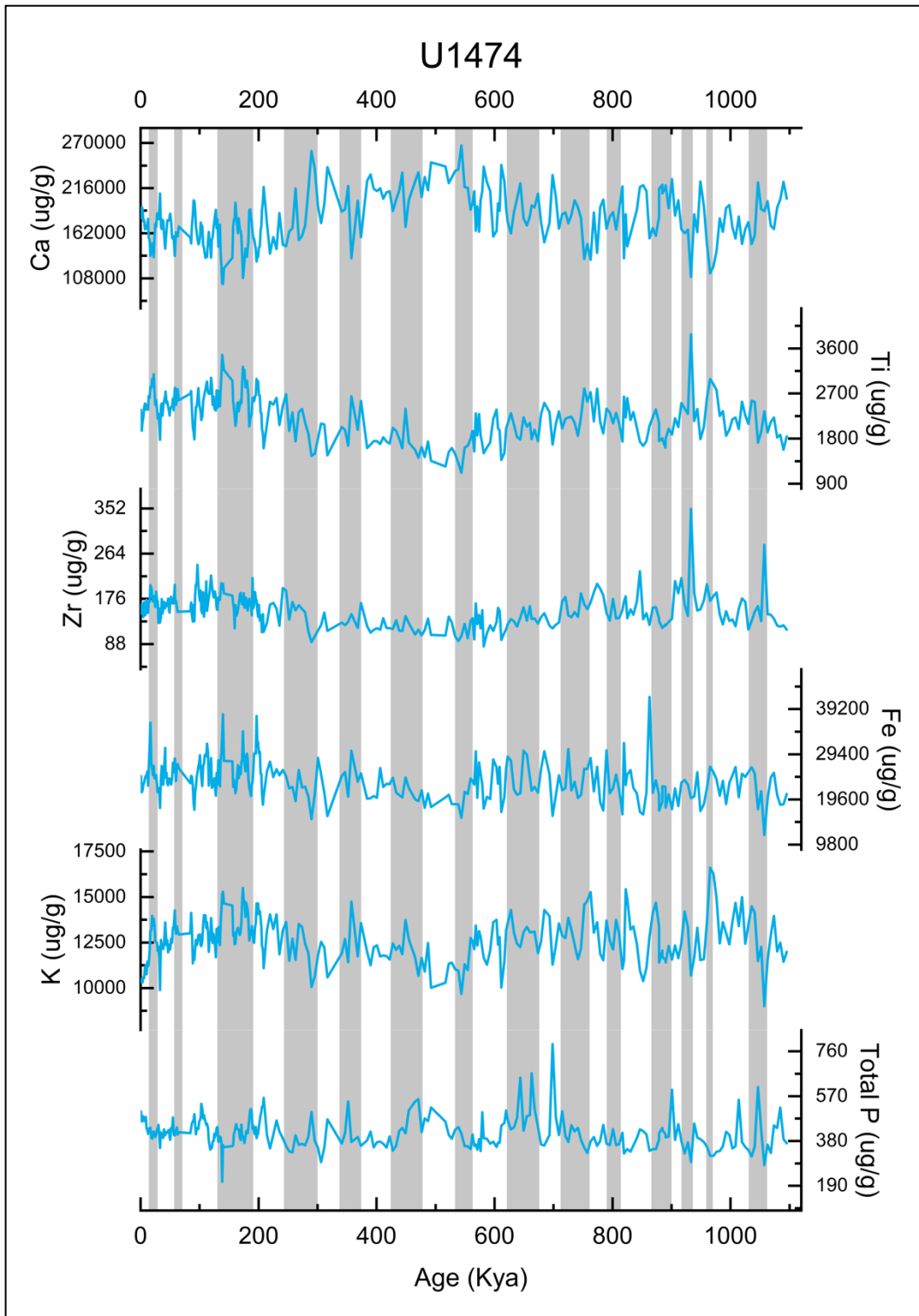


Figure 5. XRF concentrations and total P(P_{TOT}), 1.1 mya, U1474. Gray bars denote approximate timings of glacial cycles, from Lisiecki & Raymo (2005).

Total P and Sequential P analysis results

Total P (P_{TOT}) values range from 207 to 791 ppm across our 1.1 mya record (Table 3).

P_{TOT} 's downcore record (Fig. 5) generally follows a variable trend but not a millennial-scale fluctuation, differing from the XRF elemental data that displays a clear increasing and decreasing pattern (Fig. 5). It displays several small maxima and one minimum throughout the 1.1 mya timespan, with the most prominent ones occurring at 1050, 900, 690, and 140 kya (Fig. 5).

The total extractable P concentration (P_{EXT}) ranges from 145 to 302 ppm (Table 3). Oxide-associated P oscillates throughout the record, with a pronounced minimum at 60 and 190 kya and a maximum at 490 kya (Fig. 6). Authigenic P decreases in concentration through 410 kya, increases to a maximum at 210 kya followed by a sharp decrease to a minimum at 175 kya, and then gradually increases through 0.5 kya (Fig. 6). Organic P increases throughout the 492 kya timespan, with one major minimum at 180 kya and several minor maxima. Detrital P trends upwards throughout the record, but at 190 kya it sharply increases in concentration and reaches a sustained maximum until 100 kya, when it decreases again to lower concentrations through the end of the record (Fig. 6).

P_{EXT} averaged 53.7% of our mean P_{TOT} concentrations, but when this fraction and those of the individual components are plotted downcore, they display variable patterns (Table 3, Fig. 7). From 200 to 100 kya, higher fractions of extractable P relative to P_{TOT} are recorded in oxide-associated P, detrital P, and organic P, with maximum percentages visible at 140 kya (Fig. 7). A minor increase in extractable P concentrations relative to P_{TOT} is also recorded at 305 kya. Authigenic P also displays a variable extraction pattern, but from 200 to 100 kya it records a decrease in concentration relative to P_{TOT} (Fig. 7).

Table 3. Descriptive statistics of P data, U1474.

Element	Mean (ppm)	Median (ppm)	Minimum (ppm)	Maximum (ppm)	Average fraction of P_{EXT} (%)	Average fraction of P_{TOT} (%)
Total P (P_{TOT})	415	408	207	791	--	--
Oxide- associated P (Step I)	50	52	4	7	23.0	12.1
Authigenic P (Step II)	53	52	20	92	24.7	12.6
Detrital P (Step III)	61	55	20	143	26.3	14.8
Organic P (Step IV)	59	57	7	109	26.1	14.2
Reactive P (I, II, IV)	163	163	94	208	73.8	38.9
Total Extractable P (P_{EXT})	224	221	145	302	--	53.7

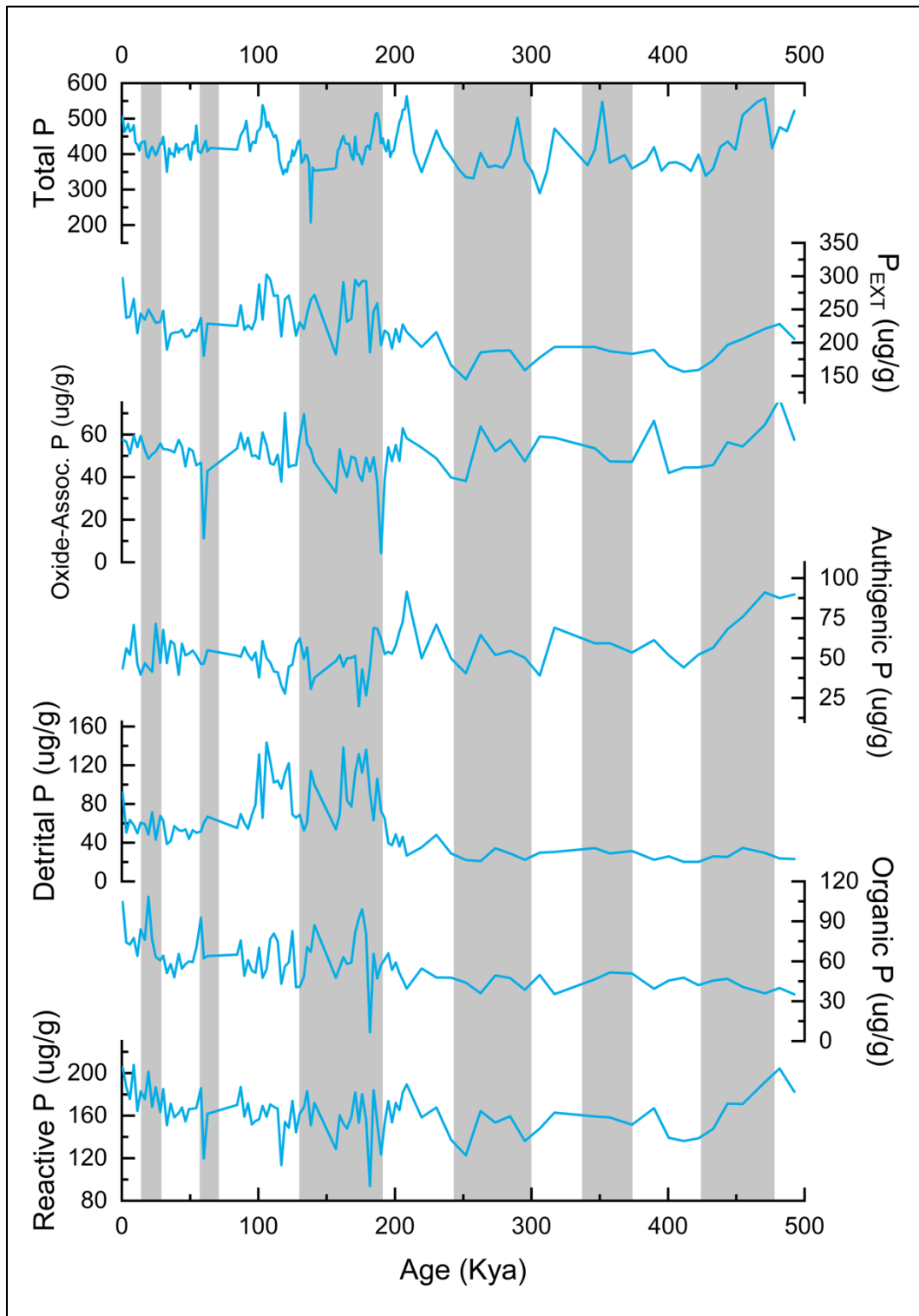


Figure 6. Detailed P geochemistry, U1474. Gray bars denote approximate timings of glacial cycles, from Lisiecki & Raymo (2005).

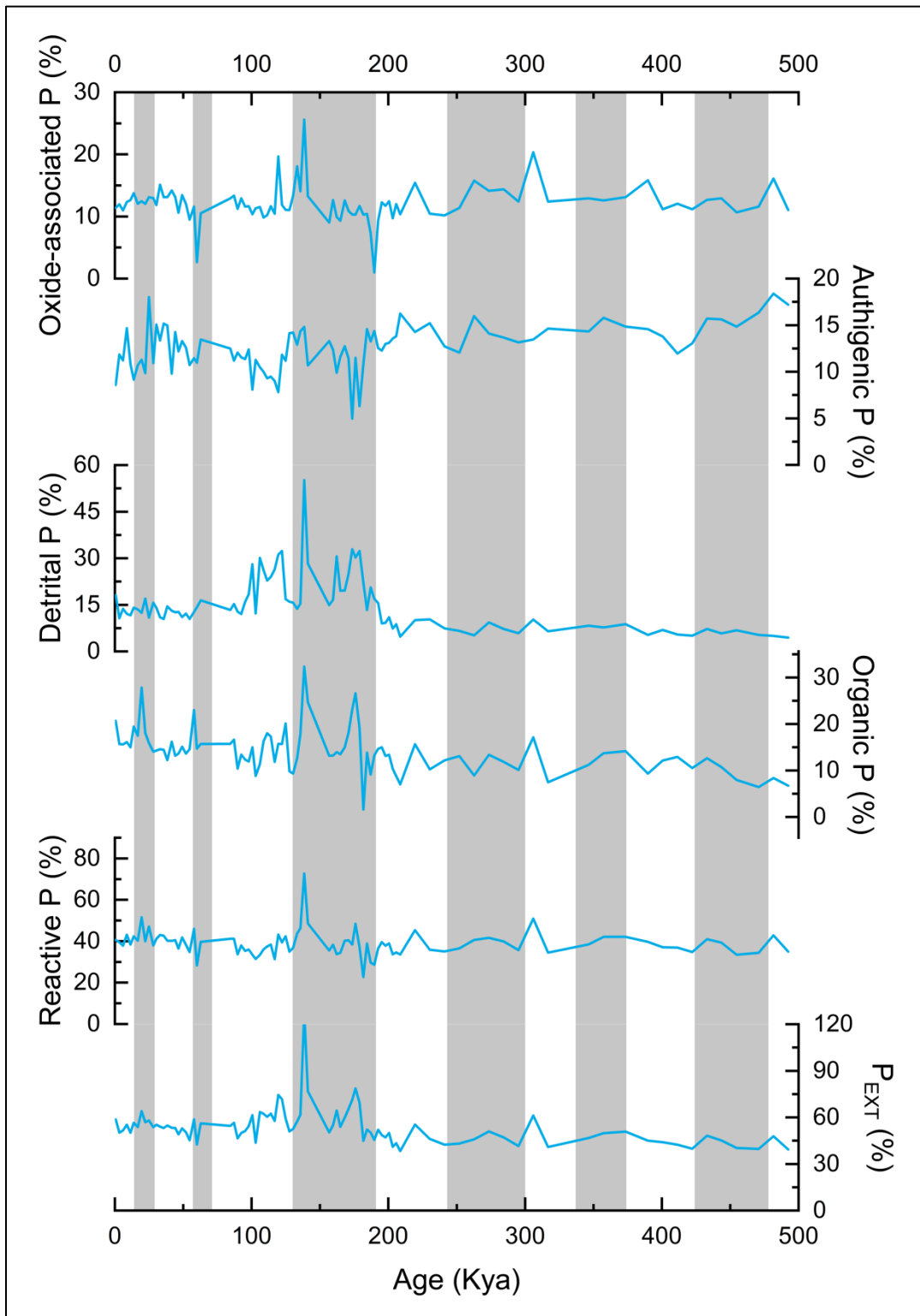


Figure 7. Changes in the percentage of P_{TOT} extracted by each step of the sequential extraction, U1474. Gray bars denote approximate timings of glacial cycles, from Lisiecki & Raymo (2005).

Elemental ratio data

Elemental ratios were calculated to evaluate changes in export production, productivity, and sediment provenance. Ca/Ti displays a similar millennial-scale trend to the elemental data plots. It begins low, gradually increases to a maximum centered at 525 kya, and then gradually decreases to lower values at the end of the record (Fig. 8). Ca/Ti is used to emphasize the variation in terrigenous sediment delivery to each core site. Maxima in this ratio are interpreted to represent decreases in the terrigenous sediment supply, while minima are interpreted to represent increases in the supply.

Fe/Ti shows a similar long-term pattern to Ca/Ti, but it is more muted; it increases from 1100 to 500 kya and then decreases from 500 to 0.5 kya (Fig. 8). It records one significant maximum at 860 kya and two minima at 1060 and 930 kya. Zr/Ti differs from Ca/Ti and Fe/Ti and does not show a long-term increasing and decreasing pattern. Its values are also much more variable than Fe/Ti but contains two similar maxima at 1060 and 850 kya (Fig. 8). Fe/Ti and Zr/Ti can both be used to assess changes in terrigenous provenance, where significant variations in the trend indicate a change in sediment source.

P_{TOT}/Ti and P_{TOT}/Zr , which are both used here to examine changes in export production, display nearly identical strongly variable trends throughout the last 1.1 mya (Fig. 9). Both increase to a broad maximum around 500 kya, then decrease through 0.5 kya. The ratio of detrital P to Zr, another terrigenous material indicator, starts low, increases sharply, and maintains a sustained peak from 175 to 90 kya, then decreases again through the end of our record (Fig. 10).

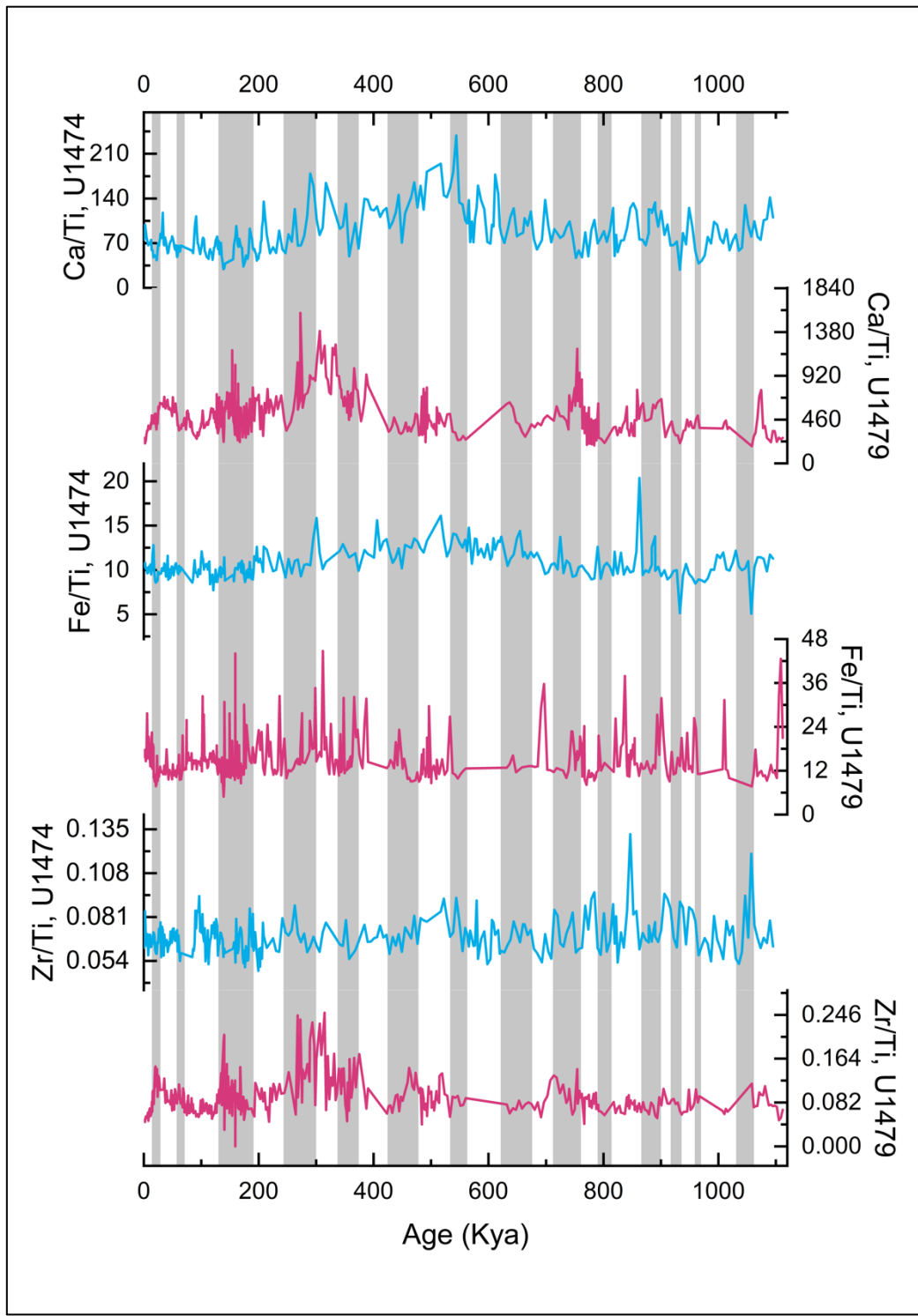


Figure 8. Ca/Ti, Fe/Ti, and Zr/Ti comparisons, U1474 and U1479. Plots are color-coded by site, with cyan plots for U1474 and magenta plots for U1479. Gray bars denote approximate timings of glacial cycles, from Lisiecki & Raymo (2005).

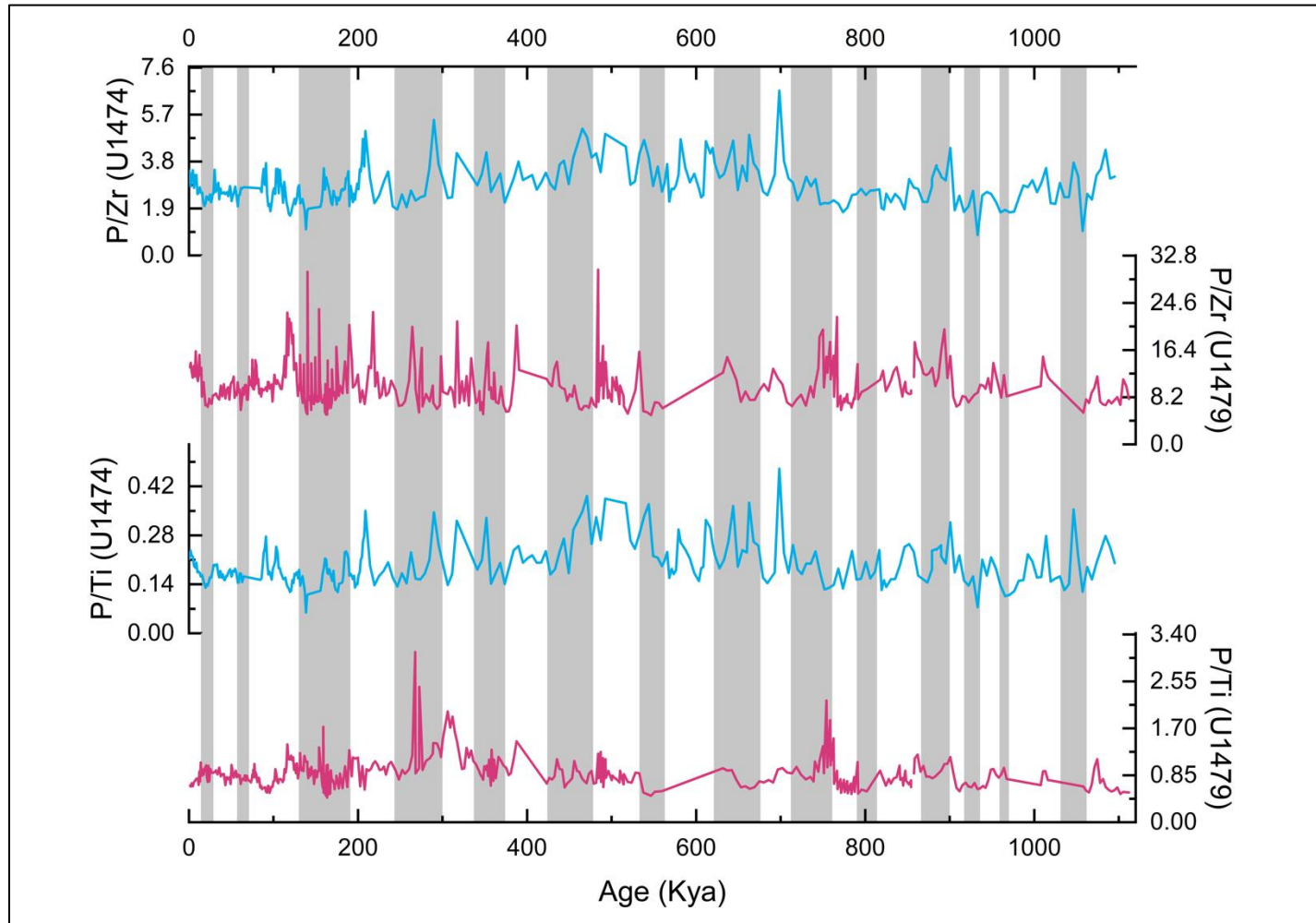


Figure 9. $\text{P}_{\text{TOT}}/\text{Zr}$ and $\text{P}_{\text{TOT}}/\text{Ti}$, U1474 and U1479. Plots are color-coded by site, with cyan plots for U1474 and magenta plots for U1479. Gray bars denote approximate timings of glacial cycles, from Lisiecki & Raymo (2005).

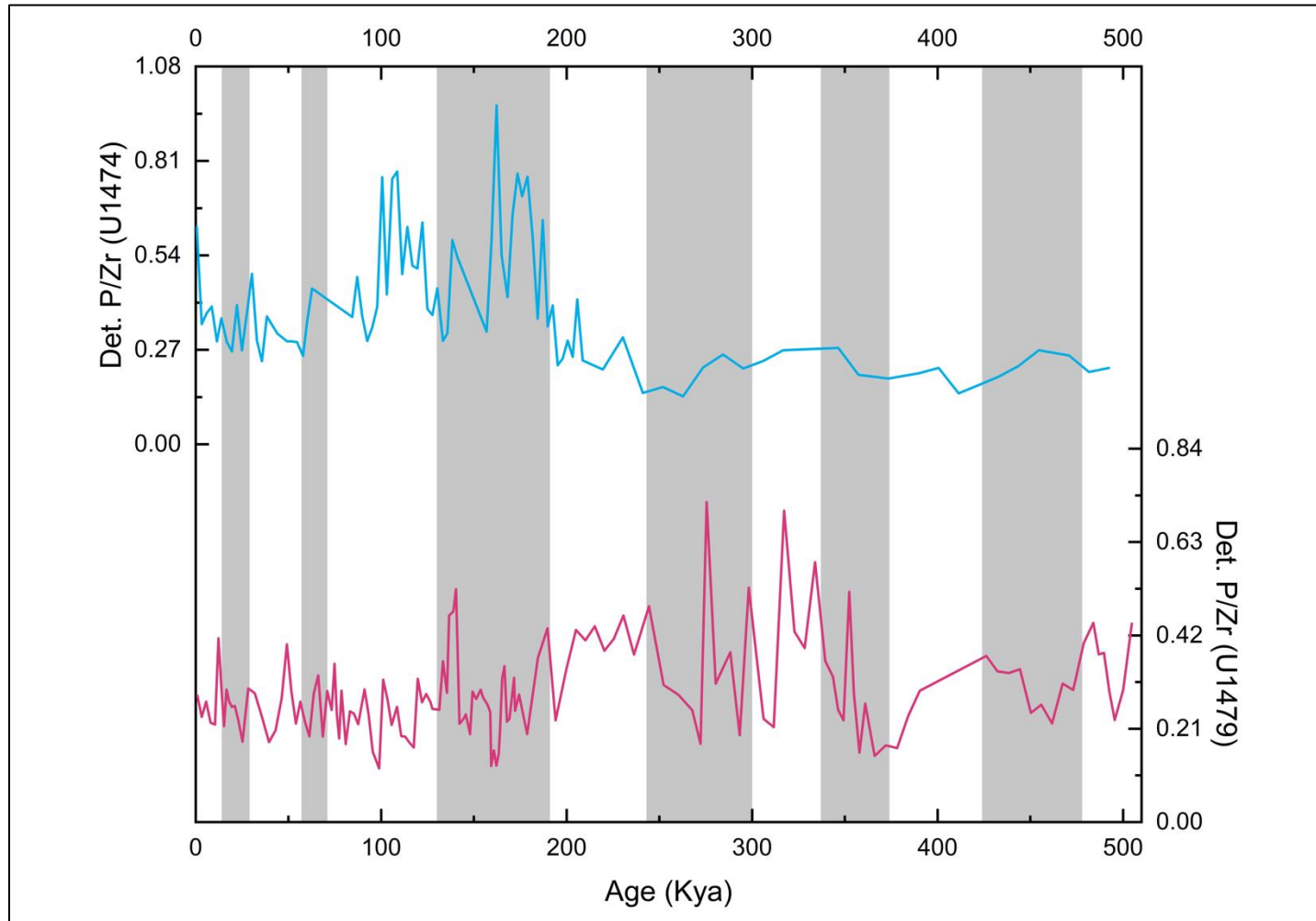


Figure 10. Det. P/Zr, U1474 and U1479. Plots are color-coded by site, with cyan plots for U1474 and magenta plots for U1479. Gray bars denote approximate timings of glacial cycles, from Lisiecki & Raymo (2005).

Correlation coefficients

U1474 has strong correlations between some elements (Table 4), and the correlation varies between different time intervals. From 1100 to 420 kya, U1474 displays many moderate ($r=\pm 0.4$ to ± 0.59) to high ($r=\pm 0.6$ to ± 0.79) correlations (Table 4). The strongest correlation is between Ca and Ti, with a correlation coefficient of $r=-0.94$. Other significant correlations are between Ca and Fe ($r=-0.68$), Ca and K ($r=-0.78$), Zr and Ti ($r=0.66$), Ti and K ($r=0.67$) and Fe and K ($r=0.66$). Total P displays only moderate correlation with Ca ($r=0.51$) and moderate inverse correlation with Ti ($r=-0.48$).

From 492 to 0.5 kya, several significant changes can be seen between correlation coefficients (Table 4 and 5). Ca and Ti remain the strongest elemental relationship, with a correlation coefficient of $r=-0.94$. Many elements continue to display sustained strong correlations or relationships that increase in correlation; these include Ca and Fe ($r=-0.82$), Ca and K ($r=-0.81$), Ti and Zr ($r=0.69$), Ti and K ($r=0.77$), and Fe and K ($r=0.70$). Two elemental relationships strengthen from moderate to strong correlations, Ca and Zr ($r=-0.64$) and Ti and Fe ($r=0.75$). Conversely, PTOT's relationships with the other elements weaken markedly after 420 kya (Table 5). The most significant decrease in correlation is seen between PTOT and Ca, which decreases by 0.27 from $r=0.51$ to $r=0.24$.

Table 4. Pearson correlation coefficients of XRF elements and PTOT, U1474. Coefficients are color-coded to denote the strengths of each relationship. **Bold, red** = very high correlation ($\geq \pm 0.8$), **non-bold, red** = high correlation (± 0.6 to ± 0.79), black, non-bold = moderate correlation (± 0.4 to ± 0.59), non-bold, gray = low to negligible correlation ($\leq \pm 0.39$).

Full record (1100 – 0.5 kya)						
	Ca	Ti	Zr	Fe	K	PTOT
Ca	1	-0.95	-0.61	-0.78	-0.76	0.33
Ti	--	1	0.69	0.68	0.68	-0.30
Zr	--	--	1	0.25	0.26	-0.21
Fe	--	--	--	1	0.67	-0.24
K	--	--	--	--	1	-0.27
PTOT	--	--	--	--	--	1
1100 – 420 kya						
	Ca	Ti	Zr	Fe	K	PTOT
Ca	1	-0.94	-0.51	-0.68	-0.78	0.51
Ti	--	1	0.66	0.51	0.67	-0.48
Zr	--	--	1	0	0.1	-0.27
Fe	--	--	--	1	0.66	-0.33
K	--	--	--	--	1	-0.30
PTOT	--	--	--	--	--	1
420 – 0.5 kya						
	Ca	Ti	Zr	Fe	K	PTOT
Ca	1	-0.94	-0.64	-0.82	-0.81	0.24
Ti	--	1	0.69	0.75	0.77	-0.25
Zr	--	--	1	0.40	0.43	-0.19
Fe	--	--	--	1	0.70	-0.21
K	--	--	--	--	1	-0.30
PTOT	--	--	--	--	--	1

Table 5. Change in Pearson correlation coefficients of XRF elements and TP_{TOT}, U1474. Changes are calculated as the difference between the older part of the record (1110 to 420 kya) and the younger part of the record (420 to 0 kya). Changes are color-coded according to degree of change and by increases or decreases in value. **Bold, bright blue** = strong negative change (≥ -0.26), **non-bold, bright blue** = moderate negative change (-0.16 to -0.25), **non-bold, light blue** = weak negative change (-0.06 to -0.15), **non-bold, gray** = negligible change (± 0.05), **non-bold, orange** = weak positive change (+0.06 to +0.15), **non-bold, bright red** = moderate positive change (+0.16 to +0.25), **bold, bright red** = strong positive change ($\geq +0.26$).

	Ca	Ti	Zr	Fe	K	TP _{TOT}
Ca	--		+0.13	+0.14	+0.03	-0.27
Ti	--	--	+0.03	+0.24	+0.10	-0.23
Zr	--	--	--	+0.40	+0.33	-0.08
Fe	--	--	--	--	+0.04	-0.12
K	--	--	--	--	--	0
TP _{TOT}	--	--	--	--	--	--

PCA and GAM results

PCA was completed for U1474 over the entire record (0.5 to 1100 kya) and examined the relationships between Fe, Ti, Ca, K, Zr, and P_{TOT}. The first principal component (PC1) represents 62.23% of the variance in our record, while PC2 and PC3 represent 14.91% and 14.33% respectively (Fig. 10a). Because only PC1 had a significant eigenvector value (3.73), it will be the focus for the remainder of this project.

Of the variables included in the PCA, Ti and Ca display the strongest significance to our record with respective eigenvectors of 0.49 and -0.51 (Fig. 10b). Fe and K also display

significance to PC1, with equivalent eigenvector values of 0.42. Total P and Zr show weak relationships with PC1, with eigenvector values of -0.22 and 0.33. U1474's PC1 score plot shows both increasing and decreasing trends from 1100 kya to 0.5 kya (Fig. 11). It first predominantly increases from 1100 to 875 kya, decreases from 875 to roughly 500 kya, increases again from 500 to 150 kya, and finally decreases from 150 to 0.5 kya. This pattern is enhanced and emphasized in the GAM analysis (Fig. 12).

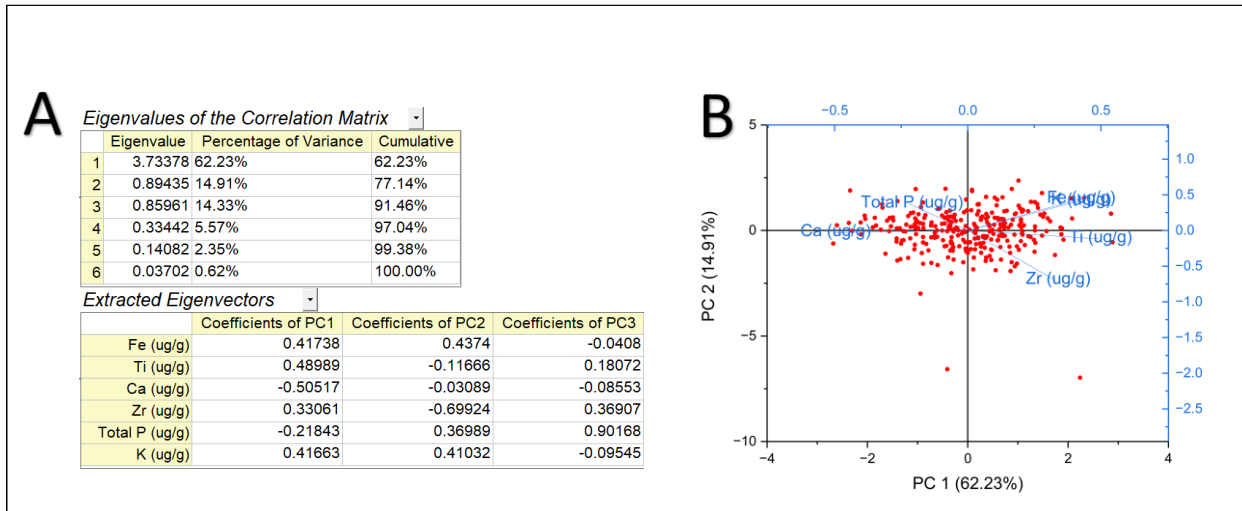


Figure 11. U1474 PCA data report and biplot. Figure 11a displays the calculated eigenvalues of each principal component and their respective share of the total variance, as well as the eigenvector values for each variable used in the PCA. Figure 11b displays the biplot of PC1 and PC2 for U1474. Red dots denote the spread of each individual datapoint in U1474's dataset.

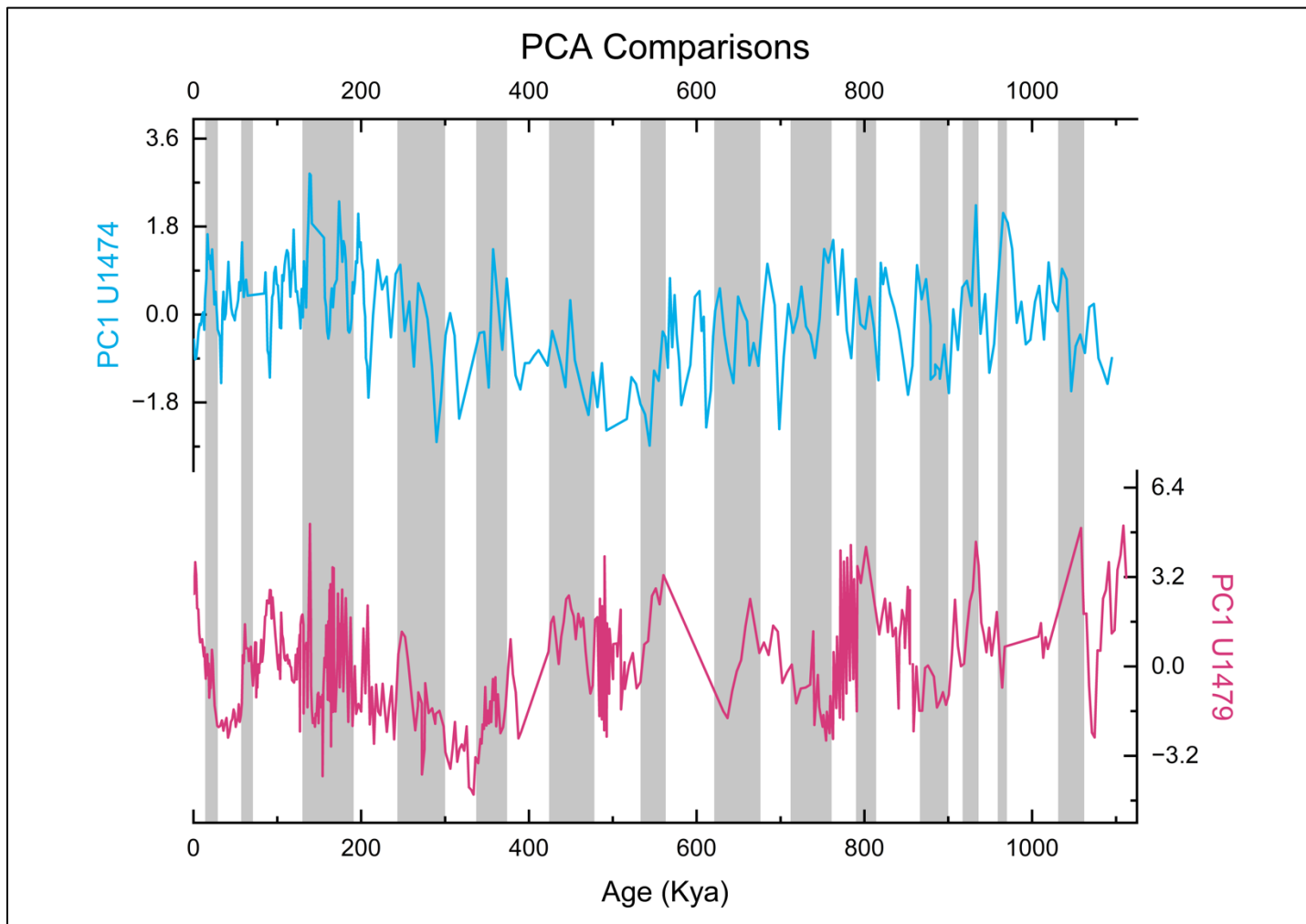


Figure 12. PC1 score plots for U1474 (top) and U1479 (bottom). Deviations from 0 denote significant changes in our record and are explored further in the discussion. Gray bars denote approximate timings of glacial cycles, from Lisiecki & Raymo (2005).

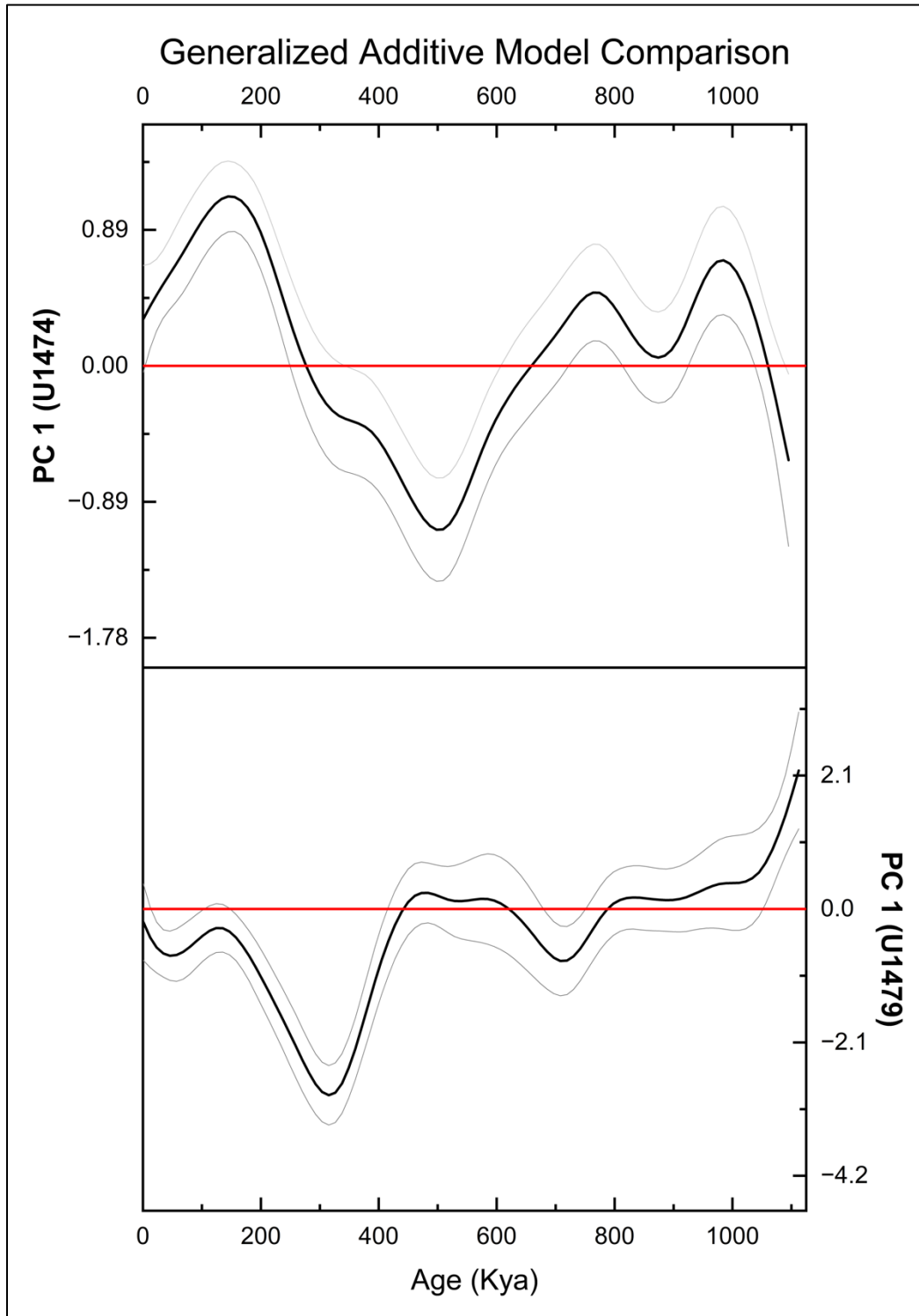


Figure 13. Generalized additive models (GAMs) of the first principal components of U1474 and U1479. Large deviations from 0 (horizontal red line) denote significant changes in our geochemical record

Spectral analysis

Timeseries spectral analysis was completed for U1474's PC1 for the entire length of U1474's record because it represents an amalgamation of all our significant variables for this site (Fig. 14). Peaks above the 95% X^2 confidence line were detected for 3 distinct frequencies, which were then multiplied by our timestep of 3.71 kya and were found to correspond with 126 kya, 107 kya, and 94.6 kya periodicities. The most significant of these periodicities is the 107 kya cycle, which corresponds with the cycle of orbital eccentricity.

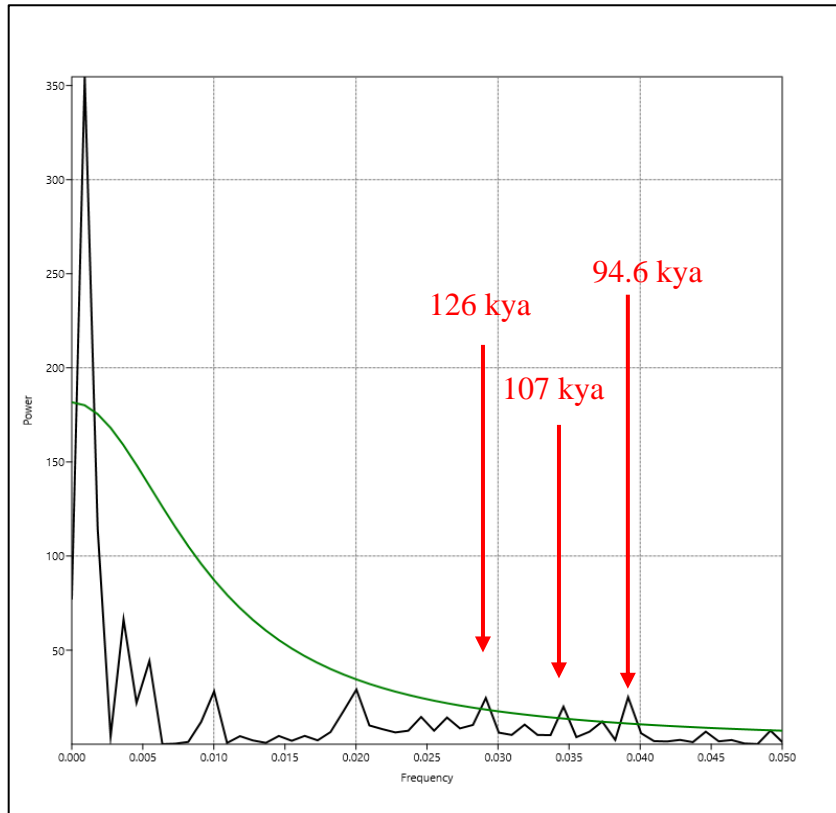


Figure 14. REDFIT plot for PC1 of U1474. The green curve is indicative of the 95% X^2 significance level for the dataset. Significant frequencies and their corresponding periodicities are denoted by the red arrows.

RESULTS – U1479

XRF analysis results

Like U1474, U1479's sediment chemical composition is dominated by Ca, which ranges in value from 21.3 to 38.5 wt% and its lowest concentration values are for Zr, which ranges from 17 to 226 ppm (Table 6, Fig. 4). Ca is highly variable from 1112 to around 550 kya, with many maxima and minima recorded during this period. From 550 to 300 kya, Ca records an increase in concentrations to its largest maximum of 38.1 wt% (Fig. 15). From 300 kya to 0.8 kya, it follows a decreasing trend, though we do record a brief increase in Ca around 43 kya (Fig. 15). As in U1474, Ti and K both display strong inverse relationships with Ca and mirror its trend closely throughout the record. Zr displays a variable trend throughout the entire record, with distinct maxima recorded at 1060, 770, 460, and 140 kya, the last of which is the most prominent with a concentration of 226 ppm (Fig. 15; Table 6). Zr differs from Ti especially from 400 to 300 kya (Fig. 15). Fe follows a constant, variable trend throughout U1479's record, with no minima but several maxima at 1100, 835, 700, 105, and 6 kya (Fig. 15).

As in U1474, Ti, K, and Zr are all used as terrigenous indicators and Ca as a biomass indicator. The previously discussed dilution effect of terrigenous input on our Ca record is also viewed in U1479's data, where increases or decreases in our detrital elements are mirrored by decreases or increases in biomass (Fig. 15). Unlike in U1474 though, U1479's Zr record appears to decouple from Ti and K, varying independently after 400 kya (Fig. 15). Additionally, from 450 kya to 0.8 kya, Zr begins to follow glacial-interglacial cycles, generally increasing during glacial cycles and decreasing during interglacial cycles (Fig. 15). The decoupling of Zr and Ti but not of Ti and K is an interesting phenomenon that will be explored later in the discussion.

Table 6. Descriptive statistics of select XRF data, U1479. Values were computed using OriginPro's built-in "Descriptive Statistics on Columns" function.

Element	Mean	Median	Minimum	Maximum
Ca (wt. %)	30.1	30.1	21.3	38.5
Ti (ppm)	665	652	241	121
Zr (ppm)	59	57	17	226
Fe (wt. %)	1.0	0.9	0.4	3.9
K (wt. %)	0.9	0.9	0.5	1.5

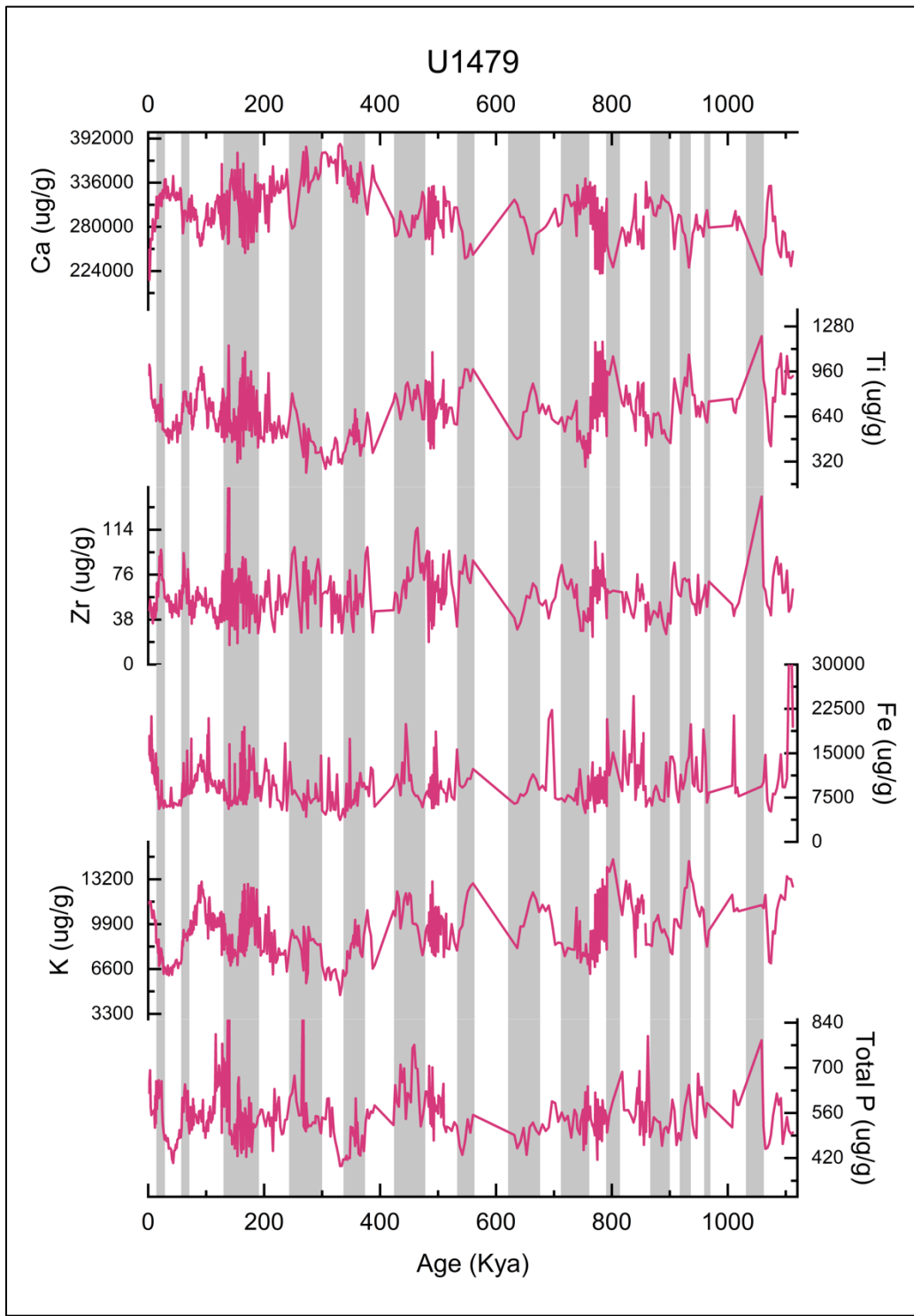


Figure 15. XRF concentrations and P_{TOT}, U1479. Gray bars denote approximate timings of glacial cycles, from Lisiecki & Raymo (2005).

Total P and Sequential P analysis results

P_{TOT} values range from 395 to 1253 ppm across our record (Table 6). P_{TOT} follows a similar trend to Zr, Ti, and K, with some large variations but a constant trend throughout the record (Fig. 15). P_{TOT} displays many significant maxima in its record, the most prominent of which are recorded at 1060, 860, 455, 265, and 140 kya (Fig. 15). Like U1474, U1479's P_{EXT} concentration values are significantly lower than P_{TOT} , ranging from 159 to 428 ppm (Table 7). P_{EXT} 's downcore pattern is similar to P_{TOT} , exhibiting a variable trend and a similar maximum to P_{TOT} at 140 kya (Fig. 16).

Oxide-associated P displays a long-term, gradual curve from 504 to 0.8 kya (Fig. 16). It increases to a maximum value of 93 ppm at 245 kya, decreases to a minimum value of 30 ppm at 140 kya, and then varies through 0.8 kya (Fig. 16). Both authigenic and detrital P share similar trends throughout the record and vary between maxima during glacial periods and minima during interglacial periods, especially after 300 kya (Fig. 16). Organic P's concentrations begin low and then sharply increase after 150 kya through the end of our record. As seen in our P_{TOT} and P_{EXT} records, reactive P, detrital P, and authigenic P display a very distinct concentration maximum at approximately 140 kya (Fig. 16).

P_{EXT} averaged 38.5% of P_{TOT} 's mean values, but like U1474, it displays a variable extraction pattern downcore (Fig. 17). The components of P_{EXT} also display variable downcore extraction patterns. Oxide-associated P's fraction relative to P_{TOT} ranged from 2.4 to 20%, with an average of 10.3% (Fig. 17, Table 7). Authigenic P consistently displayed the highest extraction fraction of P_{TOT} , ranging from 8 to 22.7% with an average of 16.4% (Fig. 17). Conversely, detrital P nearly always had the lowest fraction over our record, with an average of 2.8% (Table 7); its only deviation from this pattern was seen at 140 kya, where its relative

fraction peaked at 8.9% (Fig. 17). Organic P maintained a consistently low fraction of P_{TOT} , except at the end of our record, where it reaches a maximum fraction of 30% at 3 kya (Fig. 17).

Table 7. Descriptive statistics of P data, U1479. Mean, median, minimum and maximum values were computed using OriginPro's built-in "Descriptive Statistics on Columns" function, and the average fractions were computed with Microsoft Excel.

Element	Mean (ppm)	Median (ppm)	Minimum (ppm)	Maximum (ppm)	Average fraction of P_{EXT} (%)	Average fraction of P_{TOT} (%)
Total P (P_{TOT})	554	541	395	1253	--	--
Oxide-associated P (Step I)	57	56	30	94	27.2	10.5
Authigenic P (Step II)	92	87	61	263	43.2	16.4
Detrital P (Step III)	17	15	6	107	7.7	2.9
Organic P (Step IV)	48	40	18	207	22.0	8.7
Reactive P (I, II, IV)	197	192	145	354	92.4	35.6
Total Extracted P (TP_{EXT})	214	205	159	428	--	38.5

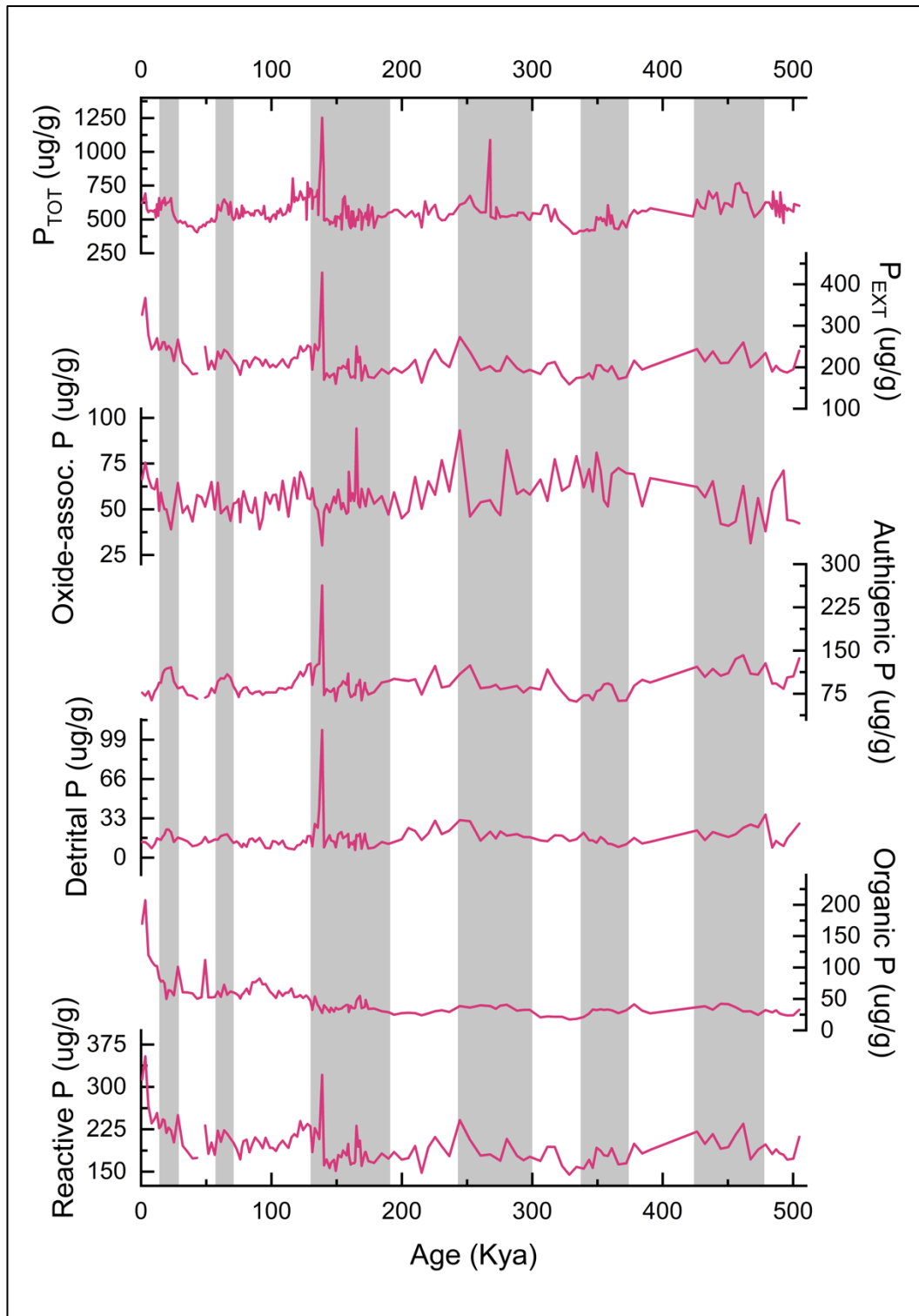


Figure 16. Detailed P geochemistry, U1479. Breaks in the authigenic P and reactive P records at approximately 47 kya are due to a lost sample. Gray bars denote approximate timings of glacial cycles, from Lisiecki & Raymo (2005).

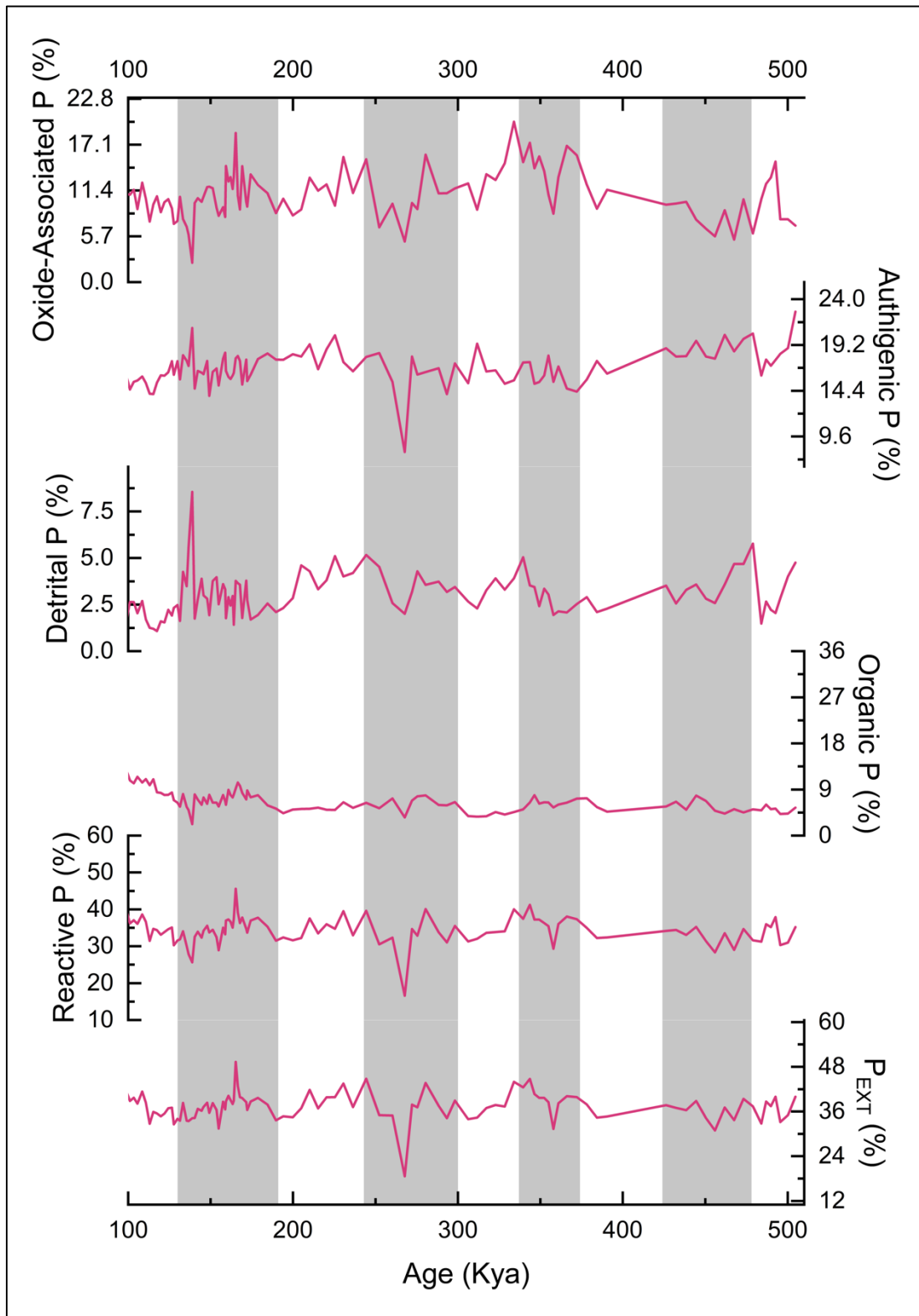


Figure 17. Changes in the percentage of P_{tot} extracted by each step of the sequential extraction, U1479. Gray bars denote approximate timings of glacial cycles, from Lisiecki & Raymo (2005).

Elemental ratio data

Elemental ratios were again calculated to evaluate changes in export production, productivity, and sediment provenance. Ca/Ti, Fe/Ti, and Zr/Ti all display variable downcore patterns throughout the record, especially Ca/Ti (Fig. 8). Ca/Ti contains significant maximum values at 755 and 160 kya and a sustained period of higher values from 400 to 260 kya, but no major minima (Fig. 8). Because of this pattern, we can assume that terrigenous sediment supply to U1479 is variable but contains three significant decreases in supply during the maximum (Fig. 8). Likewise, Fe/Ti contains many maxima but no minima. The most prominent maxima values occur at 1108, 840, 700, 310, and 160 kya (Fig. 8). Zr/Ti displays a similar downcore pattern to Ca/Ti, with two significant maxima centered at 320 and 140 kya (Fig. 8).

Detrital P/Zr increases moderately from 504 kya to 205 kya, decreases sharply from 205 to 165 kya, and then remains generally constant through the end of the record (Fig. 10). P/Zr has a variable but flat average trend and displays no minima but many strong maxima (Fig. 9). The most prominent maximum values occur at 895, 760, 485, and 140 kya. Prior to 500 kya, P/Zr and P/Ti patterns follow each other closely, but after 500 kya they deviate and follow different patterns from each other (Fig. 9). P/Ti rises to a maximum value at approximately 275 kya, then decreases through the end of the record, with far less variance than P/Zr (Fig. 9).

Correlation Coefficients

U1479 displays strong correlations between different elemental concentrations, and like U1474 has large changes in correlation in certain elements over the course of the record. From 1112 to 420 kya, U1479 displays many moderate (± 0.4 to ± 0.59) to high (± 0.6 to ± 0.79)

correlations (Table 8). Mirroring the trend seen in U1474, the highest elemental correlation is between Ca and Ti, with a correlation coefficient of $r=-0.91$. Other significant correlation coefficients are Ca and K ($r=-0.86$), Ti and K ($r=0.78$), and Ti and Zr ($r=0.70$). TP_{TOT} displays weak to moderate correlations with the XRF-derived elemental concentrations, and the highest correlation is between it and Zr ($r=0.43$).

From 420 to 0.8 kya, many correlation coefficients again shift substantially (Table 9). The relationship between Ca and Ti remains strong, $r= -0.90$. Ca and K ($r=-0.79$) and Ti and K ($r=0.75$) retain a strong relationship, and Fe and K's correlation strengthens from moderate ($r=0.53$) to strong ($r=0.64$) (Table 8). Elemental relationships with Zr change significantly after 420 kya. Ti and Zr drop from a strong correlation of $r=0.70$ to a weak correlation of $r=0.36$ (Table 8). The relationships between Ca and Zr ($r=-0.25$) and K and Zr ($r=-0.01$) are also weaker. Interestingly, Zr's relationship strengthens with P ($r=0.52$). All correlation changes are shown in Table 9. Because U1474 and U1479 have different timesteps between datapoints, Pearson correlation coefficients could not be computed and thus were not included in this project.

Table 8. Pearson correlation coefficients of XRF elements and PTOT, U1479. Coefficients are color-coded to denote the strengths of each relationship. **Bold, red** = very high correlation ($\geq \pm 0.8$), **non-bold, red** = high correlation (± 0.6 to ± 0.79), black, non-bold = moderate correlation (± 0.4 to ± 0.59), non-bold, gray = low to negligible correlation ($\leq \pm 0.39$).

Full record (1112 – 0 kya)						
	Ca	Ti	Zr	Fe	K	PTOT
Ca	1	-0.90	-0.34	-0.51	-0.84	-0.31
Ti	--	1	0.49	0.43	0.78	0.32
Zr	--	--	1	-0.07	0.11	0.49
Fe	--	--	--	1	0.59	0.03
K	--	--	--	--	1	0.17
PTOT	--	--	--	--	--	1
1112 – 420 kya						
	Ca	Ti	Zr	Fe	K	PTOT
Ca	1	-0.91	-0.53	-0.48	-0.86	-0.25
Ti	--	1	0.70	0.37	0.78	0.31
Zr	--	--	1	-0.03	0.27	0.43
Fe	--	--	--	1	0.53	0.04
K	--	--	--	--	1	0.19
PTOT	--	--	--	--	--	1
420 – 0.8 kya						
	Ca	Ti	Zr	Fe	K	PTOT
Ca	1	-0.90	-0.25	-0.54	-0.79	-0.35
Ti	--	1	0.36	0.46	0.75	0.33
Zr	--	--	1	-0.11	-0.01	0.52
Fe	--	--	--	1	0.64	0.02
K	--	--	--	--	1	0.17
PTOT	--	--	--	--	--	1

Table 9. Change in Pearson correlation coefficients of XRF elements and P_{TOT}, U1479. Changes are calculated as the difference between the older part of the record (1110 to 492 kya) and the younger part of the record (492 to 0.5 kya). Changes are color-coded according to the degree of change and by increases or decreases in value. **Bold, bright blue** = strong negative change (≥ -0.26), **non-bold, bright blue** = moderate negative change (-0.16 to -0.25), **non-bold, light blue** = weak negative change (-0.06 to -0.15), **non-bold, gray** = negligible change (± 0.05), **non-bold, light orange** = weak positive change (+0.06 to +0.15), **non-bold, bright red** = moderate positive change (+0.16 to +0.25), **bold, bright red** = strong positive change ($\geq +0.26$).

	Ca	Ti	Zr	Fe	K	P _{TOT}
Ca	--	-0.01	-0.28	+0.06	-0.07	+0.10
Ti	--	--	-0.34	+0.09	-0.03	+0.02
Zr	--	--	--	+0.08	-0.28	+0.09
Fe	--	--	--	--	+0.11	-0.02
K	--	--	--	--	--	-0.02
P _{TOT}	--	--	--	--	--	--

PCA and GAM Analysis

Principal Components Analysis was completed for U1479 over the entire record (0.8 to 1112 kya) and, similarly to U1474, examined the relationships between Fe, Ti, Ca, K, Zr, and Total P. The first principal component (PC1) represents 55.12% of the variance in our record, while PC2 and PC3 represent 23.96% and 10.04% respectively (Figure 21). Both PC1 and PC2 displayed significant eigenvectors (3.31 and 1.44), but because U1474 only examined PC1, it will also be the sole focus for U1479.

Similarly to U1474, U1479's first principal component is dominated by Ti and Ca, which have perfectly opposed eigenvectors of 0.52 and -0.52 (Figure 21). Also relevant to PC1 are K, with an eigenvector value of 0.48, and to a lesser extent Fe, with an eigenvector value of 0.36. Total P and Zr show the least influence on PC1 and have very similar eigenvector values of 0.24 and 0.25. The score plot for PC1 of U1479 (Figure 12), along with the PC1 score plot for U1474. U1479's PC1 score plot is very different from the one seen in U1474. It first trends steeply downwards from 1112 to 1000 kya, then its trend remains relatively constant from 1000 kya to 440 kya. It decreases sharply from 440 to 315 kya, then increases equally as steeply from 315 kya to 135 kya. At the end of the record (135 kya to 0.8 kya) it again remains relatively constant. This pattern, like that of U1474, is enhanced and emphasized in the GAM analysis. The GAM of the score plot for PC1 is shown in Figure 13, along with the GAM of U1474.

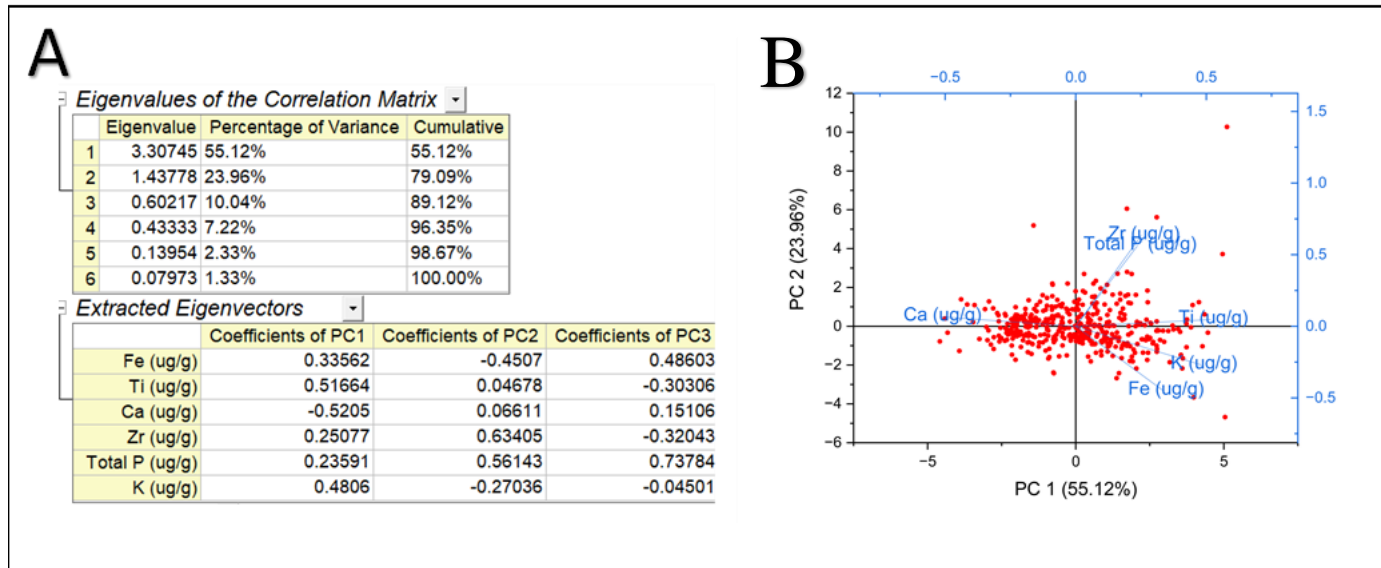


Figure 18. U1479 PCA report data and biplot. Figure 11a displays the calculated eigenvalues of each principal component and their respective share of the total variance, as well as the eigenvector values for each variable used in the PCA. Figure 11b displays the biplot of PC1 and PC2 for U1479. Red dots denote the spread of each individual datapoint in U1479's dataset.

CHAPTER 5

DISCUSSION

Downcore comparisons, U1474 and U1479

When comparing U1474 and U1479, no obvious correlation can be seen between individual XRF records. Elements vary independently of each other, with no trends visible in U1474 carrying over to U1479 downstream. Possible explanations for this are that Site U1474 lies directly within the flow of the Agulhas Current, while Site U1479 does not and instead relies on infrequent terrigenous input through the Agulhas Leakage. Regardless, Ca, and by extension biomass, is much higher in U1479 (mean = 30.1 wt%) than in U1474 (mean = 17.7 wt%), while the terrigenous elemental concentrations in U1474 are higher than in U1479 (Fig. 4). From these observations, we conclude that while primary productivity is greater at site U1479 throughout our record, terrigenous input is greater in the Natal Bight on the same timescale. This is consistent with modern observations and paleorecords of productivity and continental sediment influx for both core sites (Goschen et al., 2015; Gunn et al., 2020; Hood et al., 2017; Jacobs et al., 2022; Krug et al., 2014; Lutjeharms et al., 2000; Meyer et al., 2002; Vinayachandran et al., 2021; Wells et al., 2024).

Across both U1474 and U1479, PTOT displays a consistently variable but constant trend in concentration (Fig. 19). U1479 has more variability than U1474, with larger differences in maxima and minima height especially after 500 kya (Fig. 19). The average PTOT values in our core samples from U1479 are comparable with other Indo-Pacific open ocean settings (217 - 712 ug/g) while U1474's PTOT values are lower than what we would expect (Baturin, 1988; Filippelli, 1997). This discrepancy in U1474 is likely because of the high continental input to the Natal

Bight, and is supported by the initial results from Site U1474, which reported a high fraction of terrigenous clay material to biogenic material ($59\% \pm 15\%$ terrigenous clay, $41\% \pm 15\%$ biogenic material) (Hall, Hemming, LeVay et al., 2017a).

In both U1474 and U1479, P/Ti, used as indicators of changes in export production and new productivity, display strong correlations with our Ca concentrations (U1474 $r=0.83$, U1479 $r=0.70$). Previously we discussed the dilution effect in our samples, where inputs of terrigenous material cause relative Ca concentrations in our sediments to decrease, and vice versa. Because of the strong relationships between our P/Ti export production indicator with Ca, we believe that export production is similarly affected by this dilution effect; as terrigenous input to each site increases, the P/Ti ratio decreases accordingly, and vice versa. P_{TOT} in both sites maintains a relatively constant rate of burial, though U1479 displays a higher degree of variability in P_{TOT} concentrations than U1474 (Fig. 19). We therefore conclude that for both sites, P burial occurs independently of terrigenous material input, and therefore export production and overall productivity rates are largely unaffected by those input changes as well. Export production rates were therefore largely stable throughout our 1.1 mya records at Sites U1474 and U1479, and the variability seen in our P_{TOT} and sequential P datasets is predominantly caused by changes in marine processes rather than continental processes.

As with our XRF results, neither our total P or sequential P data shows any true correlation between U1474 and U1479. Comparing between overall concentrations, P_{TOT} values are significantly higher in U1479 than in U1474, suggesting that overall export production is consistently higher off the southwestern coast of Africa than the Natal Bight throughout our time series, which is consistent with modern observations and paleorecords from the region (Fig. 4;

Diz et al., 2007; Hood et al., 2017; Jacobs et al., 2022; Jebri et al., 2022; Lutjeharms, 2007; Meyer et al., 2002; Tangunan et al., 2021).

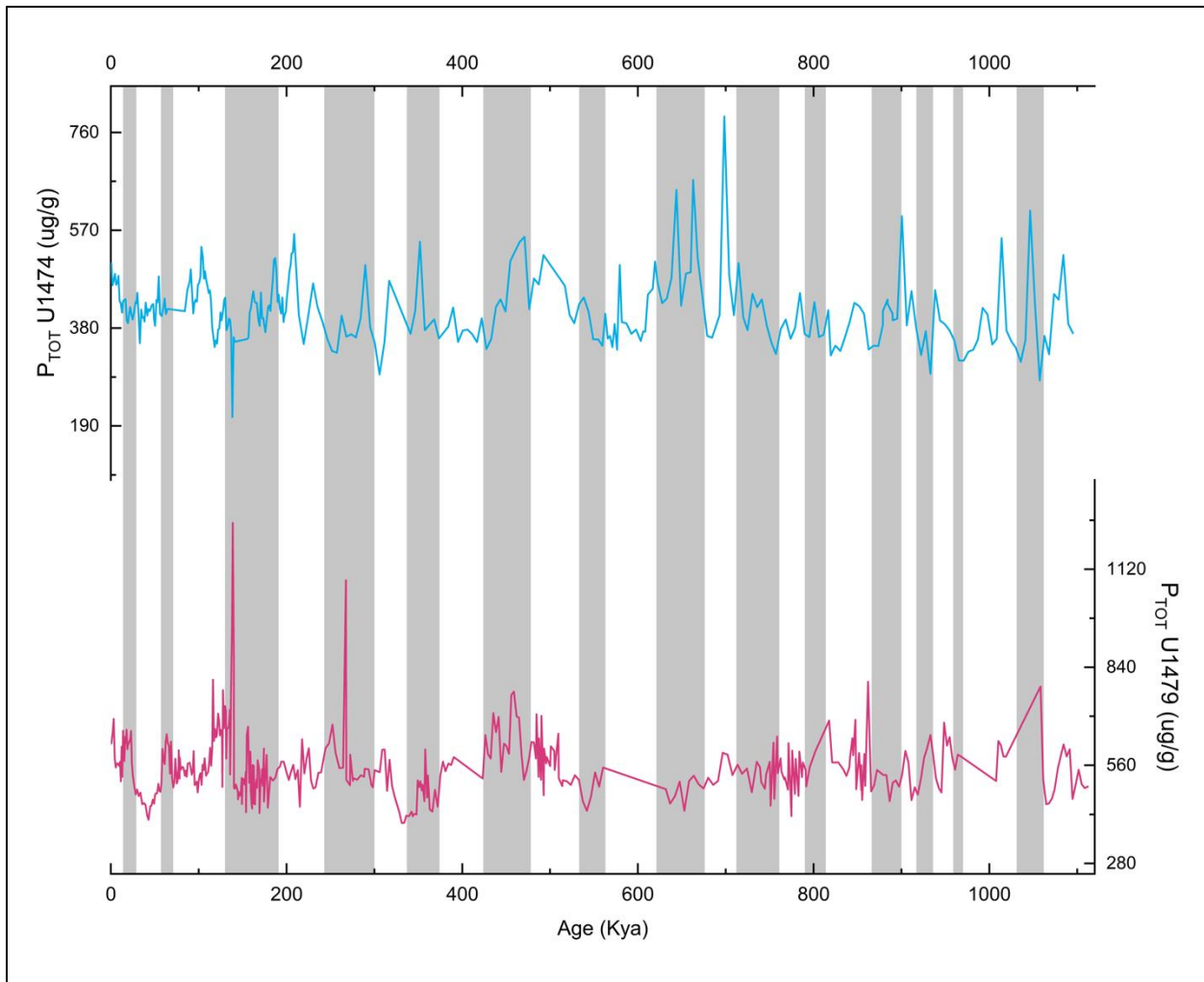


Figure 19. PTOT comparison plots, U1474 and U1479. Gray bars denote approximate timings of glacial cycles, from Lisiecki & Raymo (2005).

Elemental burial variability: potential causes, mechanisms, and implications

Up until this point, we have discussed what our XRF and P data is representative of, how it varies, and when changes occur over the last 1.1 mya in U1474 and U1479. We now must talk

about the processes and conditions that are the potential causes of and driving forces behind these observations.

Site U1474 and the Natal Bight

U1474 and the Natal Bight are ideally positioned to document long-term changes in terrigenous material input from the African continent in response to changing climate dynamics. This is evidenced by our terrigenous indicator data, which show long-term variability in their burial patterns, and in Ca/Ti (Fig. 5 and Fig. 8). We interpret these records to mean that long-term, gradual, large-scale changes to riverine input were taking place throughout this period, likely driven by changes in local hydroclimate. Increases in long-term humidity in the catchments of the Tugela, Zambezi, and Limpopo River systems enhance local weathering and erosion rates. This increases the sediment load of the rivers, and therefore enhances transport and deposition of terrigenous material to U1474. When conditions are drier in southeast Africa, this system reverses, resulting in decreased terrigenous sediment input to the region. Kaboth-Bahr et al. (2021), using multiple proxies, also saw this pattern. When we compare our PC1 record from U1474 with their PC1, our record corresponds well with theirs (Fig. 20). It also builds out an additional 500 kya of proxy data. This reinforces our conclusion that Site U1474's geochemical data is strongly influenced by long-term changes in southeastern African hydroclimate and the east-west moisture dipole (Fig. 20; Kaboth-Bahr et al., 2021).

Using the GAM analysis for our PC1, the trend reveals itself in better detail (Fig. 13). We therefore present the following timeline of events for hydroclimate and terrigenous input in southeastern Africa and the resulting effects on the geochemistry of sediments in Site U1474:

- From 1,110 to 985 kya, a major change from dry conditions to wet conditions takes place in southeastern Africa. Erosion is enhanced in the region, terrigenous material loads

increase in all river catchments, are transported to the coast and enter the western Indian Ocean. The flow of the Agulhas Current then transports the material along the coast to the Natal Bight, where a portion of it is deposited as detrital material.

- From 985 to 775 kya, the hydroclimate of southeastern Africa remains moderately wet, continuing to cause enhanced erosion in the river catchments and leads to higher deposition of terrigenous material in the Natal Bight.
- From 775 to 665 kya, conditions begin to flip from wet to dry in southeastern Africa, and a long dry period that peaks at 500 kya occurs. Erosion and riverine input of sediments decrease in response to the change in hydroclimate, and the supply of terrigenous sediment to the Natal Bight and U1479 drops. In response, new primary productivity and export production are enhanced, and peak at the height of dry conditions in southeastern Africa.
- Conditions again begin to shift to a wet regime from 500 kya to 275 kya, and from 275 to 0.5 kya enhanced erosion, riverine transport, and high deposition of terrigenous material resumes at Site U1474. This wet period peaks around 145 kya and has been weakening through the most modern samples in our dataset.

Throughout the entire record, P_{TOT} burial rates are variable but generally constant, and we conclude that export production and productivity rates are also likely constant (Fig. 19).

The first principal component in Kaboth-Bahr et al. (2021) shows a strong correlation with insolation, specifically corresponding to eccentricity and precession cycles. They assert that this is the driving mechanism behind the changes to southern African hydroclimate (Kaboth-Bahr et al., 2021). Despite our record's lack of orbital tuning and some

discrepancies in the alignment of peaks, long-term eccentricity and eccentricity-driven precession appear to correlate with our PC1 plot as well (Fig. 20). The REDFIT spectral analysis of U1474's PC1 also showed a strong peak at the frequency corresponding with a 107 kya periodicity, aligning with the 105 kya eccentricity cycle (Fig. 14). Our record is not long enough to conclusively say that the 400-kya cycle of eccentricity correlates with our data, however this also appears to be a trend in our PC1 record. It is also important to note that throughout our record for U1474, glacial-interglacial variations do not seem to have any effect on changes to either terrigenous input or export production, which is also a conclusion in Kaboth-Bahr et al. (2021). We therefore conclude that changes in insolation and its effect on precipitation is the primary control on long-term variability in the biogeochemical processes in the Natal Bight.

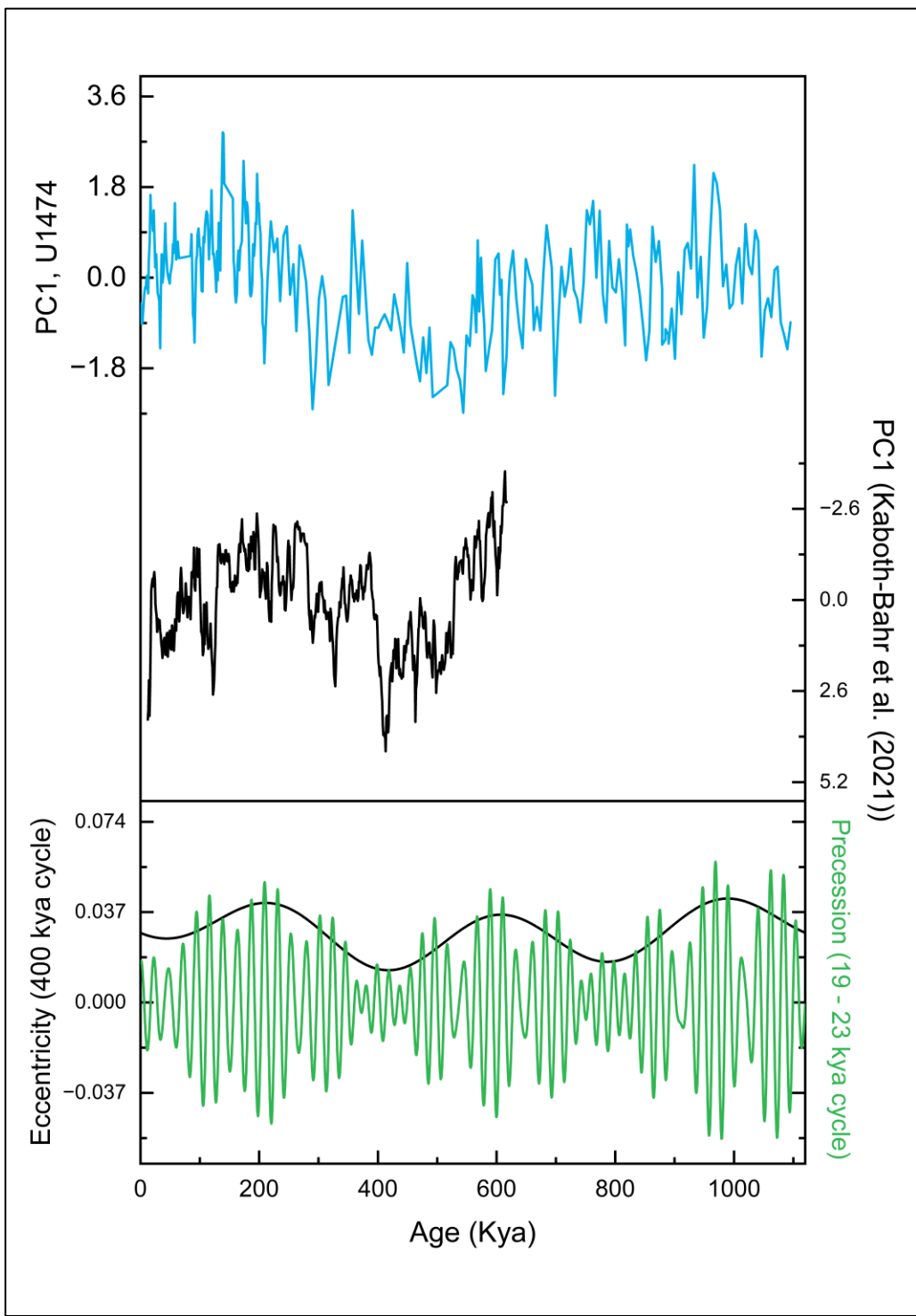


Figure 20. U1474 PC1 comparison with Kaboth-Bahr et al. (2021) PC1 hydroclimate graph. Positive values in our plot correspond with wetter conditions in east Africa, while negative values correspond with wetter conditions in west Africa. Our bottom plot shows both PCA's correspondence with 400-kya eccentricity cycle (black curve) and 19 to 23-kya precession cycles (green curve). Insolation curves are derived from Laskar et al. (2004).

Site U1479 and the Agulhas Leakage

Because of U1479's unique hydrography and variable connection to the Agulhas Current over short and long timescales, it is sensitive to many different regional and global climate changes that take place during the Quaternary. These include:

- Changes in orbitally driven glacial cyclicity from obliquity-dominated to eccentricity-dominated before and after the MPT (1250 to 700 kya).
- Further intensification of glacial-interglacial cycles following the beginning of the MBE (~420 kya).
- Intensification of the variability of global and regional sea level, resulting in longer periods of higher exposure of the Agulhas Bank region.
- Both a long-term intensification of the Agulhas Leakage after 400 kya, and short-term periods of intense Agulhas Leakage centered at 800, 400, and 100 kya (Fig. 21; Caley et al., 2012).
- The previously discussed long-term shifts in southern African hydroclimate (Kaboth-Bahr et al., 2021).

A final important factor affecting sediment input to U1479 is sediment transport distance. Sediment entering the flow of the Agulhas Current in southeastern Africa is carried downstream, decreasing in concentration as an increasing fraction of the total sediment load is deposited along the African Coast. For U1479, this means that even during times of enhanced input in eastern Africa, the sediment that eventually reaches the area will contain a much lower concentration than what is deposited in U1474, regardless of processes that affect climate or Agulhas Leakage strength. Combining all these factors with our observations for Site U1479 results in a complex

timeline of events, with many overlapping periods of change. When simplified to events centered around our terrigenous data, however, five distinct periods and one subperiod stand out. These are listed here and visualized in Figure 23.

Interval 1: From 1112 to 900 kya, detrital sediment concentrations remain generally constant but show strong variability, consistently changing between high and low values (Fig. 15). We interpret this to be a period of variable input of terrigenous material to the Agulhas Leakage Corridor. During this period, southeast Africa shifts rapidly from dry conditions to a sustained moderately wet period according to our hydroclimate record from site U1474 (Fig. 20). This large change likely led to increased sediment erosion and higher loads of terrigenous sediment in rivers. The sediment supply to the Agulhas Current and Site U1474 would have been high and is reflected in our record from the Natal Bight, but the effects of long-distance sediment transport and long-term suppression of Agulhas leakage means that most of the sediment would not reach Site U1479 or would only reach it during intervals of leakage. Records from nearby sediment cores show that overall Agulhas Leakage was low but still occurring at infrequent intervals, and would likely explain the oscillating pattern in our record (Fig. 21; Caley et al., 2012).

Interval 2: From 900 to 720 kya, a maximum centered at 800 kya is seen in our terrigenous element concentration data (Fig. 15). The timing of the terrigenous element maximum corresponds with a short-term period of more intense Agulhas Leakage, during the sustained peak in wet conditions in southeastern Africa (Fig. 20 and 21; Caley et al., 2012). We therefore attribute the increases in terrigenous material in U1479 to sustained high erosion in southeast Africa, continued high riverine input of material to the Agulhas Current, transport downstream, and eventual deposition at higher concentrations in the Agulhas Leakage Corridor.

Interval 3: From 720 to 500 kya, our terrigenous indicators increase and maintain a long, sustained maximum in concentration (Fig. 15). This sustained period of elevated terrigenous material is likely due to a large combination of factors. The MPT ends at 700 kya, which means that longer, more intense global glacial and interglacial cycles start to become common (Cartagena-Sierra et al., 2021; Imbrie et al., 1993). The east-west hydroclimate dipole switches from a moderately wet eastern Africa and dry western Africa to a dry eastern Africa and wet western Africa (Fig. 20; Kaboth-Bahr et al., 2021). The result of this is a decrease in riverine input in southeastern Africa, and lower concentrations of continentally derived sediment from this region reaching site U1479. However, a wetter west Africa would result in increased erosion of material which would be transported to the southern coast of Africa and eventually to the Agulhas Leakage Corridor (Dingle & Rogers, 1972; Kaboth-Bahr et al., 2021). The volume of sediment entering the Agulhas current in western Africa would be much higher than the sediment load coming from southeast Africa. Long-term Agulhas Leakage is still suppressed (Fig. 21; Caley et al., 2012); however, so much sediment is being carried by the current during this time that the overall concentration of terrigenous sediment being deposited at U1479 increases.

Interval 4: From 500 to 300 kya, several more shifts in our record and in the climate take place. Ti and K start high and decrease gradually, but Zr deviates from this and begins to follow a different trend (Fig. 22). Ignoring Zr for now, the large increase in biotic activity and corresponding decrease in terrigenous input can be attributed to several different factors. On a global scale, the MBE begins around 420 kya and further enhances the differences between glacial and interglacial cycles, making the extremes more intense (Imbrie et al., 1993). Western Africa is still within a wet cycle, but the climate dipole is beginning to switch again to a wetter east Africa and drier west Africa (Fig. 20; Foerster et al., 2022; Kaboth-Bahr et al., 2021). As a

result, rainfall and thus erosion begin decreasing in western Africa, reducing the localized sediment supply. It is still technically dry in eastern Africa, and despite increasing erosion and riverine transport to the ocean, levels are not yet high enough to make a noticeable difference at Site U1479 because of the long distance the sediment is transported through the Agulhas Current, further reducing already low concentrations. Despite the changepoint from less intense to more intense leakage that takes place during this time (Fig. 21, around 400 kya), and a short-term period of intensified Agulhas Leakage centered at 400 kya, sediment supply from southeast Africa is low enough to not make a difference in the trend. Therefore, the localized signal of west Africa dominates the weaker signal of east Africa, and southwest Africa's drying trend is the dominant signal being expressed in U1479 over this period (Dupont et al., 2022; Kaboth-Bahr et al., 2021).

Subinterval 4.5 – Zr, total P, and sequential P data: Independent of our terrigenous data in Intervals 4 and 5, from 500 kya to 0.8 kya Zr and some P concentrations begin to show correlations with glacial-interglacial cycles (Fig. 22). During glacial intervals, peaks in the records of Zr, detrital P, P_{TOT} , and authigenic P are recorded in U1479 (Fig. 22). Likewise, small dips in concentrations are recorded during interglacial periods. Correlation coefficients also change prior to and following 500 kya; Zr becomes more closely associated with P_{TOT} , while its relationships with Ti, Ca and K weaken considerably (Table 9). A major change in provenance for site U1479's sediments would typically be indicated by these kinds of changes, but we propose an alternative explanation.

In the primary rock formations in southern Africa that supply sediment to the Agulhas Current, Ti values far exceed Zr in every case, and at equivalent ratios (Foerster et al., 2022; Fourie, 2010; Garzanti et al., 2022; Schüürman et al., 2019). As a result, changes in hydroclimate

from eastern to western southern Africa, and thus a change in provenance, would not elicit a strong deviation in Zr from Ti and K. Their ratio in the sediments remains largely the same across the entire southern portion of the continent A source of Zr, detrital P, and authigenic P independent of Ti is also unlikely for this core site, because large-scale changes in hydrography would need to take place in either the Agulhas Current or Site U1479, and no such evidence exists of this over the last few million years (Babin, 2023). Instead, we propose that a combination of factors already discussed in this project caused the change in trend. MBE-centered intensification of glacial cycles in southern Africa led to prolonged, larger exposures of the Agulhas Bank. Longer exposures of the continental shelf during glacial periods allowed for enhanced erosion of deposits of combined terrigenous-sourced and marine-sourced material (Dingle & Rogers, 1972; Dupont et al., 2011; Hahn et al., 2018). This resuspended material was then transported to Site U1479 by the enhanced Agulhas Leakage, and was redeposited, leading to higher concentrations in our samples. This was also aided by increasing wet conditions in western Africa, which enhanced erosion rates of the bank and shelf further (Foerster et al., 2022; Kaboth-Bahr et al., 2021). P_{TOT} rates also display elevated concentrations during these glacial intervals, especially during MIS 2, 4, 6, 8, and 12 (Fig. 19), suggesting increased productivity rates and export production. These spikes were likely caused by the resuspended shelf nutrients.

There remains the issue of the drop in correlation between Ti, K, and Zr, and why Ti and K do not register the same peaks in material during glacial cycles. Our solution is likely tied to the effects of transporting sediments a long distance for U1479, and the geochemistry of the original source rocks in southern Africa. As previously stated, Ti exists in much higher concentrations than Zr in the bedrock of southern Africa. When it is eroded and enters the Indian Ocean through river systems in the southeast, Zr is already at a lower concentration than Ti. Both

Ti and Zr's concentrations then decrease proportionally due to the distance they are transported from U1474 to U1479. By the time the sediments are deposited in U1479, Zr's concentration only averages around 60 ppm, while Ti is still high related to Zr at an average of 666 ppm (Table 7). The primary minerals containing Ti and Zr in the host rocks of southern Africa are rutile and zircon (Fourie, 2010; Garzanti et al., 2022; Hahn et al., 2018; Schüürman et al., 2019). Rutile has a much lower molecular weight than zircon (79.88 g/mol vs. 183.30 g/mol), and as a result would not be able to be transported as far, regardless of its distance from the source (Nesse, 2017). Because of both factors, Ti starts at a high concentration and remains generally high as it moves through the Agulhas Current to U1479. A smaller signal like the glacial/interglacial cycle variability seen in Zr, detrital P, and authigenic P would be overwhelmed by the stronger influx of material from southeastern Africa through the Agulhas Leakage. Therefore, Zr's low starting concentrations would enhance the small variability signal caused by glacial interglacial cycles, while Ti would suppress it.

Interval 5: From 300 to 0.8 kya, Ti and K greatly increase in concentration overall (Fig. 15). The hydroclimate dipole again denotes very wet conditions in southeastern Africa that peak at 150 kya and then decrease markedly through the end of our record (Fig. 20; Kaboth-Bahr et al., 2021). This again means that increased erosion and transport of continental sediments to the western Indian Ocean and the Agulhas Current is happening, and the sediment is eventually transported downstream. Unlike the previous wet period in southeastern Africa, long-term Agulhas Leakage is more intense, and so more of the distant-sourced sediment can make it to site U1479 at higher concentrations and be deposited. Even when conditions start to shift back to drier in the east and wetter in the west, the return to localized input keeps detrital element concentration levels high at U1479 through the end of our record (Fig. 15).

As in U1474, U1479's P data displays short-term variability but maintains a constant trend, and we conclude that export production and overall P burial must also be constant throughout our 1.1 mya record (Fig. 19).

This timeline of events at Site U1479 serves to highlight the complexity of the mechanisms that affect inputs and burial of all sediment types in the Agulhas Ring Corridor. Our record shows that short and long changes in hydroclimate in both southeastern and southwestern Africa exert profound effects on sediment transport to the site. Meanwhile the Agulhas Leakage controls the amount of sediment passing through the ring corridor regardless of the amount of input. Orbital-scale changes to glacial-interglacial cycles, and glacial-interglacial cycles later in our record, also cause large changes in sediment burial here. Finally, our understanding of sediment burial dynamics at U1479 has shown to be heavily reliant on the bedrock geology of southern Africa and is why we are able to see glacial-interglacial changes at all.

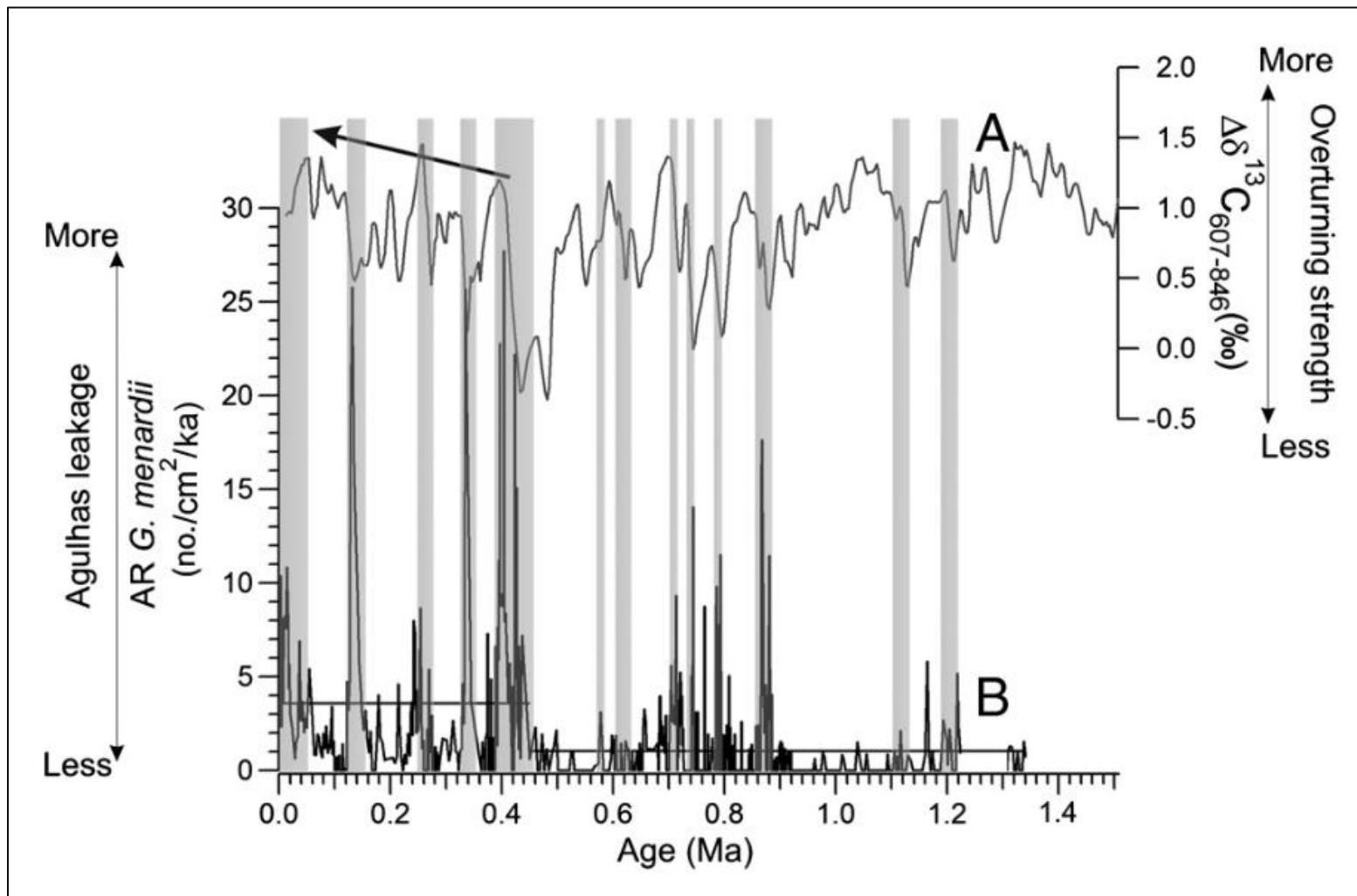


Figure 21. Links between Agulhas Leakage strength and ocean overturning strength, from Caley et al. (2012). The foraminifera *G. menardii* is used as an indicator of enhanced periods of leakage at ODP Site 1087, nearby to Site U1479 off the Agulhas Bank. Higher peaks of the presence of the species on short-term timescales occur centered at 800 kya, 400 kya, and 100 kya. A long-term changepoint in Agulhas Leakage intensity occurs at 400 kya, and is indicated by the horizontal lines in mean *G. menardii* counts.

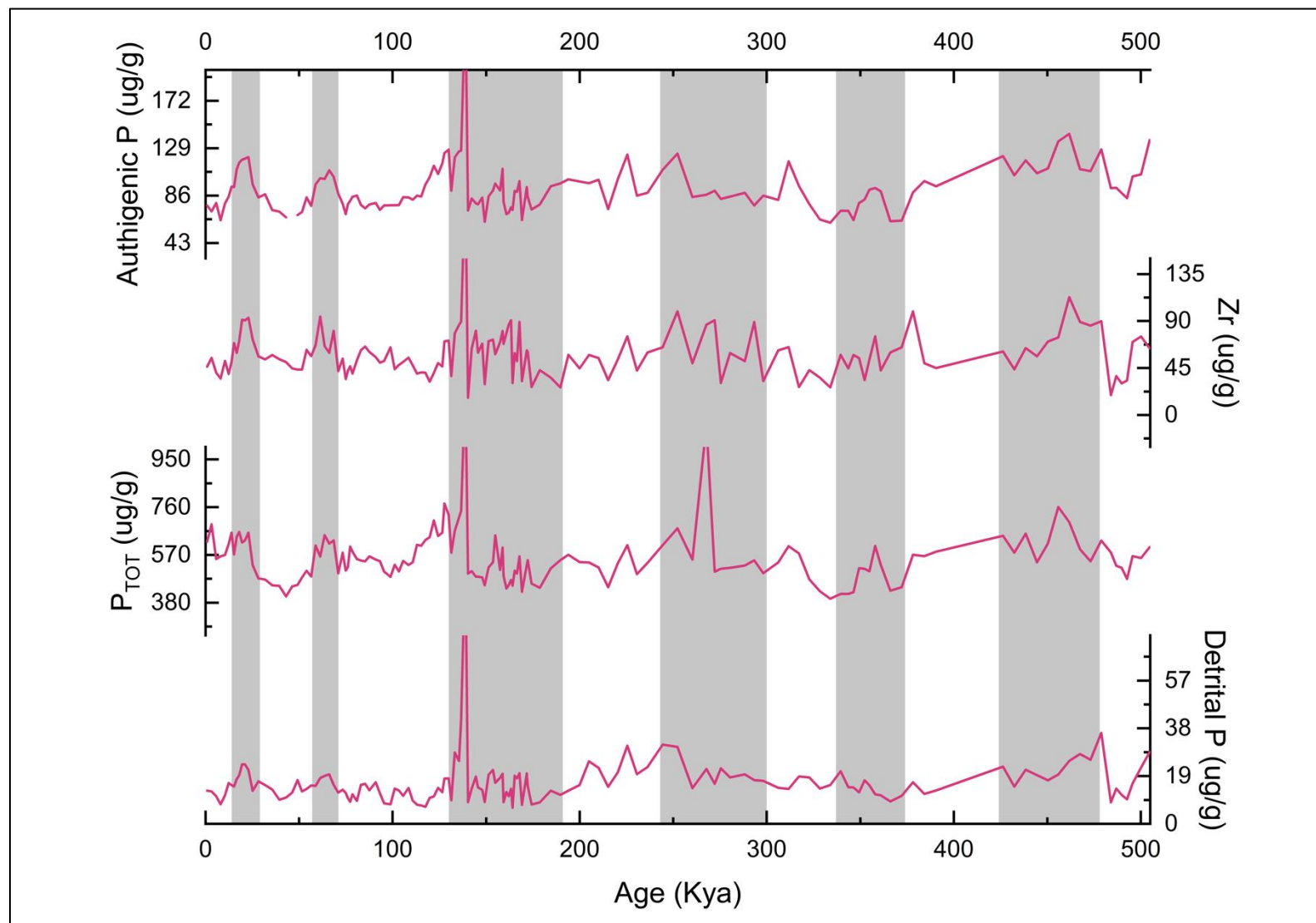


Figure 22. U1479 XRF and P data with glacial period correlations. Gray bars denote approximate timings of glacial cycles, from Lisiecki & Raymo (2005).

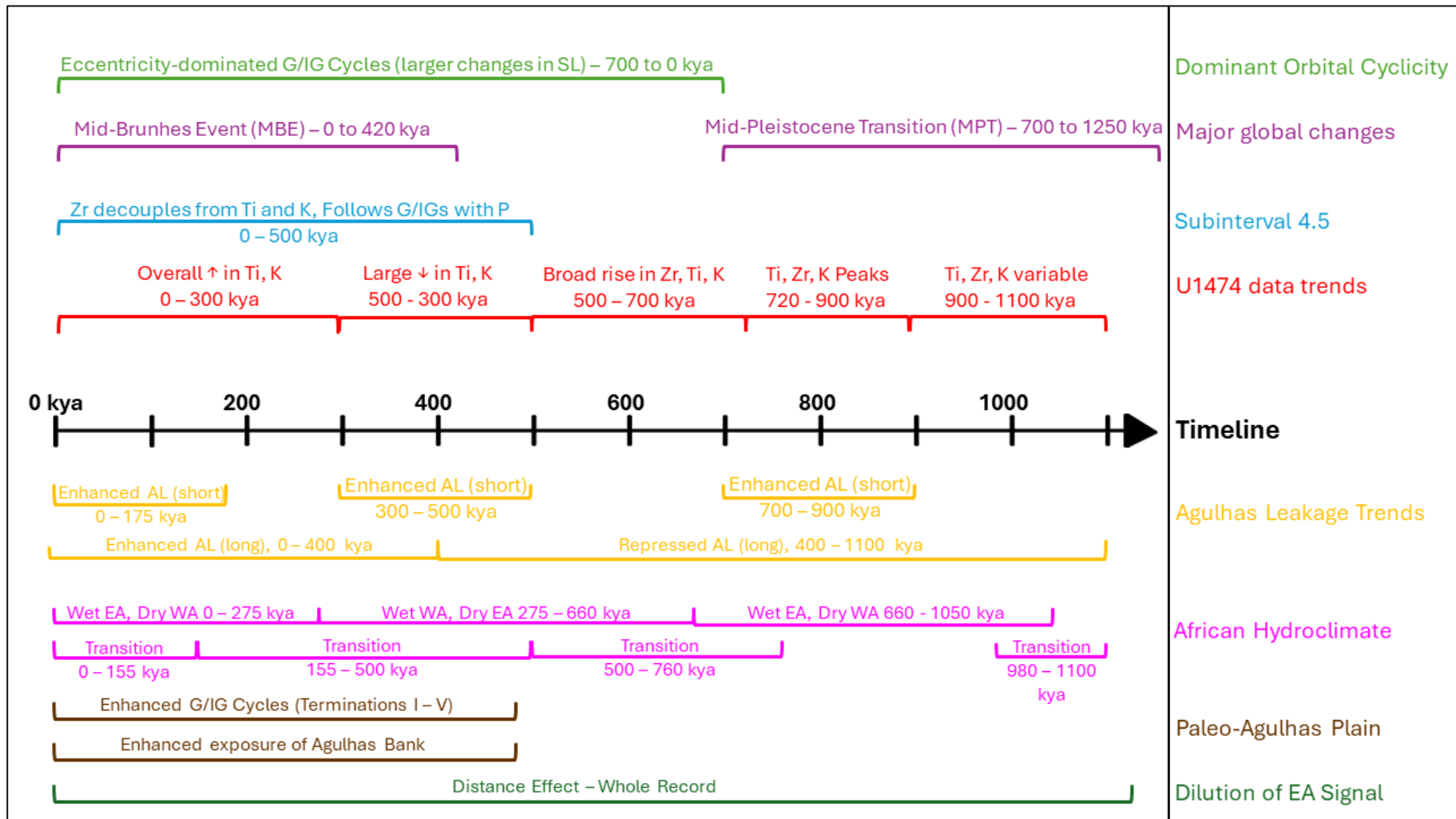


Figure 23. Timeline of changes at Site U1479. For detailed description see discussion. Timing of intervals and subinterval 4.5 based on our Ti/K data and Zr data. Timing of MBE and MPT from Imbrie et al. (1993). Timing of Agulhas Leakage Enhancement from Caley et al. (2012). Timeline of African hydroclimate change from our data and Kaboth-Bahr et al. (2021).

CHAPTER 6

CONCLUSIONS

In this project, we explored how sediment burial varied off the coast of southern Africa over the last 1100 kya, and what effects regional and global climate trends had on the biogeochemistry of the sediments. Site U1474 in the Natal Bight was shown to be heavily reliant on processes that affect southeastern African climate, especially hydroclimate changes and Earth's orbital parameters. Site U1479 in the Agulhas Ring Corridor was shown to be influenced by southeastern and southwestern hydroclimate, variability in Agulhas Leakage intensity, large-scale changes in orbital forcing, glacial/interglacial cyclicity, and the surface geology of southern Africa and the Agulhas Bank. Trends in elemental burial in U1479 did not necessarily reflect trends in elemental burial in U1474. Despite this, their sustained connection via the Agulhas Current and dependence on many of the same processes for terrigenous sediment delivery asserts that Site U1479's burial dynamics are at least partly influenced by Site U1474's burial dynamics. In addition to our findings and timelines of processes at play at our two core sites, our research extends the long-term record of hydroclimate change in southern Africa.

When we began this project, we proposed three general hypotheses:

1. Primary productivity rates were consistently higher in U1479 than U1474 over the last 1.1 mya, but continental sediment influx was consistently higher in U1474 than U1479.

Our XRF and P data proved this statement to be accurate. Higher terrigenous input was consistently seen in U1474 than in U1479 over the last 1100 kya, while Ca and P data indicates

that higher rates of primary productivity and export production have consistently been present in U1479 over U1474.

2. Orbital cycle variability strongly influenced nutrient and associated elemental cycling in the Agulhas Current over the last 1.1 mya.

This statement is partially correct. Site U1474's data demonstrated the influence of eccentricity and eccentricity-driven precession on hydroclimate and continental input to the Agulhas Current. While the influence of the 400-kyr eccentricity cycle is visually observable in U1479's terrigenous material data, the preliminary age model was not suitable for spectral analysis. As a result, the dominance of any one orbital parameter over the other for Site U1479's nutrient and elemental cycling could not be determined.

3. U1479 and U1474 did not always have a strong teleconnection and may have been disconnected during glacial lowstands, accounting for differences in each record.

This statement is mostly incorrect. Processes affecting U1474 also affect U1479, and despite variability in Agulhas Leakage over short and long time periods, leakage persists and keeps both core sites connected throughout our record. There is no evidence of sustained disconnection during glacial lowstands.

Sequential extractions for both U1474 and U1479 only covered the most recent 500 kya of our record, and at a low sampling resolution. Longer, higher-resolution records are necessary to make full assessments of nutrient burial processes in both cores.

REFERENCES

- Anderson, L. D., & Delaney, M. L. (2000). Sequential extraction and analysis of phosphorus in marine sediments: Streamlining of the SEDEX procedure. *Limnology and Oceanography*, 45(2), 509–515. <https://doi.org/10.4319/lo.2000.45.2.0509>
- Ao, H., Rohling, E. J., Stringer, C., Roberts, A. P., Dekkers, M. J., Dupont-Nivet, G., Yu, J., Liu, Q., Zhang, P., Liu, Z., Ma, X., Zhou, W., Jin, Z., Xiao, G., Wang, H., Sun, Q., Yang, P., Peng, X., Shi, Z., ... An, Z. (2020). Two-stage mid-Brunhes climate transition and mid-Pleistocene human diversification. *Earth-Science Reviews*, 210, 103354. <https://doi.org/10.1016/j.earscirev.2020.103354>
- Arrigo, K. R. (2005). Marine microorganisms and global nutrient cycles. *Nature*, 437(7057), Article 7057. <https://doi.org/10.1038/nature04159>
- Babin, D. P. (2023). *Mid-Pleistocene-To-Present Southeast African Hydroclimate and Deep Water Regimes* [Ph.D., Columbia University]. <https://www.proquest.com/docview/2792179766/abstract/9AFEEDB04B8443ACPQ/1>
- Bard, E., & Rickaby, R. E. M. (2009). Migration of the subtropical front as a modulator of glacial climate. *Nature*, 460(7253), Article 7253. <https://doi.org/10.1038/nature08189>
- Baturin, G. N. (1988). Disseminated phosphorus in oceanic sediments—A review. *Marine Geology*, 84(1), 95–104. [https://doi.org/10.1016/0025-3227\(88\)90127-2](https://doi.org/10.1016/0025-3227(88)90127-2)
- Beal, L. M., & Bryden, H. L. (1999). The velocity and vorticity structure of the Agulhas Current at 32°S. *Journal of Geophysical Research: Oceans*, 104(C3), 5151–5176. <https://doi.org/10.1029/1998JC900056>
- Benitez-Nelson, C. R. (2000). The biogeochemical cycling of phosphorus in marine systems. *Earth-Science Reviews*, 51(1), 109–135. [https://doi.org/10.1016/S0012-8252\(00\)00018-0](https://doi.org/10.1016/S0012-8252(00)00018-0)

- Biastoch, A., Böning, C. W., & Lutjeharms, J. R. E. (2008). Agulhas leakage dynamics affects decadal variability in Atlantic overturning circulation. *Nature*, 456(7221), Article 7221. <https://doi.org/10.1038/nature07426>
- Böning, P., Bard, E., & Rose, J. (2007). Toward direct, micron-scale XRF elemental maps and quantitative profiles of wet marine sediments. *Geochemistry, Geophysics, Geosystems*, 8(5). <https://doi.org/10.1029/2006GC001480>
- Caley, T., Extier, T., Collins, J. A., Schefuß, E., Dupont, L., Malaizé, B., Rossignol, L., Souron, A., McClymont, E. L., Jimenez-Espejo, F. J., García-Comas, C., Eynaud, F., Martinez, P., Roche, D. M., Jorry, S. J., Charlier, K., Wary, M., Gourves, P.-Y., Billy, I., & Giraudeau, J. (2018). A two-million-year-long hydroclimatic context for hominin evolution in southeastern Africa. *Nature*, 560(7716), 76–79. <https://doi.org/10.1038/s41586-018-0309-6>
- Caley, T., Giraudeau, J., Malaizé, B., Rossignol, L., & Pierre, C. (2012). Agulhas leakage as a key process in the modes of Quaternary climate changes. *Proceedings of the National Academy of Sciences*, 109(18), 6835–6839. <https://doi.org/10.1073/pnas.1115545109>
- Caley, T., Kim, J.-H., Malaizé, B., Giraudeau, J., Laepple, T., Caillon, N., Charlier, K., Rebaubier, H., Rossignol, L., Castañeda, I. S., Schouten, S., & Sinninghe Damsté, J. S. (2011). High-latitude obliquity as a dominant forcing in the Agulhas current system. *Climate of the Past*, 7(4), 1285–1296. <https://doi.org/10.5194/cp-7-1285-2011>

- Cartagena-Sierra, A., Berke, M. A., Robinson, R. S., Marcks, B., Castañeda, I. S., Starr, A., Hall, I. R., Hemming, S. R., LeVay, L. J., & Party, E. 361 S. (2021). Latitudinal Migrations of the Subtropical Front at the Agulhas Plateau Through the Mid-Pleistocene Transition. *Paleoceanography and Paleoclimatology*, 36(7), e2020PA004084.
<https://doi.org/10.1029/2020PA004084>
- Castañeda, I. S., Caley, T., Dupont, L., Kim, J.-H., Malaizé, B., & Schouten, S. (2016). Middle to Late Pleistocene vegetation and climate change in subtropical southern East Africa. *Earth and Planetary Science Letters*, 450, 306–316.
<https://doi.org/10.1016/j.epsl.2016.06.049>
- Catuneanu, O., Guiraud, R., Eriksson, P., Thomas, B., Shone, R., & Key, R. (2005). Phanerozoic evolution of Africa. *Journal of African Earth Sciences*, 43(1), vii–ix.
<https://doi.org/10.1016/j.jafrearsci.2005.09.001>
- Charles, C. (2024). *Unpublished Dataset* [dataset].
- Daher, H., Beal, L. M., & Schwarzkopf, F. U. (2020). A New Improved Estimation of Agulhas Leakage Using Observations and Simulations of Lagrangian Floats and Drifters. *Journal of Geophysical Research: Oceans*, 125(4), e2019JC015753.
<https://doi.org/10.1029/2019JC015753>
- Defforey, D., & Paytan, A. (2018). Phosphorus cycling in marine sediments: Advances and challenges. *Chemical Geology*, 477, 1–11.
<https://doi.org/10.1016/j.chemgeo.2017.12.002>
- Delany, A. C., Claire Delany, A., Parkin, D. W., Griffin, J. J., Goldberg, E. D., & Reimann, B. E. F. (1967). Airborne dust collected at Barbados. *Geochimica et Cosmochimica Acta*, 31(5), 885–909. [https://doi.org/10.1016/S0016-7037\(67\)80037-1](https://doi.org/10.1016/S0016-7037(67)80037-1)

- Dingle, R. V., & Rogers, J. (1972). Pleistocene Palaeogeography of the Agulhas Bank. *Transactions of the Royal Society of South Africa*, 40(3), 155–165.
<https://doi.org/10.1080/00359197209519415>
- Diz, P., Hall, I. R., Zahn, R., & Molyneux, E. G. (2007). Paleoceanography of the southern Agulhas Plateau during the last 150 ka: Inferences from benthic foraminiferal assemblages and multispecies epifaunal carbon isotopes. *Paleoceanography*, 22(4).
<https://doi.org/10.1029/2007PA001511>
- Duhamel, S., Diaz, J. M., Adams, J. C., Djaoudi, K., Steck, V., & Waggoner, E. M. (2021). Phosphorus as an integral component of global marine biogeochemistry. *Nature Geoscience*, 14(6), Article 6. <https://doi.org/10.1038/s41561-021-00755-8>
- Dupont, L. M., Caley, T., Kim, J.-H., Castañeda, I., Malaizé, B., & Giraudeau, J. (2011). Glacial-interglacial vegetation dynamics in South Eastern Africa coupled to sea surface temperature variations in the Western Indian Ocean. *Climate of the Past*, 7(4), 1209–1224. <https://doi.org/10.5194/cp-7-1209-2011>
- Dupont, L. M., Zhao, X., Charles, C., Faith, J. T., & Braun, D. (2022). Continuous vegetation record of the Greater Cape Floristic Region (South Africa) covering the past 300 000 years (IODP U1479). *Climate of the Past*, 18(1), 1–21.
<https://doi.org/10.5194/cp-18-1-2022>
- Dyez, K. A., Zahn, R., & Hall, I. R. (2014). Multicentennial Agulhas leakage variability and links to North Atlantic climate during the past 80,000 years. *Paleoceanography*, 29(12), 1238–1248. <https://doi.org/10.1002/2014PA002698>

- Eglington, B. M., & Armstrong, R. A. (2004). The Kaapvaal Craton and adjacent orogens, southern Africa: A geochronological database and overview of the geological development of the craton. *South African Journal of Geology*, 107(1–2), 13–32. <https://doi.org/10.2113/107.1-2.13>
- Filippelli, G. M. (1997). Controls on phosphorus concentration and accumulation in oceanic sediments. *Marine Geology*, 139(1), 231–240. [https://doi.org/10.1016/S0025-3227\(96\)00113-2](https://doi.org/10.1016/S0025-3227(96)00113-2)
- Filippelli, G. M., Latimer, J. C., Murray, R. W., & Flores, J.-A. (2007). Productivity records from the Southern Ocean and the equatorial Pacific Ocean: Testing the glacial Shelf-Nutrient Hypothesis. *Deep Sea Research Part II: Topical Studies in Oceanography*, 54(21), 2443–2452. <https://doi.org/10.1016/j.dsr2.2007.07.021>
- Flores, J., Filippelli, G., Sierro, F., & Latimer, J. (2012). The “White Ocean” Hypothesis: A Late Pleistocene Southern Ocean Governed by Coccolithophores and Driven by Phosphorus. *Frontiers in Microbiology*, 3. <https://www.frontiersin.org/articles/10.3389/fmicb.2012.00233>
- Foerster, V., Asrat, A., Bronk Ramsey, C., Brown, E. T., Chapot, M. S., Deino, A., Duesing, W., Grove, M., Hahn, A., Junginger, A., Kaboth-Bahr, S., Lane, C. S., Opitz, S., Noren, A., Roberts, H. M., Stockhecke, M., Tiedemann, R., Vidal, C. M., Vogelsang, R., ... Trauth, M. H. (2022). Pleistocene climate variability in eastern Africa influenced hominin evolution. *Nature Geoscience*, 15(10), 805–811. <https://doi.org/10.1038/s41561-022-01032-y>

- Fourie, P. H. (2010). *Provenance and Paleotectonic Setting of the Devonian Bokkeveld Group, Cape Supergroup, South Africa* [M.Sc., University of Johannesburg (South Africa)].
<https://www.proquest.com/docview/2572693832/abstract/90951C3D88AA467CPQ/1>
- Franzese, A. M., Hemming, S. R., & Goldstein, S. L. (2009). Use of strontium isotopes in detrital sediments to constrain the glacial position of the Agulhas Retroflection. *Paleoceanography*, 24(2). <https://doi.org/10.1029/2008PA001706>
- Franzese, A. M., Hemming, S. R., Goldstein, S. L., & Anderson, R. F. (2006). Reduced Agulhas Leakage during the Last Glacial Maximum inferred from an integrated provenance and flux study. *Earth and Planetary Science Letters*, 250(1), 72–88.
<https://doi.org/10.1016/j.epsl.2006.07.002>
- Galvão, J. C. M., Ayres Neto, A., Vieira, R., & Simões, J. C. (2023). Elemental and mineralogical characterization of marine sediments and their relationship to sedimentary and oceanographic processes in Central Bransfield Basin. *Anais Da Academia Brasileira de Ciências*, 95, e20230990. <https://doi.org/10.1590/0001-3765202320230990>
- Garzanti, E., Bayon, G., Dinis, P., Vermeesch, P., Pastore, G., Resentini, A., Barbarano, M., Ncube, L., & Van Niekerk, H. J. (2022). The Segmented Zambezi Sedimentary System from Source to Sink: 2. Geochemistry, Clay Minerals, and Detrital Geochronology. *The Journal of Geology*, 130(3), 171–208. <https://doi.org/10.1086/719166>
- Garzanti, E., Pastore, G., Resentini, A., Vezzoli, G., Vermeesch, P., Ncube, L., Niekerk, H. J. V., Jouet, G., & Dall'Asta, M. (2021). The Segmented Zambezi Sedimentary System from Source to Sink: 1. Sand Petrology and Heavy Minerals. *The Journal of Geology*, 129(4), 343–369. <https://doi.org/10.1086/715792>

- Goschen, W. S., Bornman, T. G., Deyzel, S. H. P., & Schumann, E. H. (2015). Coastal upwelling on the far eastern Agulhas Bank associated with large meanders in the Agulhas Current. *Continental Shelf Research*, 101, 34–46. <https://doi.org/10.1016/j.csr.2015.04.004>
- Gottschalk, J., Hodell, D. A., Skinner, L. C., Crowhurst, S. J., Jaccard, S. L., & Charles, C. (2018). Past Carbonate Preservation Events in the Deep Southeast Atlantic Ocean (Cape Basin) and Their Implications for Atlantic Overturning Dynamics and Marine Carbon Cycling. *Paleoceanography and Paleoclimatology*, 33(6), 643–663. <https://doi.org/10.1029/2018PA003353>
- Gunn, K. L., Beal, L. M., Elipot, S., McMonigal, K., & Houk, A. (2020). Mixing of Subtropical, Central, and Intermediate Waters Driven by Shifting and Pulsing of the Agulhas Current. *Journal of Physical Oceanography*, 50(12), 3545–3560. <https://doi.org/10.1175/JPO-D-20-0093.1>
- Hahn, A., Miller, C., Andó, S., Bouimetarhan, I., Cawthra, H. C., Garzanti, E., Green, A. N., Radeff, G., Schefuß, E., & Zabel, M. (2018). The Provenance of Terrigenous Components in Marine Sediments Along the East Coast of Southern Africa. *Geochemistry, Geophysics, Geosystems*, 19(7), 1946–1962. <https://doi.org/10.1029/2017GC007228>
- Hall, I. R., Hemming, S. R., LeVay, L. J., Barker, S., Berke, M. A., Brentegani, L., Caley, T., Cartagena-Sierra, A., Charles, C. D., Coenen, J. J., Crespin, J. G., Franzese, A. M., Gruetzner, J., Han, X., Hines, S. K. V., Jimenez-Espejo, F. J., Just, J., Koutsodendris, A., Kubota, K., ... Zhang, H. (2017a). Site U1474. *Proceedings of the International Ocean Discovery Program, Expedition Reports*, 361, 37pp. <https://doi.org/10.14379/iodp.proc.361.103.2017>

- Hall, I. R., Hemming, S. R., LeVay, L. J., Barker, S., Berke, M. A., Brentegani, L., Caley, T., Cartagena-Sierra, A., Charles, C. D., Coenen, J. J., Crespin, J. G., Franzese, A. M., Gruetzner, J., Han, X., Hines, S. K. V., Jimenez-Espejo, F. J., Just, J., Koutsodendris, A., Kubota, K., ... Zhang, H. (2017b). Site U1479. *Proceedings of the International Ocean Discovery Program, Expedition Reports, 361*, 30pp.
<https://doi.org/10.14379/iodp.proc.361.108.2017>
- Hall, I. R., Hemming, S. R., LeVay, L. J., Barker, S., Berke, M. A., Brentegani, L., Caley, T., Cartagena-Sierra, A., Charles, C. D., Coenen, J. J., Crespin, J. G., Franzese, A. M., Gruetzner, J., Han, X., Koutsodendris, A., Kubota, K., Lathika, N., Richard D Norris, Pereira dos Santos, T., ... Zhang, H. (2017c). Expedition 361 summary. *Proceedings of the International Ocean Discovery Program, Expedition Reports, 361*, 33pp.
<https://doi.org/10.14379/iodp.proc.361.101.2017>
- Hammer, O., Harper, D., & Ryan, P. (2001). PAST: Paleontological Statistics Software Package for Education and Data Analysis. *Palaeontologia Electronica, 4*, 1–9.
- Hood, R. R., Beckley, L. E., & Wiggert, J. D. (2017). Biogeochemical and ecological impacts of boundary currents in the Indian Ocean. *Progress in Oceanography, 156*, 290–325.
<https://doi.org/10.1016/j.pocean.2017.04.011>
- Hutchings, L., van der Lingen, C. D., Shannon, L. J., Crawford, R. J. M., Verheyen, H. M. S., Bartholomae, C. H., van der Plas, A. K., Louw, D., Kreiner, A., Ostrowski, M., Fidel, Q., Barlow, R. G., Lamont, T., Coetzee, J., Shillington, F., Veitch, J., Currie, J. C., & Monteiro, P. M. S. (2009). The Benguela Current: An ecosystem of four components. *Progress in Oceanography, 83*(1), 15–32. <https://doi.org/10.1016/j.pocean.2009.07.046>

Imbrie, J., Berger, A., Boyle, E. A., Clemens, S. C., Duffy, A., Howard, W. R., Kukla, G., Kutzbach, J., Martinson, D. G., McIntyre, A., Mix, A. C., Molfino, B., Morley, J. J., Peterson, L. C., Pisias, N. G., Prell, W. L., Raymo, M. E., Shackleton, N. J., & Toggweiler, J. R. (1993). On the structure and origin of major glaciation cycles 2. The 100,000-year cycle. *Paleoceanography*, 8(6), 699–735.

<https://doi.org/10.1029/93PA02751>

Jacobs, Z., Roberts, M., Jebri, F., Srokosz, M., Kelly, S., Sauer, W., Bruggeman, J., & Popova, E. (2022). Drivers of productivity on the Agulhas Bank and the importance for marine ecosystems. *Deep Sea Research Part II: Topical Studies in Oceanography*, 199, 105080.

<https://doi.org/10.1016/j.dsr2.2022.105080>

Jebri, F., Srokosz, M., Jacobs, Z. L., Nencioli, F., & Popova, E. (2022). Earth Observation and Machine Learning Reveal the Dynamics of Productive Upwelling Regimes on the Agulhas Bank. *Frontiers in Marine Science*, 9.

<https://www.frontiersin.org/articles/10.3389/fmars.2022.872515>

John, T., Schenk, V., Mezger, K., & Tembo, F. (2004). Timing and PT evolution of whiteschist metamorphism in the Lufilian Arc-Zambezi Belt Orogen (Zambia): Implications for the assembly of Gondwana. *Journal of Geology*, 112(1), Article 1.

<https://doi.org/10.1086/379693>

Kaboth-Bahr, S., Gosling, W. D., Vogelsang, R., Bahr, A., Scerri, E. M. L., Asrat, A., Cohen, A. S., Düsing, W., Foerster, V., Lamb, H. F., Maslin, M. A., Roberts, H. M., Schäbitz, F., & Trauth, M. H. (2021). Paleo-ENSO influence on African environments and early modern humans. *Proceedings of the National Academy of Sciences*, 118(23), e2018277118.

<https://doi.org/10.1073/pnas.2018277118>

- Krug, M., Tournadre, J., & Dufois, F. (2014). Interactions between the Agulhas Current and the eastern margin of the Agulhas Bank. *Continental Shelf Research*, 81, 67–79.
<https://doi.org/10.1016/j.csr.2014.02.020>
- Laskar, J., Robutel, P., Joutel, F., Gastineau, M., Correia, A. C. M., & Levrard, B. (2004). A long-term numerical solution for the insolation quantities of the Earth. *Astronomy & Astrophysics*, 428(1), Article 1. <https://doi.org/10.1051/0004-6361:20041335>
- Latimer, J. C., Filippelli, G. M., Hendy, I. L., Gleason, J. D., & Blum, J. D. (2006a). Glacial-interglacial terrigenous provenance in the southeastern Atlantic Ocean: The importance of deep-water sources and surface currents. *Geology*, 34(7), 545–548.
<https://doi.org/10.1130/G22252.1>
- Latimer, J. C., Filippelli, G. M., Hendy, I., & Newkirk, D. R. (2006b). Opal-associated particulate phosphorus: Implications for the marine P cycle. *Geochimica et Cosmochimica Acta*, 70(15), 3843–3854. <https://doi.org/10.1016/j.gca.2006.04.033>
- Lisiecki, L. E., & Raymo, M. E. (2005). A Pliocene-Pleistocene stack of 57 globally distributed benthic $\delta^{18}\text{O}$ records. *Paleoceanography*, 20(1). <https://doi.org/10.1029/2004PA001071>
- Lutjeharms, J. R. E. (2007). Three decades of research on the greater Agulhas Current. *Ocean Science*, 3(1), 129–147. <https://doi.org/10.5194/os-3-129-2007>
- Lutjeharms, J. R. E., Valentine, H. R., & Van Ballegooyen, R. C. (2000). The hydrography and water masses of the Natal Bight, South Africa. *Continental Shelf Research*, 20(14), 1907–1939. [https://doi.org/10.1016/S0278-4343\(00\)00053-4](https://doi.org/10.1016/S0278-4343(00)00053-4)
- MacDonald, K. (2013). *EVALUATION OF SELECTIVE IRON EXTRACTION TECHNIQUES TO QUANTIFY IRON-BOUND PHOSPHORUS IN SEDIMENTS*. UNIVERSITY OF HAWAI‘I AT MĀNOA.

- Marino, G., Zahn, R., Ziegler, M., Purcell, C., Knorr, G., Hall, I. R., Ziveri, P., & Elderfield, H. (2013). Agulhas salt-leakage oscillations during abrupt climate changes of the Late Pleistocene. *Paleoceanography*, 28(3), 599–606. <https://doi.org/10.1002/palo.20038>
- Meyer, A. A., Lutjeharms, J. R. E., & de Villiers, S. (2002). The nutrient characteristics of the Natal Bight, South Africa. *Journal of Marine Systems*, 35(1), 11–37. [https://doi.org/10.1016/S0924-7963\(02\)00043-X](https://doi.org/10.1016/S0924-7963(02)00043-X)
- Milliman, J. D., & Meade, R. H. (1983). World-Wide Delivery of River Sediment to the Oceans. *The Journal of Geology*, 91(1), 1–21. <https://doi.org/10.1086/628741>
- Mortlock, R. A., & Froelich, P. N. (1989). A simple method for the rapid determination of biogenic opal in pelagic marine sediments. *Deep Sea Research A*, 36, 1415–1426. [https://doi.org/10.1016/0198-0149\(89\)90092-7](https://doi.org/10.1016/0198-0149(89)90092-7)
- Nesse, W. D. (2017). *Introduction to Mineralogy*. Oxford University Press.
- OriginPro* (10.1.0.178 (Student Version)). (2024). [Computer software]. OriginLab Corporation.
- Paytan, A., & McLaughlin, K. (2007). The Oceanic Phosphorus Cycle. *Chemical Reviews*, 107(2), 563–576. <https://doi.org/10.1021/cr0503613>
- Redfield, A. C. (1958). The Biological Control of Chemical Factors in the Environment. *American Scientist*, 46(3), 230A – 221.
- Ruttenberg, K. C. (1992). Development of a sequential extraction method for different forms of phosphorus in marine sediments. *Limnology and Oceanography*, 37(7), 1460–1482. <https://doi.org/10.4319/lo.1992.37.7.1460>
- Ruttenberg, K. C. (1993). Reassessment of the oceanic residence time of phosphorus. *Chemical Geology*, 107(3), 405–409. [https://doi.org/10.1016/0009-2541\(93\)90220-D](https://doi.org/10.1016/0009-2541(93)90220-D)

- Ruttenberg, K. C., & Berner, R. A. (1993). Authigenic apatite formation and burial in sediments from non-upwelling, continental margin environments. *Geochimica et Cosmochimica Acta*, 57(5), 991–1007. [https://doi.org/10.1016/0016-7037\(93\)90035-U](https://doi.org/10.1016/0016-7037(93)90035-U)
- Schubert, R., Gula, J., & Biastoch, A. (2021). Submesoscale flows impact Agulhas leakage in ocean simulations. *Communications Earth & Environment*, 2(1), 1–8. <https://doi.org/10.1038/s43247-021-00271-y>
- Schumann, E. H. (1982). Inshore circulation of the Agulhas current off Natal. *Journal of Marine Research*, 40(1), 43–55.
- Schüürman, J., Hahn, A., & Zabel, M. (2019). In search of sediment deposits from the Limpopo (Delagoa Bight, southern Africa): Deciphering the catchment provenance of coastal sediments. *Sedimentary Geology*, 380, 94–104. <https://doi.org/10.1016/j.sedgeo.2018.11.012>
- Scott, L., & Neumann, F. H. (2018). Pollen-interpreted palaeoenvironments associated with the Middle and Late Pleistocene peopling of Southern Africa. *Quaternary International*, 495, 169–184. <https://doi.org/10.1016/j.quaint.2018.02.036>
- servén, daniel, Brummitt, C., Abedi, H., & hlink. (2018). *dswah/pyGAM: V0.8.0* (v0.8.0) [Computer software]. Zenodo. <https://doi.org/10.5281/zenodo.1476122>
- Simon, M. H., Arthur, K. L., Hall, I. R., Peeters, F. J. C., Loveday, B. R., Barker, S., Ziegler, M., & Zahn, R. (2013). Millennial-scale Agulhas Current variability and its implications for salt-leakage through the Indian–Atlantic Ocean Gateway. *Earth and Planetary Science Letters*, 383, 101–112. <https://doi.org/10.1016/j.epsl.2013.09.035>
- Simpson, G. L. (2018). Modelling Palaeoecological Time Series Using Generalised Additive Models. *Frontiers in Ecology and Evolution*, 6. <https://doi.org/10.3389/fevo.2018.00149>

- Strickland, J. D. H., & Parsons, T. R. (1972). *A Practical Handbook of Seawater Analysis, 2nd edition.* <https://doi.org/10.25607/OBP-1791>
- Tangunan, D., Berke, M. A., Cartagena-Sierra, A., Flores, J. A., Gruetzner, J., Jiménez-Espejo, F., LeVay, L. J., Baumann, K.-H., Romero, O., Saavedra-Pellitero, M., Coenen, J. J., Starr, A., Hemming, S. R., & Hall, I. R. (2021). Strong glacial-interglacial variability in upper ocean hydrodynamics, biogeochemistry, and productivity in the southern Indian Ocean. *Communications Earth & Environment*, 2(1), Article 1. <https://doi.org/10.1038/s43247-021-00148-0>
- Turney, C. S. M., & Jones, R. T. (2010). Does the Agulhas Current amplify global temperatures during super-interglacials? *Journal of Quaternary Science*, 25(6), 839–843. <https://doi.org/10.1002/jqs.1423>
- Tyrrell, T. (1999). The relative influences of nitrogen and phosphorus on oceanic primary production. *Nature*, 400(6744), Article 6744. <https://doi.org/10.1038/22941>
- van Leeuwen, P. J., de Ruijter, W. P. M., & Lutjeharms, J. R. E. (2000). Natal pulses and the formation of Agulhas rings. *Journal of Geophysical Research: Oceans*, 105(C3), 6425–6436. <https://doi.org/10.1029/1999JC900196>
- Vinayachandran, P. N. M., Masumoto, Y., Roberts, M. J., Huggett, J. A., Halo, I., Chatterjee, A., Amol, P., Gupta, G. V. M., Singh, A., Mukherjee, A., Prakash, S., Beckley, L. E., Raes, E. J., & Hood, R. (2021). Reviews and syntheses: Physical and biogeochemical processes associated with upwelling in the Indian Ocean. *Biogeosciences*, 18(22), 5967–6029. <https://doi.org/10.5194/bg-18-5967-2021>

Wells, C., Pringle, J., & Stretch, D. D. (2024). Upwelling along the southeast African coastline and links to cold water temperature anomalies at Sodwana Bay, South Africa.

Continental Shelf Research, 276, 105227. <https://doi.org/10.1016/j.csr.2024.105227>

DATA APPENDICES

Appendix A – U1474 XRF and PtOT data, full record

Label Identifier	Sample No.	Age (kya)	Zr (ppm)	Fe (ppm)	Ti (ppm)	Ca (ppm)	Total P (ppm)	K (ppm)
1474 F1H1W 2-3	1	0.541	147	24651	2375	179868	506	10516
1474 F1H1W 7-8	2	1.892	166	21174	1958	193517	463	10296
1474 F1H1W 12-13	3	3.243	147	21564	2133	190968	473	10315
1474 F1H1W 17-18	4	4.595	141	22773	2220	176539	485	10600
1474 F1H1W 22-23	5	5.946	170	23207	2409	177828	464	10549
1474 F1H1W 28-29	6	7.568	144	24326	2504	166721	469	11109
1474 F1H1W 32-33	7	8.649	148	24705	2378	166908	482	11272
1474 F1H1W 37-38	8	10.000	174	24920	2477	169867	432	10762
1474 F1H1W 42-43	9	11.351	169	25666	2420	173722	428	11454
1474 F1H1W 47-48	10	12.703	149	22597	2379	179171	410	11200
1474 F1H1W 51-52	11	13.784	169	26077	2651	157009	431	11300
1474 F1H1W 57-58	12	15.405	170	31182	2612	153766	435	12061
1474 F1H1W 62-63	13	16.757	203	36277	2831	135000	436	13117
1474 F1H1W 67-68	14	18.108	197	27312	2812	143914	395	13180
1474 F1H1W 72-73	15	19.459	183	26276	2992	149814	390	13972
1474 F1H1W 77-78	16	20.811	171	24872	2905	144639	409	13424
1474 F1H1W 82-83	17	22.162	180	26913	3084	133467	421	13820
1474 F1H1W 87-88	18	23.514	181	24197	2763	155586	407	13476
1474 F1H1W 92-93	19	24.865	161	24187	2470	173518	397	12556
1474 F1H1W 97-98	20	26.216	190	24877	2571	169738	409	12527
1474 F1H1W 104-105	21	28.108	171	22608	2372	185271	431	12479
1474 F1H1W 107-108	22	28.919	171	21151	2202	186092	428	12045
1474 F1H1W 112-113	23	30.270	129	22066	2292	178829	449	12271
1474 F1H1W 117-118	24	31.622	157	21390	2097	187365	404	11687
1474 F1H1W 122-123	25	32.973	130	17755	1779	209565	351	9898
1474 F1H1W 128-129	26	34.595	141	24443	2466	169730	416	12649
1474 F1H1W 132-133	27	35.676	176	26874	2501	167039	401	12384

1474 F1H1W 137-138	28	37.027	148	23773	2255	178032	402	12319
1474 F1H1W 142-143	29	38.378	156	22800	2463	176759	393	12149
1474 F1H1W 147-148	30	39.730	170	25557	2546	161882	429	12368
1474 F1H2W 4-5	31	41.622	158	30802	2656	143518	404	13605
1474 F1H2W 7-8	32	42.432	168	24386	2741	151377	417	13225
1474 F1H2W 13-14	33	44.054	165	25357	2509	164638	413	12362
1474 F1H2W 17-18	34	45.135	162	23033	2539	177372	416	12623
1474 F1H2W 22-23	35	46.486	177	22673	2447	177635	424	11960
1474 F1H2W 29-30	36	48.378	152	24180	2329	177047	427	12196
1474 F1H2W 32-33	37	49.189	149	23487	2260	182138	397	12395
1474 F1H2W 36-37	38	50.270	174	24046	2370	185326	385	12132
1474 F1H2W 42-43	39	51.892	180	22835	2434	175358	435	12709
1474 F1H2W 47-48	40	53.243	167	24269	2438	156982	430	12496
1474 F1H2W 52-53	41	54.595	172	27540	2602	155374	481	13322
1474 F1H2W 57-58	42	55.946	167	25490	2369	158235	408	13266
1474 F1H2W 64-65	43	57.838	204	28500	2790	134696	404	14267
1474 F1H2W 67-68	44	58.649	168	27345	2818	144554	410	13613
1474 F1H2W 72-73	45	60.000	173	23599	2472	163171	424	12983
1474 F1H2W 77-78	46	61.351	160	26844	2567	158181	438	13391
1474 F1H2W 82-83	47	62.703	150	27278	2787	158258	408	13153
1474 F1H2W 89-90	48	64.595	151	26389	2566	170015	417	12943
1474 D1H3W 12-13	49	84.324	152	23144	2699	156859	413	13018
1474 D1H3W 17-18	50	85.676	169	24703	2751	149646	433	14128
1474 D1H3W 22-23	51	87.027	145	24579	2405	169578	454	13391
1474 D1H3W 27-28	52	88.378	132	22404	2017	184540	462	11353
1474 D1H3W 32-33	53	89.730	165	18787	1938	201469	472	12050
1474 D1H3W 37-38	54	91.081	132	17382	1787	200363	494	11552
1474 D1H3W 42-43	55	92.432	185	21165	2174	189593	452	12181
1474 D1H3W 47-48	56	93.784	205	22434	2431	169932	409	12648
1474 D1H3W 52-53	57	95.135	205	24438	2433	163353	429	12355
1474 D1H3W 56-57	58	96.216	242	25430	2582	155337	435	12465
1474 D1H3W 62-63	59	97.838	202	26791	2807	148723	431	12905
1474 D1H3W 67-68	60	99.189	182	27570	2509	150451	464	12721
1474 D1H3W 72-73	61	100.541	172	29220	2415	155863	468	12952
1474 D1H3W 77-78	62	101.892	192	26307	2323	174893	480	12335
1474 D1H3W 81-82	63	102.973	154	24513	2173	170917	538	12302
1474 D1H3W 87-88	64	104.595	148	22493	2241	170944	518	12574
1474 D1H3W 92-93	65	105.946	189	26944	2551	146930	476	13499
1474 D1H3W 97-98	66	107.297	141	27328	2628	145211	490	14002
1474 D1H3W 102-103	67	108.649	159	29114	2725	137543	473	13877
1474 D1H3W 107-108	68	110.000	170	29368	2778	132575	461	13996

1474 D1H3W 112-113	69	111.351	210	28967	2884	137295	448	13298
1474 D1H3W 117-118	70	112.703	153	31715	2938	133726	453	13613
1474 D1H3W 122-123	71	114.054	168	29820	2719	152484	434	13081
1474 D1H3W 127-128	72	115.405	179	22618	2699	163492	382	11993
1474 D1H3W 132-133	73	116.757	188	24897	2731	150458	363	12792
1474 D1H3W 137-138	74	118.108	205	25405	2696	146981	343	12638
1474 D1H3W 142-143	75	119.459	221	28578	3015	132678	357	13846
1474 D1H3W 147-148	76	120.811	204	22135	2872	155006	350	13285
1474 D1H4W 2-3	77	122.162	193	22584	2476	156364	377	12478
1474 D1H4W 7-8	78	123.514	179	22820	2639	169293	379	12982
1474 D1H4W 12-13	79	124.865	179	24205	2409	176405	411	12686
1474 D1H4W 16-17	80	125.946	190	22310	2384	182615	395	12431
1474 D1H4W 22-23	81	127.568	179	20412	2361	190066	413	11696
1474 D1H4W 27-28	82	128.919	158	25326	2761	168100	435	13261
1474 D1H4W 32-33	83	130.270	154	22928	2417	178555	439	12500
1474 D1H4W 37-38	84	131.622	178	28124	2757	145903	376	13344
1474 D1H4W 43-44	85	133.243	178	25839	2494	163184	384	13052
1474 D1H4W 47-48	86	134.324	174	22451	2443	172278	399	12361
1474 D1H4W 52-53	87	135.676	192	28228	2780	139041	395	13576
1474 D1H4W 57-58	88	137.027	207	29793	3089	121977	372	14280
1474 D1H4W 62-63	89	138.378	196	33501	3473	102003	207	15140
1474 D1H4W 67-68	90	139.730	205	38093	3333	101236	363	15293
1474 D1H4W 71-72	91	141.081	187	27945	3175	120137	354	14652
1474 F2H2W 105-106	92	155.405	182	27895	2953	132401	359	14531
1474 F2H2W 110-111	93	156.757	167	22318	2558	170499	362	12874
1474 F2H2W 115-116	94	158.108	158	23785	2403	177478	411	13053
1474 F2H2W 120-121	95	159.459	119	22971	2240	179439	419	12398
1474 F2H2W 125-126	96	160.811	164	20954	2052	198477	439	12465
1474 F2H2W 130-131	97	162.162	143	21831	2138	184545	452	12983
1474 F2H2W 135-136	98	163.514	147	25036	2495	171033	431	13225
1474 F2H2W 140-141	99	164.865	155	27059	2526	162140	429	13323
1474 F2H2W 145-146	100	166.216	166	24202	2344	179997	429	13101
1474 F2H3W 2-3	101	168.108	184	26667	2464	165941	394	12922
1474 F2H3W 7-8	102	169.459	188	25026	2567	164700	384	13093
1474 F2H3W 12-13	103	170.811	172	27753	2512	158003	449	13648
1474 F2H3W 17-18	104	172.162	165	28273	2938	134925	399	14798

1474 F2H3W 22-23	105	173.514	170	34375	3234	108278	400	15494
1474 F2H3W 27-28	106	174.865	187	28561	3104	117089	384	14758
1474 F2H3W 31-32	107	175.946	159	27343	3169	128775	372	14785
1474 F2H3W 37-38	108	177.568	178	25671	2824	143598	399	13906
1474 F2H3W 42-43	109	178.919	178	29164	2937	135058	421	14688
1474 F2H3W 47-48	110	180.270	160	29533	2956	133950	424	14489
1474 F2H3W 52-53	111	181.622	154	28305	2810	144478	414	14256
1474 F2H3W 55-56	112	182.432	165	24168	2648	151576	434	13758
1474 F2H3W 62-63	113	184.324	176	22237	2043	189416	473	12613
1474 F2H3W 67-68	114	185.676	163	21134	2185	190760	512	13055
1474 F2H3W 72-73	115	187.027	166	20318	2256	180696	516	12920
1474 F2H3W 77-78	116	188.378	144	22961	2299	174673	492	13403
1474 F2H3W 82-83	117	189.730	217	23249	2609	163552	431	13091
1474 F2H3W 87-88	118	191.081	158	25952	2620	156290	445	12552
1474 F2H3W 92-93	119	192.432	164	29410	2548	155276	419	12482
1474 F2H3W 97-98	120	193.784	189	29775	2639	148524	408	13349
1474 F2H3W 102-103	121	195.135	176	29545	2671	142697	439	13577
1474 F2H3W 107-108	122	196.486	173	37726	2991	128194	392	14651
1474 F2H3W 112-113	123	197.838	153	31922	2857	134093	406	14043
1474 F2H3W 117-118	124	199.189	141	32042	2946	133726	411	14648
1474 F2H3W 122-123	125	200.541	164	29621	2676	144634	441	14095
1474 F2H3W 128-129	126	202.162	134	29968	2657	146562	468	14224
1474 F2H3W 132-133	127	203.243	144	25187	2326	165131	490	13826
1474 F2H3W 137-138	128	204.595	131	25104	2307	171290	503	13334
1474 F2H3W 141-142	129	205.676	111	21225	2010	189508	525	12330
1474 F2H3W 147-148	130	207.297	146	18451	1887	200014	527	12100
1474 F2H4W 2-3	131	208.649	112	20322	1608	217454	563	11090
1474 F2H4W 22-23	132	214.054	130	25671	2088	174173	406	13156
1474 F2H4W 42-43	133	219.459	165	27790	2538	137449	349	14045
1474 F2H4W 62-63	134	224.865	168	24446	2478	157436	406	13248
1474 F2H4W 82-83	135	230.270	157	26162	2612	143187	467	14047
1474 F2H4W 101-102	136	235.405	124	24847	2075	186044	421	11854
1474 F2H4W 122-123	137	241.081	197	25995	2455	148179	391	13173
1474 F2H4W 142-143	138	246.486	192	24595	2687	146436	359	13622
1474 F2H5W 12-13	139	251.892	136	21984	1955	163905	336	11510
1474 F2H5W 32-33	140	257.297	170	22332	2324	168006	332	12719
1474 F2H5W 52-53	141	262.703	154	19234	1746	215547	404	11545
1474 F2H5W 72-73	142	268.108	164	25993	2325	153701	364	13520

1474 F2H5W 92-93	143	273.514	156	22188	2389	158921	368	13349
1474 F2H5W 112-113	144	278.919	150	22387	2118	171456	362	12439
1474 F2H5W 132-133	145	284.324	113	20210	1897	214284	399	11930
1474 F2H6W 2-3	146	289.730	92	15324	1454	260335	503	10064
1474 F2H6W 22-23	147	295.135	103	20637	1499	239162	382	10640
1474 F2H6W 42-43	148	300.541	114	28618	1803	194315	351	11803
1474 F2H6W 62-63	149	305.946	125	25077	2098	174038	290	12539
1474 F2H6W 82-83	150	311.351	149	21038	2083	197030	353	12223
1474 F2H6W 102-103	151	316.757	114	15978	1467	241007	472	10594
1474 D3H1W 112-113	152	341.081	130	24692	2030	187895	369	11912
1474 D3H1W 132-133	153	346.486	125	25532	1976	190709	414	12695
1474 D3H2W 2-3	154	351.892	131	20191	1660	218515	548	11426
1474 D3H2W 21-22	155	357.297	146	30193	2647	131711	376	14753
1474 D3H2W 62-63	156	368.108	120	23470	1976	201017	397	11753
1474 D3H2W 82-83	157	373.514	168	25257	2552	157245	360	13570
1474 D3H2W 121-122	158	384.054	123	19759	1612	224837	383	11990
1474 D3H2W 142-143	159	389.730	110	19869	1681	232288	420	11254
1474 D3H3W 12-13	160	395.135	116	20342	1752	215381	353	12247
1474 D3H3W 32-33	161	400.541	119	19965	1751	212551	375	12353
1474 D3H3W 52-53	162	405.946	116	26399	1692	215754	377	11733
1474 D3H3W 72-73	163	411.351	138	22307	1828	203272	369	11786
1474 D3H3W 92-93	164	416.757	119	23020	1743	210870	353	11757
1474 D3H3W 112-113	165	422.162	119	22918	1701	212269	399	11569
1474 D3H3W 132-133	166	427.568	117	24277	2014	188622	339	12454
1474 D3H4W 2-3	167	432.973	134	21113	1954	202168	359	12095
1474 D3H4W 22-23	168	438.378	114	20535	1801	212804	421	12333
1474 D3H4W 41-42	169	443.514	113	20035	1610	234606	436	11862
1474 D3H4W 62-63	170	449.189	143	24366	2395	169553	412	13741
1474 D3H4W 82-83	171	454.595	129	22111	1724	201722	510	12671
1474 D3H4W 122-123	172	465.405	107	19627	1573	223940	548	11688
1474 D3H4W 142-143	173	470.811	116	19236	1419	234790	557	10673
1474 D3H5W 12-13	174	476.216	105	21593	1632	205364	417	11657
1474 D3H5W 32-33	175	481.622	115	17798	1434	229266	476	10904
1474 D3H5W 52-53	176	487.027	138	20886	1744	213496	465	12471
1474 D3H5W 72-73	177	492.432	106	17976	1356	246788	522	10023
1474 A3H3W 122-123	178	516.757	105	20053	1243	241949	462	10288
1474 A3H3W 142-143	179	522.162	141	20610	1531	222001	406	11333
1474 A3H4W 12-13	180	527.568	130	18582	1612	228778	390	11402

1474 A3H4W 32-33	181	532.973	103	18571	1500	236404	427	11043
1474 A3H4W 52-53	182	538.378	94	18541	1315	238399	440	10959
1474 A3H4W 72-73	183	543.784	104	15618	1117	266970	412	9685
1474 A3H4W 92-93	184	549.189	127	21268	1620	217094	358	11310
1474 A3H4W 112-113	185	554.595	100	20772	1658	216519	358	10993
1474 A3H4W 130-131	186	559.459	134	24142	1799	190304	345	12755
1474 D4H1W 82-83	198	562.703	138	23632	1953	197474	408	12597
1474 A3H5W 3-4	187	565.676	97	22821	1545	212286	360	12138
1474 D4H1W 102-103	199	568.108	167	30056	2301	164910	365	13436
1474 A3H5W 22-23	188	570.811	127	19944	1865	194057	343	12338
1474 D4H1W 122-123	200	573.514	145	27626	2290	163771	388	13126
1474 A3H5W 42-43	189	576.216	119	25274	1867	201288	338	12819
1474 D4H1W 143-144	201	579.189	154	22764	1691	212960	502	12164
1474 A3H5W 62-63	190	581.622	83	17622	1508	241742	392	11672
1474 A3H5W 82-83	191	587.027	109	20148	1624	223230	389	11281
1474 A3H5W 102-103	192	592.432	125	19669	1725	212467	369	12066
1474 A3H5W 120-121	193	597.838	114	28277	2190	158020	377	13624
1474 A3H5W 142-143	194	603.243	131	26575	2378	164780	355	13754
1474 A3H6W 2-3	195	605.946	159	23006	2002	197888	374	12381
1474 D4H2W 101-102	207	608.378	153	26667	1964	188787	373	12804
1474 A3H6W 22-23	196	611.351	96	16867	1374	243844	445	10025
1474 A3H6W 42-43	197	616.757	111	20158	1515	223578	457	11488
1474 D4H2W 142-143	208	619.459	117	26318	2000	192321	509	13178
1474 D4H3W 2-3	209	622.162	126	28886	2099	175536	470	13555
1474 D4H3W 22-23	210	627.568	137	28045	2305	161790	429	14290
1474 D4H3W 42-43	211	632.973	133	21759	2077	187731	438	13032
1474 D4H3W 61-62	212	638.108	123	20625	1830	203281	478	12434
1474 D4H3W 82-83	213	643.784	139	20910	1780	221839	648	12251
1474 D4H3W 102-103	214	649.189	160	30174	2226	179556	424	13076
1474 D4H3W 122-123	215	654.595	133	29351	2038	171355	486	13362
1474 D4H3W 142-143	216	660.000	162	24315	2115	182616	489	13062
1474 D4H4W 2-3	217	662.703	137	21504	1789	195190	668	13065
1474 D4H4W 21-22	218	667.838	138	22320	1976	192672	517	13102
1474 D4H4W 42-43	219	673.514	128	21079	1753	209385	440	11913
1474 D4H4W 62-63	220	678.919	141	26201	2292	175000	365	12558
1474 D4H4W 82-83	221	684.324	148	30059	2513	151079	361	14293
1474 F4H3W 44-45	222	692.973	124	25056	2331	174591	405	13950
1474 F4H3W 64-65	223	698.378	119	16024	1680	231609	791	11289

1474 F4H3W 84-85	224	703.784	126	20463	2096	205585	482	12332
1474 F4H3W 104-105	225	709.189	130	24848	2344	167407	405	13550
1474 F4H3W 124-125	226	714.595	171	21582	2006	184743	506	12888
1474 F4H3W 144-145	227	720.000	180	22074	2197	186726	401	12749
1474 F4H4W 12-13	228	724.865	144	30531	2223	173957	376	13859
1474 F4H4W 32-33	229	730.270	140	21603	2237	184016	447	13204
1474 F4H4W 52-53	230	735.676	151	23415	2115	201600	421	12372
1474 F4H4W 72-73	231	741.081	141	19921	1860	193232	436	11592
1474 F4H4W 92-93	232	746.486	186	20547	2227	180104	385	12167
1474 F4H4W 112-113	233	751.892	166	26252	2803	131211	352	14576
1474 F4H4W 131-132	234	757.027	156	26224	2542	149134	330	14798
1474 F4H5W 2-3	235	762.703	169	28569	2727	130094	379	15272
1474 F4H5W 22-23	236	768.108	189	21353	2146	186711	397	13048
1474 F4H5W 42-43	237	773.649	205	26685	2799	138414	359	13613
1474 F4H5W 62-63	238	778.919	196	19015	2129	192982	380	11883
1474 F4H5W 82-83	239	784.324	183	17208	1903	202289	448	11527
1474 F4H5W 102-103	240	789.730	149	30259	2400	167513	369	13710
1474 F4H5W 122-123	241	795.135	134	20942	2325	181865	363	12613
1474 F4H5W 143-144	242	800.811	176	22028	2107	187325	430	12127
1474 F4H6W 12-13	243	805.946	138	24984	2313	166410	363	13736
1474 F4H6W 32-33	244	811.351	139	21658	2094	190987	367	12972
1474 F4H6W 52-53	245	816.757	155	16367	1743	218164	415	11049
1474 A4H4W 142-143	247	819.459	170	31836	2639	132016	327	11526
1474 F4H6W 72-73	246	822.162	181	22762	2223	184666	338	15424
1474 A4H5W 12-13	248	824.865	139	25011	2611	146256	346	14911
1474 A4H5W 32-33	249	830.270	155	25971	2172	161061	335	13217
1474 A4H5W 51-52	250	835.405	145	22063	2330	174078	362	13379
1474 A4H5W 72-73	251	841.081	171	20933	2018	189916	392	12429
1474 A4H5W 92-93	252	846.486	230	16928	1738	217429	429	10966
1474 A4H5W 112-113	253	851.892	137	16310	1655	219442	423	10384
1474 A4H5W 132-133	254	857.297	148	21142	1749	212603	408	11101
1474 A4H6W 2-3	255	862.703	126	41846	2053	155861	338	12822
1474 A4H6W 22-23	256	868.108	159	21062	2232	168069	346	14123
1474 A4H6W 42-43	257	873.514	160	23736	2382	159064	345	14693
1474 A4H6W 62-63	258	878.919	138	20514	2107	182167	387	13351
1474 F5H1W 82-83	261	878.919	133	17149	1749	215364	413	11397
1474 A4H6W 82-83	259	884.324	119	19144	1807	220153	436	12068
1474 F5H1W 102-103	262	884.324	119	22467	1788	209807	427	11704

1474 A4H6W 102-103	260	889.730	126	22354	1620	216800	408	11545
1474 F5H1W 123-124	263	890.000	124	17824	1801	219535	395	11413
1474 F5H1W 142-143	264	895.135	131	20693	1997	191902	398	12320
1474 F5H2W 12-13	265	900.541	137	17515	1881	226710	597	11567
1474 F5H2W 32-33	266	905.946	210	21996	2207	183128	385	12337
1474 F5H2W 52-53	267	911.351	187	18147	2031	201601	452	11642
1474 F5H2W 72-73	268	916.757	216	23259	2511	166748	380	12473
1474 F5H2W 92-93	269	922.162	164	23822	2404	161846	328	14207
1474 F5H2W 112-113	270	927.568	143	22852	2294	166366	374	13342
1474 F5H2W 132-133	271	932.973	351	19883	3883	109816	291	10698
1474 F5H3W 2-3	272	938.378	187	20236	2153	184816	454	11699
1474 F5H3W 22-23	273	943.784	153	25519	2392	163311	395	13307
1474 F5H3W 41-42	274	948.919	156	17097	1788	223999	388	11543
1474 F5H3W 62-63	275	954.595	173	18535	2029	195135	376	11589
1474 F5H3W 82-83	276	960.000	205	22026	2603	149356	356	13597
1474 F5H3W 102-103	277	965.405	172	26696	2988	114038	317	16613
1474 F5H3W 122-123	278	970.811	182	25493	2885	122441	317	16272
1474 F5H3W 142-143	279	976.216	188	23943	2770	140412	334	14968
1474 F5H4W 12-13	280	981.622	145	20395	2255	179977	338	12459
1474 F5H4W 32-33	281	987.027	126	23612	2351	163732	358	13614
1474 F5H4W 52-53	282	992.432	152	18578	1857	192351	419	13016
1474 F5H4W 72-73	283	997.838	133	23210	1982	195844	406	12398
1474 F5H4W 92-93	284	1003.243	136	24829	2187	169146	348	13642
1474 F5H4W 111-112	285	1008.378	123	26629	2224	155765	359	14678
1474 F5H4W 132-133	286	1014.054	157	20066	1992	182017	555	13409
1474 F5H5W 2-3	287	1019.459	177	25150	2535	149363	375	14992
1474 F5H5W 22-23	288	1024.865	170	24481	2262	167053	355	12431
1474 F5H5W 42-43	289	1030.270	116	25565	2096	175234	342	13464
1474 F5H5W 62-63	290	1035.676	133	26583	2557	149017	315	14495
1474 F5H5W 82-83	291	1041.081	151	25249	2533	159328	357	14147
1474 F5H5W 102-103	292	1046.486	162	17505	1720	222882	609	11486
1474 F5H5W 122-123	293	1051.892	133	21360	1942	190753	425	12266
1474 F5H5W 142-143	294	1057.297	281	11865	2345	188283	278	9003
1474 F5H6W 12-13	295	1062.703	146	19690	1922	200326	365	11522
1474 F5H6W 32-33	296	1068.108	145	24414	2135	170862	329	12921
1474 F5H6W 52-53	297	1073.514	138	25394	2222	167054	446	13963
1474 F5H6W 72-73	298	1078.919	124	20539	1823	192866	435	12009
1474 F5H6W 92-93	299	1084.324	122	18449	1876	202330	522	12492

1474 F5H6W 112-113	300	1089.730	124	18530	1578	223574	388	11438
1474 F5H6W 132-133	301	1095.135	116	20811	1845	203444	370	11986

Appendix B – U1479 XRF and PtOT data, full record

Label Identifier	Sample No.	Calculated Age (kyr)	Zr (ppm)	Fe (ppm)	Ti (ppm)	Ca (ppm)	PtOT (ppm)	K (ppm)
361-U1479I-1H-1-W 3/4-LATI	1	0.784	46	14820	936	250869	623	11511
361-U1479I-1H-1-W 8/9-LATI	2	1.995	46	17919	1009	212807	655	11397
361-U1479I-1H-1-W 13/14-LATI	3	3.205	55	14310	980	231288	692	11579
361-U1479I-1H-1-W 18/19-LATI	4	4.416	50	13719	891	264975	579	11555
361-U1479I-1H-1-W 23/24-LATI	5	5.627	41	21254	768	264869	554	10982
361-U1479I-1H-1-W 28/29-LATI	6	6.838	48	11694	759	263731	565	10354
361-U1479I-1H-1-W 33/34-LATI	7	8.023	35	15565	729	289757	565	10399
361-U1479I-1H-1-W 38/39-LATI	8	9.237	47	11527	704	277583	558	10909
361-U1479I-1H-1-W 43/44-LATI	9	10.381	52	11237	731	274487	570	10451
361-U1479I-1H-1-W 48/49-LATI	10	11.385	43	10050	762	274621	514	10084
361-U1479I-1H-1-W 53/54-LATI	11	12.272	39	9750	667	282305	613	9863
361-U1479I-1H-1-W 58/59-LATI	12	13.078	44	14984	718	293038	527	10172
361-U1479I-1H-1-W 63/64-LATI	13	13.825	51	13671	607	306498	659	8538
361-U1479I-1H-1-W 68/69-LATI	14	14.534	46	8808	700	318346	607	8686
361-U1479I-1H-1-W 73/74-LATI	15	15.220	69	10378	679	303828	572	8721
361-U1479I-1H-1-W 78/79-LATI	16	15.898	69	12666	659	291724	617	8307
361-U1479I-1H-1-W 83/84-LATI	17	16.576	60	12484	673	291149	642	8496
361-U1479I-1H-1-W 88/89-LATI	18	17.266	57	7320	725	304544	623	7775
361-U1479I-1H-1-W 93/94-LATI	19	17.973	71	7733	693	306465	662	8768
361-U1479I-1H-1-W 98/99-LATI	20	18.690	73	5585	616	319067	606	6824
361-U1479I-1H-1-W 103/104-LATI	21	19.451	91	5734	624	320383	620	7046
361-U1479I-1H-1-W 108/109-LATI	22	20.246	90	6054	604	316418	623	6983
361-U1479I-1H-1-W 113/114-LATI	23	21.080	91	6031	774	322299	628	7335
361-U1479I-1H-1-W 118/119-LATI	24	21.960	97	7155	867	308703	634	8106
361-U1479I-1H-1-W 123/124-LATI	25	22.874	93	10352	643	306157	659	7957
361-U1479I-1H-1-W 128/129-LATI	26	23.899	71	7046	768	322699	567	7521

361-U1479I-1H-1-W 133/134-LATI	27	25.149	73	6612	549	326958	529	7470
361-U1479I-1H-1-W 138/139-LATI	28	26.619	71	5751	552	316339	500	6249
361-U1479I-1H-1-W 143/144-LATI	29	28.253	56	7007	533	339832	477	6752
361-U1479I-1H-1-W 148/149-LATI	30	30.009	57	6317	542	340679	491	6586
361-U1479I-1H-2-W 3/4- LATI	31	31.850	53	5905	503	316803	472	6211
361-U1479I-1H-2-W 8/9- LATI	32	33.742	59	6103	555	331086	482	6862
361-U1479I-1H-2-W 13/14-LATI	33	35.656	58	6091	454	317726	449	6137
361-U1479I-1H-2-W 18/19-LATI	34	37.565	44	5986	544	313771	452	6547
361-U1479I-1H-2-W 23/24-LATI	35	39.447	53	9166	514	322327	447	6726
361-U1479I-1H-2-W 28/29-LATI	36	41.281	40	6293	478	320672	417	6172
361-U1479I-1H-2-W 33/34-LATI	37	43.012	51	5781	604	344599	405	6878
361-U1479I-1H-2-W 38/39-LATI	38	44.698	47	6606	542	317613	443	6767
361-U1479I-1H-2-W 43/44-LATI	39	46.285	45	6466	569	318719	445	7027
361-U1479I-1H-2-W 48/49-LATI	40	47.762	59	6478	567	313835	462	7242
361-U1479I-1H-2-W 53/54-LATI	41	49.113	44	6280	652	323680	451	7279
361-U1479I-1H-2-W 58/59-LATI	42	50.353	44	6308	459	319459	476	7010
361-U1479I-1H-2-W 63/64-LATI	43	51.559	44	6184	524	314771	480	6668
361-U1479I-1H-2-W 68/69-LATI	44	52.771	41	6358	595	322793	481	6956
361-U1479I-1H-2-W 73/74-LATI	45	53.982	63	7038	584	314888	507	7047
361-U1479I-1H-2-W 78/79-LATI	46	55.192	54	6279	523	329343	488	7046
361-U1479I-1H-2-W 83/84-LATI	47	56.403	56	6126	595	327342	484	6982
361-U1479I-1H-2-W 88/89-LATI	48	57.614	47	6901	587	306593	510	7303
361-U1479I-1H-2-W 93/94-LATI	49	58.824	67	9897	735	293010	607	8664
361-U1479I-1H-2-W 98/99-LATI	50	60.011	60	7579	675	271881	574	8315
361-U1479I-1H-2-W 103/104-LATI	51	61.222	94	13334	814	282676	564	9472
361-U1479I-1H-2-W 108/109-LATI	52	62.432	84	7754	810	300700	628	8931
361-U1479I-1H-2-W 113/114-LATI	53	63.643	66	8728	820	300808	649	9180
361-U1479I-1H-2-W 118/119-LATI	54	64.854	72	7867	816	296681	624	9129
361-U1479I-1H-2-W 123/124-LATI	55	66.064	60	8017	723	298605	615	9210
361-U1479I-1H-2-W 128/129-LATI	56	67.275	52	15437	713	287287	536	8691
361-U1479I-1H-2-W 133/134-LATI	57	68.486	81	9049	744	295769	628	9335
361-U1479I-1H-2-W 138/139-LATI	58	69.696	68	8282	676	310415	525	9447
361-U1479I-1H-2-W 143/144-LATI	59	70.907	42	8119	662	315544	496	9554
361-U1479I-1H-2-W 148/149-LATI	60	72.118	50	8688	681	292008	513	9092

361-U1479I-1H-3-W 3/4-LATI	61	73.304	54	9960	805	286551	579	10169
361-U1479I-1H-3-W 8/9-LATI	62	74.514	53	17473	675	291885	536	9889
361-U1479G-1H-3-W 9/10-LATI	63	74.878	35	8254	589	319770	508	9178
361-U1479I-1H-3-W 13/14-LATI	64	75.726	53	10343	628	308274	512	10083
361-U1479G-1H-3-W 14/15-LATI	65	76.089	42	9162	549	305233	522	9298
361-U1479I-1H-3-W 18/19-LATI	66	76.936	58	10309	609	292987	554	9647
361-U1479G-1H-3-W 19/20-LATI	67	77.299	47	9161	572	300355	604	9720
361-U1479I-1H-3-W 23/24-LATI	68	78.149	51	9680	642	301876	523	9509
361-U1479G-1H-3-W 24/25-LATI	69	78.512	40	9456	639	304196	583	10789
361-U1479G-1H-3-W 29/30-LATI	70	79.691	40	9998	641	288851	548	10293
361-U1479G-1H-3-W 34/35-LATI	71	80.819	52	11257	760	291469	554	11240
361-U1479G-1H-3-W 39/40-LATI	72	81.944	49	10332	687	301868	556	10110
361-U1479G-1H-3-W 44/45-LATI	73	83.069	62	11524	687	294425	548	9853
361-U1479G-1H-3-W 49/50-LATI	74	84.194	55	10413	841	293292	530	11273
361-U1479G-1H-3-W 54/55-LATI	75	85.319	66	11659	827	266799	545	11543
361-U1479G-1H-3-W 59/60-LATI	76	86.444	55	13088	880	272480	528	11704
361-U1479G-1H-3-W 64/65-LATI	77	87.569	61	12772	917	270864	565	12727
361-U1479G-1H-3-W 74/75-LATI	78	89.819	59	13264	895	255928	567	11487
361-U1479G-1H-3-W 79/80-LATI	79	90.944	56	14737	989	263518	552	12622
361-U1479G-1H-3-W 84/85-LATI	80	92.069	58	12273	994	256775	533	13025
361-U1479G-1H-3-W 89/90-LATI	81	93.194	50	11910	830	271625	545	12190
361-U1479G-1H-3-W 94/95-LATI	82	94.319	55	13118	919	264094	601	12437
361-U1479G-1H-3-W 99/100-LATI	83	95.444	52	13753	943	275433	504	11981
361-U1479G-1H-3-W 109/110-LATI	84	97.694	49	11042	796	287320	514	11743
361-U1479G-1H-3-W 114/115-LATI	85	98.820	65	10140	755	288493	483	10683
361-U1479G-1H-3-W 119/120-LATI	86	99.941	53	10775	694	293997	515	9955
361-U1479G-1H-3-W 124/125-LATI	87	101.068	44	8429	710	306515	531	10184
361-U1479G-1H-3-W 129/130-LATI	88	102.192	49	18092	559	309756	537	10614
361-U1479G-1H-3-W 134/135-LATI	89	103.318	48	8667	577	282384	504	8837
361-U1479G-1H-3-W 139/140-LATI	90	104.442	50	20936	764	285398	562	11413
361-U1479G-1H-3-W 144/145-LATI	91	105.568	51	11331	773	289434	546	11870
361-U1479G-1H-3-W 149/150-LATI	92	106.692	56	11663	742	290901	580	10982
361-U1479G-1H-4-W 7/8-LATI	93	108.495	55	9806	678	279635	530	9489
361-U1479G-1H-4-W 12/13-LATI	94	109.615	56	10505	702	303634	537	10040

361-U1479G-1H-4-W 17/18-LATI	95	110.745	48	9457	742	300204	541	10677
361-U1479G-1H-4-W 22/23-LATI	96	111.864	45	9801	740	301390	566	10693
361-U1479G-1H-4-W 27/28-LATI	97	112.990	40	9568	633	283990	610	9440
361-U1479G-1H-4-W 32/33-LATI	98	114.120	48	9459	623	289284	559	10568
361-U1479G-1H-4-W 37/38-LATI	99	115.240	41	10338	615	303082	607	10198
361-U1479G-1H-4-W 42/43-LATI	100	116.370	35	9271	571	312341	804	9692
361-U1479G-1H-4-W 47/48-LATI	101	117.490	41	9020	537	310788	629	9812
361-U1479G-1H-4-W 52/53-LATI	102	118.620	30	8416	586	314934	664	9684
361-U1479G-1H-4-W 57/58-LATI	103	119.740	32	8284	562	320379	640	10354
361-U1479G-1H-4-W 61/62-LATI	104	120.644	31	9309	535	305527	646	9896
361-U1479G-1H-4-W 67/68-LATI	105	121.990	40	10381	628	297329	708	10236
361-U1479G-1H-4-W 72/73-LATI	106	123.120	36	8239	583	318155	686	9744
361-U1479G-1H-4-W 77/78-LATI	107	124.240	50	9705	680	293776	646	10728
361-U1479G-1H-4-W 82/83-LATI	108	125.370	51	9150	631	283160	661	9915
361-U1479G-1H-4-W 87/88-LATI	109	126.490	47	10023	741	276637	658	10809
361-U1479C-2H-3-W 142/143-LATI	110	126.896	36	9354	494	359774	499	7635
361-U1479G-1H-4-W 92/93-LATI	111	127.620	71	9226	727	269631	775	9889
361-U1479G-1H-4-W 97/98-LATI	112	128.740	79	9236	837	264501	666	10184
361-U1479G-1H-4-W 102/103-LATI	113	129.870	71	10468	796	271021	729	10621
361-U1479G-1H-4-W 107/108-LATI	114	130.990	76	9689	717	271179	717	10291
361-U1479C-2H-4-W 12/13-LATI	115	131.351	37	7025	462	321632	579	8018
1479 G1H4W 112-113	116	132.120	64	9052	668	282791	664	9939
1479 G1H4W 117-118	117	133.240	78	8191	710	290539	666	9062
1479 G1H4W 122-123	118	134.370	93	8396	682	286899	674	9161
1479 G1H4W 127-128	119	135.490	86	6890	776	296284	719	8397
1479 C2H4W 32-33	120	135.829	38	7751	496	325617	534	8937
1479 G1H4W 132-133	121	136.620	90	6452	620	287156	745	7738
1479 G1H4W 137-138	122	137.740	146	6616	840	258499	948	8225
1479 G1H4W 142-143	123	138.870	226	5593	1145	260016	1253	7540
1479 G1H4W 147-148	124	139.990	167	6249	800	300176	878	7217
1479 C2H4W 52-53	125	140.283	17	16530	536	314588	496	9105
1479 G1H5W 2-3	126	141.120	64	6518	617	333869	493	7367
1479 G1H5W 7-8	127	142.240	64	6472	524	340614	506	6853
1479 G1H5W 12-13	128	143.370	59	6149	595	342505	496	7271
1479 G1H5W 17-18	129	144.490	81	6214	524	352514	484	7115
1479 C2H4W 72-73	130	144.761	33	6907	461	345277	463	9127
1479 G1H5W 22-23	131	145.620	60	6739	551	332838	484	7694
1479 G1H5W 27-28	132	146.740	67	6553	509	327081	473	7414

1479 G1H5W 32-33	133	147.870	68	7135	693	327613	481	7953
1479 G1H5W 37-38	134	148.990	57	7940	623	314003	524	7955
1479 C2H4W 92-93	135	149.215	30	13218	477	351973	449	8016
1479 G1H5W 42-43	136	150.120	59	8191	575	316271	522	7937
1479 G1H5W 47-48	137	151.240	71	6424	639	321865	520	7566
1479 G1H5W 52-53	138	152.370	60	6695	542	319788	505	7677
1479 G1H5W 57-58	139	153.600	72	7178	585	315985	541	7592
1479 C2H4W 112-113	140	153.830	18	6348	315	374142	426	6893
1479 G1H5W 62-63	141	154.890	58	7626	558	312004	648	7815
1479 G1H5W 67-68	142	156.180	81	7395	702	305443	671	8963
1479 G1H5W 72-73	143	157.470	70	8934	722	294148	510	8911
1479 H2H1W 117-118	144	158.271	75	8431	888	267236	549	10259
1479 G1H5W 77-78	145	158.760	81	7762	651	301747	600	8557
1479 C2H4W 132-133	146	158.940		15011	340	352866	588	7887
1479 H2H1W 121-122	147	159.272	68	9635	910	273566	487	10619
1479 G1H5W 82-83	148	160.040	52	7035	626	323077	450	8796
1479 H2H1W 127-128	149	160.787	79	14575	853	269678	436	10319
1479 G1H5W 87-88	150	161.330	53	7230	640	314575	561	7973
1479 H2H1W 132-133	151	162.052	87	18628	935	262675	450	11474
1479 G1H5W 92-93	152	162.620	54	7731	543	318455	559	7814
1479 H2H1W 137-138	153	163.318	91	11882	1055	255302	471	12296
1479 G1H5W 97-98	154	163.912	57	6404	642	325405	488	7903
1479 C2H5W 2-3	155	164.067	31	6711	430	360275	448	7957
1479 H2H1W 142-143	156	164.583	80	13841	969	261993	490	11653
1479 G1H5W 102-103	157	165.200	59	6546	614	331120	507	7638
1479 H2H1W 147-148	158	165.865	71	19437	1024	253694	521	12816
1479 G1H5W 107-108	159	166.480	52	7029	550	323683	496	7544
1479 H2H2W 2-3	160	167.124	76	14040	1101	246868	575	12399
1479 G1H5W 112-113	161	167.770	89	6682	601	324912	565	7975
1479 G1H5W 117-118	162	169.060	74	6348	740	314162	545	7970
1479 C2H5W 22-23	163	169.163	32	7654	547	320627	424	8903
1479 G1H5W 122-123	164	170.350	59	7186	667	312589	506	8300
1479 G1H5W 127-128	165	171.640	62	8349	767	296991	531	9191
1479 H2H2W 22-23	167	172.178	60	12119	919	251884	549	12864
1479 G1H5W 132-133	166	172.920	65	8400	700	294284	502	9175
1479 G1H5W 137-138	168	174.210	75	9449	861	276711	608	10423
1479 C2H5W 41-42	169	174.288	27	16322	542	324952	457	9636
1479 H2H2W 42-43	170	177.259	70	12199	962	260569	590	12584
1479 C2H5W 59-60	171	178.634	43	12234	499	314896	439	9743
1479 H2H2W 59-60	172	181.553	59	15792	853	260865	526	12568
1479 C2H5W 82-83	173	184.513	36	7536	510	346183	516	8374
1479 H2H2W 82-83	174	187.376	59	11620	825	274240	525	12448
1479 C2H5W 102-103	175	189.647	26	7741	421	335662	549	8198
1479 H2H2W 102-103	176	192.448	37	9472	668	299195	556	10348

1479 C2H5W 119-120	177	193.970	58	6938	487	333707	571	7596
1479 H2H2W 119-120	178	196.754	55	9327	494	328320	570	7912
1479 C2H5W 142-143	179	199.869	45	10692	463	334075	542	7862
1479 H2H2W 142-143	180	202.579	70	14057	795	284707	518	10603
1479 C2H6W 12-13	181	204.966	58	12023	531	320015	540	7725
1479 H2H3W 12-13	182	207.650	80	12120	950	274066	561	11172
1479 C2H6W 32-33	183	210.095	55	5897	541	344136	521	7142
1479 H2H3W 32-33	184	212.723	40	9010	587	311936	546	9263
1479 C2H6W 52-53	185	215.201	33	11239	456	356875	442	6201
1479 H2H3W 52-53	186	217.769	28	9550	600	319386	634	9429
1479 C2H6W 72-73	187	220.324	53	9665	485	325411	537	7054
1479 H2H3W 72-73	188	222.847	46	7106	552	337839	579	7297
1479 C2H6W 92-93	189	225.448	75	7004	644	323245	609	8117
1479 H2H3W 92-93	190	227.926	59	6668	542	323907	516	7629
1479 C2H7W 12-13	191	230.542	43	5433	489	344802	494	7750
1479 H2H3W 112-113	192	233.102	59	6977	575	328271	497	7659
1479 C2H7W 31-32	193	236.276	60	16686	514	331187	539	7975
1479 H2H3W 132-133	194	239.228	49	5302	494	353056	540	6416
1479 H2H4W 2-3	195	244.340	65	13518	650	291505	609	8556
1479 H2H4W 22-23	196	248.272	93	8032	804	277915	623	9461
1479 H2H4W 42-43	197	252.252	99	8730	715	281423	676	8879
1479 H2H4W 59-60	198	255.639	79	8057	680	296769	596	9000
1479 H2H4W 82-83	199	260.240	50	7286	575	322728	552	8612
1479 H2H4W 102-103	200	264.269	27	6633	456	344368	553	8016
1479 H2H4W 119-120	201	267.696	87	5395	353	375071	1088	6494
1479 C3H1W 72-73	202	268.042	54	8152	587	332085	519	9708
1479 C3H1W 92-93	203	272.128	91	7054	515	345341	503	8606
1479 H2H4W 142-143	204	272.354	57	4254	241	381610	591	5550
1479 H2H5W 7-8	205	275.420	31	10411	375	362897	515	6323
1479 C3H1W 113-114	206	276.217	80	7926	553	323864	523	9703
1479 C3H1W 132-133	207	280.375	59	6568	467	336560	519	8698
1479 C3H2W 2-3	208	284.596	71	7202	459	340253	532	8820
1479 C3H2W 19-20	209	288.252	52	7381	425	350211	528	8531
1479 C3H2W 23-24	210	288.911	76	9846	383	355471	550	8512
1479 C3H2W 42-43	211	293.285	89	6894	384	340377	549	8371
1479 C3H2W 65-66	212	296.620	74	7074	389	348483	504	8438
1479 C3H2W 82-83	213	298.138	32	14588	421	365541	497	7936
1479 C3H2W 102-103	214	300.205	59	5316	365	373863	546	6854
1479 C3H2W 142-143	215	306.139	62	4625	269	374676	540	5795
1479 C3H3W 12-13	216	308.917	60	5593	353	371397	605	6603
1479 C3H3W 32-33	217	311.677	65	14171	317	356877	605	6707
1479 C3H3W 53-54	218	314.459	75	5309	298	368987	487	5800
1479 C3H3W 72-73	219	317.241	27	8399	397	361975	576	6371
1479 C3H3W 92-93	220	320.024	70	5512	413	361369	502	6510

1479 C3H3W 112-113	221	322.792	43	5418	490	365257	473	6580
1479 C3H3W 132-133	222	325.572	59	11437	461	335593	449	5905
1479 C3H4W 2-3	223	328.350	36	4493	315	382423	425	5624
1479 C3H4W 22-23	224	331.128	59	3714	337	385172	395	4681
1479 C3H4W 42-43	225	333.896	26	4581	305	380966	396	5343
1479 C3H4W 59-60	226	336.258	37	5584	374	344808	416	6492
1479 C3H4W 82-83	227	339.460	58	4244	397	363894	415	6084
1479 C3H4W 102-103	228	342.228	55	9844	447	352559	428	6343
1479 H3H1W 97-98	229	343.600	45	5299	455	355075	415	7914
1479 C3H4W 119-120	230	344.599	70	5991	484	333846	420	7458
1479 H3H1W 117-118	231	346.368	58	6238	510	343575	422	7607
1479 C3H4W 142-143	232	347.826	80	17446	546	328598	420	7364
1479 H3H1W 137-138	233	349.295	55	5784	510	357457	517	8281
1479 C3H5W 12-13	234	350.865	40	6307	524	318651	498	8487
1479 H3H2W 7-8	235	352.319	33	6299	501	340944	515	8477
1479 C3H5W 32-33	236	353.889	28	7142	585	311879	489	9079
1479 H3H2W 24-25	237	354.888	53	6466	444	336644	505	8180
1479 C3H5W 52-53	238	356.929	46	8755	692	316329	458	10225
1479 H3H2W 44-45	239	357.903	75	6947	461	330878	606	8443
1479 C3H5W 72-73	240	359.953	59	9969	624	310589	468	9726
1479 H3H2W 64-65	241	360.927	43	6138	468	347417	531	8314
1479 C3H5W 92-93	242	362.983	59	8582	543	321889	434	9803
1479 C3H5W 112-113	243	366.023	60	11646	362	361835	428	7851
1479 C3H5W 132-133	244	369.044	49	9315	440	345791	490	7496
1479 C3H6W 2-3	245	372.083	65	9987	431	329887	442	9086
1479 C3H6W 22-23	246	375.123	93	8955	539	311838	531	9920
1479 C3H6W 42-43	247	378.148	99	9338	668	295926	571	10928
1479 C3H6W 59-60	248	380.745	79	7762	612	317624	543	9756
1479 C3H6W 82-83	249	384.215	50	12608	494	333017	565	9032
1479 C3H7W 2-3	250	387.415	27	12138	383	357768	561	6626
1479 C3H7W 22-23	251	390.439	45	5982	416	339047	583	6881
1479 C4H1W 128-129	252	423.229	46	9522	748	289921	523	10860
1479 C4H1W 148-149	253	426.250	61	10752	804	268308	646	10497
1479 C4H2W 18-19	254	429.287	59	11421	765	269711	592	12316
1479 C4H2W 38-39	255	432.308	44	9871	698	277530	579	11832
1479 C4H2W 58-59	256	435.345	49	7873	621	299812	709	9592
1479 C4H2W 78-79	257	438.366	64	13435	677	294469	655	10432
1479 C4H2W 98-99	258	441.400	71	9919	735	285465	698	11713
1479 C4H2W 118-119	259	444.422	56	19920	859	279792	541	12172
1479 C4H2W 138-139	260	447.464	82	15865	883	274236	622	11340
1479 C4H3W 8-9	261	450.330	70	10379	825	267388	616	12173
1479 C4H3W 28-29	262	453.188	71	11334	741	268751	593	12001
1479 C4H3W 47-48	263	455.889	74	8732	686	294156	761	9962
1479 C4H3W 68-69	264	458.886	99	8110	829	279080	771	9911

1479 C4H3W 88-89	265	461.724	113	7752	767	294293	700	9930
1479 C4H3W 108-109	266	464.572	116	7822	864	290160	696	9722
1479 C4H3W 128-129	267	467.425	89	7197	791	298976	593	9007
1479 C4H3W 148-149	268	470.269	78	6798	733	305256	519	8272
1479 C4H4W 18-19	269	473.120	86	5874	621	324153	545	7624
1479 C4H4W 38-39	270	475.967	72	7193	622	317365	579	8177
1479 C4H4W 58-59	271	478.818	90	8087	897	264675	627	9358
1479 C4H4W 78-79	272	481.666	96	8627	878	270363	626	9813
1479 H4H1W 73-74	273	483.976	19	7696	467	329162	580	8679
1479 C4H4W 98-99	274	484.518	95	9759	887	264577	706	10762
1479 H4H1W 93-94	275	486.868	37	7398	414	324133	527	8310
1479 C4H4W 118-119	276	487.365	62	10930	872	268911	637	12054
1479 H4H1W 113-114	277	489.735	30	5705	445	331090	519	7836
1479 C4H4W 138-139	278	490.216	88	11318	1098	245391	701	13037
1479 H4H1W 133-134	279	492.611	33	5746	415	331948	475	7647
1479 C4H5W 8-9	280	493.063	43	15945	756	277641	608	11067
1479 H4H2W 3-4	281	495.511	70	6395	625	318347	566	7544
1479 C4H5W 28-29	282	496.168	62	18649	628	293249	584	11171
1479 H4H2W 23-24	283	500.088	75	6304	733	312432	558	7858
1479 C4H5W 48-49	284	500.743	53	8476	726	289106	614	11166
1479 H4H2W 43-44	285	504.697	64	10258	764	278579	601	9140
1479 C4H5W 68-69	286	505.329	47	9130	694	288229	547	10499
1479 H4H2W 63-64	287	509.306	93	8785	901	266523	650	10189
1479 C4H5W 88-89	288	509.896	51	8455	562	330948	524	7477
1479 H4H2W 83-84	289	513.926	59	8103	729	306435	501	10670
1479 C4H5W 108-109	290	514.465	78	6827	595	312517	518	8155
1479 C4H5W 128-129	291	519.051	96	10644	704	311519	514	8050
1479 C4H5W 148-149	292	523.624	69	7647	702	273945	504	9906
1479 C4H6W 18-19	293	528.210	56	7141	591	304558	532	8580
1479 C4H6W 38-39	294	532.807	32	15645	583	304614	518	7955
1479 C4H6W 58-59	295	537.370	79	9620	846	284074	458	9454
1479 C4H6W 78-79	296	541.956	77	9215	846	273857	430	9777
1479 C4H6W 98-99	297	546.529	92	9618	977	239981	471	11244
1479 C4H6W 118-119	298	551.115	74	10725	973	242246	540	12286
1479 C4H6W 138-139	299	555.711	69	10669	892	258408	499	12681
1479 C4H7W 8-9	300	560.270	88	12337	977	244657	554	12906
1479 C5H2W 62-63	301	631.634	39	6454	503	314491	492	8446
1479 C5H2W 81-82	302	636.693	30	6642	481	308459	451	8142
1479 C5H2W 102-103	303	642.258	36	8084	500	292673	472	9727
1479 C5H2W 122-123	304	647.583	46	7791	671	292353	514	9738
1479 C5H2W 142-143	305	652.875	58	8349	680	280185	430	10623
1479 C5H3W 12-13	306	658.202	56	10242	793	262793	516	11577
1479 C5H3W 32-33	307	663.621	69	11444	875	245778	530	12240
1479 C5H3W 52-53	308	669.128	65	10525	794	270819	506	11719

1479 C5H3W 72-73	309	674.594	53	8850	664	273776	494	10788
1479 C5H3W 92-93	310	680.099	50	9510	729	276731	525	11324
1479 C5H3W 112-113	311	685.593	54	8696	659	280338	504	10865
1479 C5H3W 132-133	312	691.070	39	20722	716	286484	515	11279
1479 C5H4W 2-3	313	696.565	52	22302	624	294546	596	10016
1479 C5H4W 22-23	314	702.041	57	7398	602	303061	591	8383
1479 C5H4W 42-43	315	707.536	73	7161	589	280751	532	8551
1479 C5H4W 63-64	316	713.290	84	7374	635	285228	562	8488
1479 C5H4W 82-83	317	718.506	69	6799	535	320302	536	7556
1479 C5H4W 102-103	318	723.983	64	7919	640	320430	551	8148
1479 C5H4W 123-124	319	729.728	72	7519	623	306249	484	8060
1479 C5H4W 143-144	320	735.232	56	6934	694	311645	570	8016
1479 H5H1W 139-140	321	738.947	68	8975	752	268411	555	11119
1479 C5H5W 12-13	322	740.421	50	6343	465	332996	512	7394
1479 H5H2W 9-10	323	744.507	37	12271	538	296028	493	10120
1479 C5H5W 32-33	324	745.926	29	10897	480	302969	534	7093
1479 H5H2W 29-30	325	750.045	29	6618	414	328969	570	7807
1479 C5H5W 52-53	326	751.103	45	6078	501	303533	445	7578
1479 H5H2W 49-50	327	754.203	41	4919	283	341351	624	7548
1479 C5H5W 72-73	328	755.146	37	6999	467	306101	464	8437
1479 H5H2W 69-70	329	758.310	36	5689	348	331180	643	6965
1479 C5H5W 92-93	330	759.191	48	11157	521	310536	537	7670
1479 H5H2W 89-90	331	762.413	38	7013	381	336424	580	6241
1479 C5H5W 112-113	332	763.253	65	8077	778	284013	543	9386
1479 H5H2W 109-110	333	766.504	23	13462	556	330138	519	7325
1479 C5H5W 132-133	334	767.310	80	8376	875	277025	525	9438
1479 H3H2W 129-130	335	770.622	58	5113	630	332095	491	6745
1479 C5H6W 2-3	336	771.360	104	10922	1170	226815	623	12074
1479 H5H2W 149-150	337	774.723	52	6525	538	316667	415	7151
1479 C5H6W 23-24	338	775.610	82	11278	1098	226258	602	12408
1479 H5H3W 18-19	339	778.625	55	6652	644	300897	479	7787
1479 C5H6W 42-43	340	779.466	80	12521	1102	220779	578	12509
1479 H5H3W 38-39	341	782.729	67	7331	677	305063	473	8794
1479 C5H6W 63-64	342	783.711	94	10910	1172	221313	599	13197
1479 H5H3W 58-59	343	786.838	65	6614	645	297549	527	8640
1479 C5H6W 82-83	344	787.575	72	11902	1036	249202	569	12674
1479 H5H3W 78-79	345	790.932	39	6082	501	315601	547	8033
1479 C5H6W 102-103	346	791.627	64	20767	961	257813	499	14097
1479 C5H6W 122-123	347	795.668	61	11282	937	242751	555	13759
1479 C5H7W 12-13	348	801.779	62	15100	1068	228824	599	14671
1479 C6H1W 19-20	349	817.650	61	8606	736	279074	688	10571
1479 C6H1W 39-40	350	821.053	44	18764	713	274313	569	11851
1479 C6H1W 59-60	351	824.462	61	11361	861	256142	568	13080
1479 C6H1W 79-80	352	827.893	55	9691	728	273096	569	11765

1479 B5H4W 83-84	353	830.390	50	14819	801	260394	560	12842
1479 B5H4W 103-104	354	833.793	43	13489	691	278606	548	11457
1479 B5H4W 123-124	355	837.222	39	24682	651	292714	530	10577
1479 B5H4W 143-144	356	840.645	49	7092	539	321421	554	7492
1479 C6H2W 9-10	357	841.540	57	8038	759	278271	584	11225
1479 B5H5W 13-14	358	844.058	76	13025	795	270668	637	9634
1479 C6H2W 29-30	359	844.943	62	9192	884	257808	589	11764
1479 B5H5W 33-34	360	847.482	63	12963	738	277082	690	10773
1479 C6H2W 49-50	361	848.359	54	9853	652	275809	492	11384
1479 B5H5W 53-54	363	851.764	68	16664	869	252376	595	12028
1479 C6H2W 69-70	362	854.314	55	8788	644	293109	489	10682
1479 B5H5W 73-74	364	854.314	60	18412	880	252837	560	11646
361-U1479C-6H-2-W 89/90-LATI	365	855.191					461	
1479 B5H5W 93-94	366	857.741	51	9420	671	304199	592	9912
1479 C6H2W 109-110	367	858.595	28	5990	435	337028	501	8372
1479 C6H2W 149-150	369	862.007	53	6904	651	304660	799	8418
1479 C6H2W 129-130	368	865.415	34	7418	530	317523	486	8379
1479 C6H3W 19-20	370	868.841	41	6173	493	311088	504	8300
1479 C6H3W 39-40	371	872.252	45	8416	661	295458	547	10000
1479 C6H3W 59-60	372	875.725	44	9489	650	293884	540	10168
1479 C6H3W 79-80	373	879.319	40	8526	668	306952	533	10565
1479 C6H3W 99-100	374	882.881	53	7200	642	303743	532	9749
1479 C6H3W 119-120	375	886.451	39	7027	518	319959	458	9283
1479 C6H3W 139-140	376	890.038	31	6859	544	314922	510	9514
1479 C6H4W 9-10	377	893.607	26	13422	491	312108	517	9115
1479 C6H4W 29-30	378	897.176	43	7696	471	310824	499	8782
1479 C6H4W 49-50	379	900.745	35	14409	452	305617	533	7860
1479 C6H4W 69-70	380	904.313	73	14423	678	293205	601	7692
1479 C6H4W 89-90	381	907.900	86	13267	910	251806	569	10256
1479 C6H4W 109-110	382	911.468	66	8712	823	281852	460	10243
1479 C6H4W 129-130	383	915.028	59	6723	740	295367	498	9758
1479 C6H4W 149-150	384	918.598	58	11373	663	293085	476	9599
1479 C6H5W 19-20	385	922.185	72	8933	811	274485	525	11103
1479 C6H5W 39-40	386	925.754	73	10392	918	269760	582	12550
1479 C6H5W 59-60	387	929.324	70	13328	856	253163	610	12594
1479 C6H5W 79-80	388	932.913	72	14327	1080	228503	647	14536
1479 C6H5W 99-100	389	936.136	56	19903	950	246617	586	13325
1479 C6H5W 119-120	390	939.246	51	9957	794	271930	523	12907
1479 C6H5W 139-140	391	942.363	51	9399	793	278260	495	12112
1479 C6H6W 9-10	392	945.462	42	14349	641	295284	482	11295
1479 C6H6W 29-30	393	948.571	76	8923	715	276280	682	10831
1479 C6H6W 49-50	394	951.693	44	8486	639	281616	616	10472
1479 C6H6W 69-70	395	954.794	54	8637	745	278041	641	11153

1479 C6H6W 89-90	396	957.894	58	19034	721	267729	582	10936
1479 C6H6W 109-110	397	961.019	67	14867	632	293002	547	8997
1479 C6H6W 129-130	398	964.120	49	6657	598	301075	591	8248
1479 C6H6W 149-150	399	967.221	70	8329	748	279051	586	9436
1479 C7H2W 50-51	400	1007.559	51	9535	767	281473	516	12065
1479 C7H2W 70-71	401	1010.334	41	21379	682	292313	630	10858
1479 C7H2W 90-91	402	1013.081	47	8283	667	300221	618	10908
1479 C7H2W 110-111	403	1015.951	50	9196	763	276005	585	11081
1479 C7H2W 130-131	404	1018.699	52	7714	768	292986	585	10847
1479 I4H3W 31-32	405	1058.218	142	9383	1212	219619	785	11302
1479 I4H3W 51-52	406	1061.393	66	10121	905	255722	519	11074
1479 I4H3W 71-72	407	1064.689	62	14734	829	266436	449	12058
1479 I4H3W 91-92	408	1067.871	50	6995	663	310880	451	9729
1479 I4H3W 111-112	409	1071.177	47	5374	470	331816	465	7128
1479 I4H3W 131-132	410	1074.376	42	5137	430	332227	492	7015
1479 I4H4W 2-3	411	1077.964	74	8170	774	287476	551	9375
1479 I4H4W 22-23	412	1081.205	84	8027	747	293300	586	9202
1479 I4H4W 42-43	413	1084.437	91	9036	974	260829	620	10920
1479 I4H4W 62-63	414	1087.899	76	10838	995	248224	585	11539
1479 I4H4W 82-83	415	1091.377	85	14815	1088	241717	606	12046
1479 I4H4W 102-103	416	1094.816	61	9261	805	274440	464	11814
1479 I4H4W 122-123	417	1098.235	61	9223	800	271786	504	11697
1479 I4H4W 142-143	418	1101.757	79	10704	1070	241522	548	13415
1479 I4H5W 12-13	419	1105.260	45	29848	918	247554	506	13241
1479 I4H5W 32-33	420	1108.740	49	38949	914	230256	495	13211
1479 I4H5W 52-53	421	1112.143	63	19465	928	248636	500	12671

Appendix C – U1474 P_{EXT} data, 500 kya

Label Identifier	Sample No.	Age (kya)	Fe-Bound/Adsorbed P (ppm)	Authigenic P (ppm)	Detrital P (ppm)	Organic P (ppm)	Reactive P (ppm)	P _{EXT} (ppm)
1474 F1H1W 2-3	1	0.541	58	43	92	105	206	297
1474 F1H1W 12-13	3	3.243	57	56	51	74	187	237
1474 F1H1W 22-23	5	5.946	51	52	64	73	176	239
1474 F1H1W 32-33	7	8.649	59	71	58	78	208	266
1474 F1H1W 42-43	9	11.351	54	46	50	64	165	214
1474 F1H1W 51-52	11	13.784	59	40	61	84	183	244
1474 F1H1W 62-63	13	16.757	53	47	59	76	176	235
1474 F1H1W 72-73	15	19.459	49	44	49	109	201	250

1474 F1H1W 82-83	17	22.162	51	41	72	76	168	240
1474 F1H1W 92-93	19	24.865	52	72	43	63	187	230
1474 F1H1W 104-105	21	28.108	56	47	68	61	163	231
1474 F1H1W 112-113	23	30.270	53	68	63	64	185	248
1474 F1H1W 122-123	25	32.973	53	47	39	51	151	190
1474 F1H1W 132-133	27	35.676	52	61	42	58	171	213
1474 F1H1W 142-143	29	38.378	52	59	57	48	158	215
1474 F1H2W 4- 5	31	41.622	57	40	53	66	163	216
1474 F1H2W 13-14	33	44.054	54	59	52	54	168	220
1474 F1H2W 22-23	35	46.486	45	52	54	58	155	208
1474 F1H2W 32-33	37	49.189	53	53	44	60	166	210
1474 F1H2W 42-43	39	51.892	52	55	53	59	166	220
1474 F1H2W 52-53	41	54.595	46	51	50	70	167	218
1474 F1H2W 64-65	43	57.838	47	46	51	93	186	237
1474 F1H2W 72-73	45	60.000	11	46	60	62	120	180
1474 F1H2W 82-83	47	62.703	43	55	67	64	162	229
1474 D1H3W 12-13	49	84.324	53	52	55	65	170	225
1474 D1H3W 22-23	51	87.027	61	51	69	76	187	256
1474 D1H3W 32-33	53	89.730	53	57	60	49	159	219
1474 D1H3W 42-43	55	92.432	58	52	54	61	172	226
1474 D1H3W 52-53	57	95.135	50	49	69	53	152	220
1474 D1H3W 62-63	59	97.838	50	53	79	51	155	235
1474 D1H3W 72-73	61	100.541	49	38	131	70	157	288
1474 D1H3W 81-82	63	102.973	61	61	66	48	169	235
1474 D1H3W 92-93	65	105.946	55	50	143	54	159	302
1474 D1H3W 102-103	67	108.649	46	47	124	77	171	295
1474 D1H3W 112-113	69	111.351	46	42	102	81	168	270
1474 D1H3W 122-123	71	114.054	51	41	104	75	167	271
1474 D1H3W 132-133	73	116.757	38	33	96	43	114	209
1474 D1H3W 142-143	75	119.459	70	28	111	56	154	265
1474 D1H4W 2-3	77	122.162	45	45	122	59	149	271
1474 D1H4W 12-13	79	124.865	45	46	69	83	174	243
1474 D1H4W 22-23	81	127.568	46	58	66	41	145	210
1474 D1H4W 32-33	83	130.270	59	62	69	41	162	231

1474 D1H4W 43-44	85	133.243	70	50	53	49	168	221
1474 D1H4W 52-53	87	135.676	56	57	61	71	183	244
1474 D1H4W 62-63	89	138.378	53	31	114	67	151	265
1474 D1H4W 71-72	91	141.081	47	38	100	87	172	272
1474 F2H2W 110-111	93	156.757	33	48	54	48	129	182
1474 F2H2W 120-121	95	159.459	53	52	70	55	160	230
1474 F2H2W 130-131	97	162.162	45	45	138	63	153	291
1474 F2H2W 140-141	99	164.865	40	50	84	58	148	232
1474 F2H3W 2- 3	101	168.108	50	50	77	59	159	236
1474 F2H3W 12-13	103	170.811	49	51	113	82	182	294
1474 F2H3W 22-23	105	173.514	41	20	132	92	154	285
1474 F2H3W 31-32	107	175.946	38	43	113	99	180	293
1474 F2H3W 42-43	109	178.919	49	27	136	81	156	292
1474 F2H3W 52-53	111	181.622	43	45	92	7	94	186
1474 F2H3W 62-63	113	184.324	49	69	63	65	184	247
1474 F2H3W 72-73	115	187.027	38	68	106	47	153	259
1474 F2H3W 82-83	117	189.730	4	62	73	57	123	196
1474 F2H3W 92-93	119	192.432	39	52	65	61	153	218
1474 F2H3W 102-103	121	195.135	54	54	40	66	174	214
1474 F2H3W 112-113	123	197.838	48	53	38	53	154	191
1474 F2H3W 122-123	125	200.541	55	58	49	59	172	221
1474 F2H3W 132-133	127	203.243	48	66	36	51	165	201
1474 F2H3W 141-142	129	205.676	63	72	46	46	182	228
1474 F2H4W 2- 3	131	208.649	58	91	27	40	189	216
1474 F2H4W 42-43	133	219.459	54	50	35	55	158	194
1474 F2H4W 82-83	135	230.270	49	71	48	48	168	216
1474 F2H4W 122-123	137	241.081	40	50	29	48	137	166
1474 F2H5W 12-13	139	251.892	38	40	22	44	123	145
1474 F2H5W 52-53	141	262.703	64	65	21	36	164	185
1474 F2H5W 92-93	143	273.514	52	52	34	49	153	188
1474 F2H5W 132-133	145	284.324	57	55	29	47	159	188
1474 F2H6W 22-23	147	295.135	47	50	22	39	136	159
1474 F2H6W 62-63	149	305.946	59	39	30	50	148	178
1474 F2H6W 102-103	151	316.757	59	69	31	35	163	193

1474 D3H1W 132-133	153	346.486	53	59	34	46	159	194
1474 D3H2W 21-22	155	357.297	47	59	29	52	158	187
1474 D3H2W 82-83	157	373.514	47	53	32	51	152	183
1474 D3H2W 142-143	159	389.730	66	61	22	39	167	189
1474 D3H3W 32-33	161	400.541	42	52	26	46	139	165
1474 D3H3W 72-73	163	411.351	44	44	20	48	136	156
1474 D3H3W 112-113	165	422.162	45	52	20	42	139	159
1474 D3H4W 2-3	167	432.973	46	56	26	45	148	174
1474 D3H4W 41-42	169	443.514	56	68	25	47	171	197
1474 D3H4W 82-83	171	454.595	54	76	35	41	171	206
1474 D3H4W 142-143	173	470.811	65	91	29	36	192	221
1474 D3H5W 32-33	175	481.622	77	88	24	40	204	228
1474 D3H5W 72-73	177	492.432	58	90	23	35	183	206

Appendix D – U1479 PEXT data, 500 kya

Label Identifier	Sample Number	Calculated Age (kya)	Fe-Bound/Adsorbed P (ppm)	Authigenic P (ppm)	Detrital P (ppm)	Organic P (ppm)	Reactive P (ppm)	Total P (ppm)
361-U1479I-1H-1-W 3/4-LATI	1	0.784	67	77	13	170	313	326
361-U1479I-1H-1-W 13/14-LATI	3	3.205	76	72	13	207	354	367
361-U1479I-1H-1-W 23/24-LATI	5	5.627	67	79	11	120	266	277
361-U1479I-1H-1-W 33/34-LATI	7	8.023	62	64	8	110	235	243
361-U1479I-1H-1-W 43/44-LATI	9	10.381	61	79	11	103	244	255
361-U1479I-1H-1-W 53/54-LATI	11	12.272	67	85	16	102	254	270
361-U1479I-1H-1-W 63/64-LATI	13	13.825	49	94	15	84	227	242
361-U1479I-1H-1-W 73/74-LATI	15	15.220	59	94	15	78	231	246
361-U1479I-1H-1-W 83/84-LATI	17	16.576	54	110	18	79	243	260
361-U1479I-1H-1-W 93/94-LATI	19	17.973	50	116	19	75	241	260
361-U1479I-1H-1-W 103/104-LATI	21	19.451	50	118	24	50	219	242
361-U1479I-1H-1-W 113/114-LATI	23	21.080	45	119	24	64	228	252
361-U1479I-1H-1-W 123/124-LATI	25	22.874	39	121	21	63	223	244
361-U1479I-1H-1-W 133/134-LATI	27	25.149	50	96	13	56	202	215
361-U1479I-1H-1-W 143/144-LATI	29	28.253	64	84	17	101	250	267

361-U1479I-1H-2-W 3/4-LATI	31	31.850	48	87	15	61	196	211
361-U1479I-1H-2-W 13/14-LATI	33	35.656	52	73	14	60	185	199
361-U1479I-1H-2-W 23/24-LATI	35	39.447	43	71	10	59	174	183
361-U1479I-1H-2-W 33/34-LATI	37	43.012	58	66	10	50	174	185
361-U1479I-1H-2-W 43/44-LATI	39	46.285	57		12	53		
361-U1479I-1H-2-W 53/54-LATI	41	49.113	51	68	17	112	232	249
361-U1479I-1H-2-W 63/64-LATI	43	51.559	58	71	13	52	182	195
361-U1479I-1H-2-W 73/74-LATI	45	53.982	65	84	14	52	202	216
361-U1479I-1H-2-W 83/84-LATI	47	56.403	50	77	15	53	180	195
361-U1479I-1H-2-W 93/94-LATI	49	58.824	65	96	15	62	223	238
361-U1479I-1H-2-W 103/104-LATI	51	61.222	48	102	18	53	203	221
361-U1479I-1H-2-W 113/114-LATI	53	63.643	50	101	19	73	223	243
361-U1479I-1H-2-W 123/124-LATI	55	66.064	52	109	20	57	217	237
361-U1479I-1H-2-W 133/134-LATI	57	68.486	44	103	16	62	209	224
361-U1479I-1H-2-W 143/144-LATI	59	70.907	53	88	12	61	201	214
361-U1479I-1H-3-W 3/4-LATI	61	73.304	54	79	14	58	191	204
361-U1479G-1H-3- W 9/10-LATI	63	74.878	56	69	12	55	180	192
361-U1479G-1H-3- W 14/15-LATI	65	76.089	43	78	10	51	172	182
361-U1479G-1H-3- W 19/20-LATI	67	77.299	55	81	9	57	194	202
361-U1479G-1H-3- W 24/25-LATI	69	78.512	60	85	12	59	204	216
361-U1479G-1H-3- W 34/35-LATI	71	80.819	54	86	9	66	207	216
361-U1479G-1H-3- W 44/45-LATI	73	83.069	49	78	15	58	184	200
361-U1479G-1H-3- W 54/55-LATI	75	85.319	48	75	16	76	199	215
361-U1479G-1H-3- W 64/65-LATI	77	87.569	56	78	13	77	211	224
361-U1479G-1H-3- W 79/80-LATI	79	90.944	39	79	17	83	201	218
361-U1479G-1H-3- W 89/90-LATI	81	93.194	45	73	12	73	192	204
361-U1479G-1H-3- W 99/100-LATI	83	95.444	59	77	8	74	210	218
361-U1479G-1H-3- W 114/115-LATI	85	98.820	53	77	8	62	192	200
361-U1479G-1H-3- W 124/125-LATI	87	101.068	58	77	14	57	192	206
361-U1479G-1H-3- W 134/135-LATI	89	103.318	58	77	13	51	187	200
361-U1479G-1H-3- W 144/145-LATI	91	105.568	50	85	11	63	197	208
361-U1479G-1H-4- W 7/8-LATI	93	108.495	66	84	14	55	205	219
361-U1479G-1H-4- W 17/18-LATI	95	110.745	56	82	9	60	198	207
361-U1479G-1H-4- W 27/28-LATI	97	112.990	46	86	8	60	192	200

361-U1479G-1H-4-W 37/38-LATI	99	115.240	59	85	7	67	211	218
361-U1479G-1H-4-W 47/48-LATI	101	117.490	67	96	7	53	217	223
361-U1479G-1H-4-W 57/58-LATI	103	119.740	56	103	10	54	212	222
361-U1479G-1H-4-W 67/68-LATI	105	121.990	70	113	11	56	240	251
361-U1479G-1H-4-W 77/78-LATI	107	124.240	67	106	14	51	224	238
361-U1479G-1H-4-W 87/88-LATI	109	126.490	60	115	13	55	231	244
361-U1479G-1H-4-W 92/93-LATI	111	127.620	56	125	18	54	234	253
361-U1479G-1H-4-W 102/103-LATI	113	129.870	56	128	18	47	230	248
361-U1479C-2H-4-W 12/13-LATI	115	131.351	62	90	9	33	185	194
1479 G1H4W 117-118	117	133.240	52	121	28	54	227	255
1479 G1H4W 127-128	119	135.490	50	126	25	40	216	241
1479 G1H4W 132-133	121	136.620	44	127	42	37	208	249
1479 G1H4W 142-143	123	138.870	30	263	107	28	321	428
1479 C2H4W 52-53	125	140.283	49	73	9	40	161	170
1479 G1H5W 7-8	127	142.240	53	83	14	36	172	186
1479 G1H5W 17-18	129	144.490	48	79	19	29	156	175
1479 G1H5W 22-23	131	145.620	51	78	14	36	166	180
1479 G1H5W 32-33	133	147.870	57	84	14	30	171	185
1479 C2H4W 92-93	135	149.215	53	62	9	36	152	160
1479 G1H5W 47-48	137	151.240	61	85	20	33	179	199
1479 G1H5W 57-58	139	153.600	50	91	21	35	176	197
1479 G1H5W 62-63	141	154.890	53	97	16	37	187	204
1479 G1H5W 72-73	143	157.470	48	91	18	41	179	197
1479 G1H5W 77-78	145	158.760	49	110	20	40	199	219
1479 H2H1W 121-122	147	159.272	70	80	9	29	180	189
1479 H2H1W 127-128	149	160.787	55	69	13	39	163	175
1479 H2H1W 132-133	151	162.052	59	70	11	36	165	176
1479 H2H1W 137-138	153	163.318	55	75	14	35	165	179
1479 C2H5W 2-3	155	164.067	59	73	6	36	168	174
1479 G1H5W 102-103	157	165.200	94	90	19	47	231	250
1479 G1H5W 107-108	159	166.480	53	90	18	51	194	212
1479 G1H5W 112-113	161	167.770	51	99	20	55	205	225
1479 C2H5W 22-23	163	169.163	61	64	8	35	160	168
1479 G1H5W 127-128	165	171.640	53	94	20	38	184	204
1479 H2H2W 22-23	167	172.178	52	85	15	49	185	200
1479 C2H5W 41-42	169	174.288	61	73	8	34	169	177
1479 C2H5W 59-60	171	178.634	53	78	9	35	166	174
1479 C2H5W 82-83	173	184.513	57	95	13	31	182	196

1479 C2H5W 102-103	175	189.647	47	97	12	29	173	185
1479 C2H5W 119-120	177	193.970	59	101	13	25	185	198
1479 C2H5W 142-143	179	199.869	45	99	15	28	171	187
1479 C2H6W 12-13	181	204.966	49	97	25	28	174	199
1479 C2H6W 32-33	183	210.095	68	100	22	27	195	218
1479 C2H6W 52-53	185	215.201	50	74	15	24	148	163
1479 C2H6W 72-73	187	220.324	65	101	20	27	193	214
1479 C2H6W 92-93	189	225.448	58	123	31	31	212	243
1479 C2H7W 12-13	191	230.542	77	86	20	32	195	215
1479 C2H7W 31-32	193	236.276	60	89	23	29	178	200
1479 H2H4W 2-3	195	244.340	93	109	32	39	241	273
1479 H2H4W 42-43	197	252.252	46	124	31	36	206	237
1479 H2H4W 82-83	199	260.240	54	85	14	40	179	193
1479 H2H4W 119-120	201	267.696	55	87	22	39	181	202
1479 C3H1W 92-93	203	272.128	50	91	16	34	175	191
1479 H2H5W 7-8	205	275.420	47	83	22	39	169	191
1479 C3H1W 132-133	207	280.375	82	85	18	41	208	227
1479 C3H2W 19-20	209	288.252	58	88	20	32	178	198
1479 C3H2W 42-43	211	293.285	61	77	17	33	170	188
1479 C3H2W 82-83	213	298.138	58	86	17	33	177	194
1479 C3H2W 142-143	215	306.139	66	82	14	21	169	184
1479 C3H3W 32-33	217	311.677	55	117	14	22	194	208
1479 C3H3W 72-73	219	317.241	77	95	19	22	194	213
1479 C3H3W 112-113	221	322.792	60	78	18	22	160	179
1479 C3H4W 2-3	223	328.350	63	64	14	18	145	159
1479 C3H4W 42-43	225	333.896	79	61	15	18	159	174
1479 C3H4W 82-83	227	339.460	62	72	21	21	155	176
1479 H3H1W 97-98	229	343.600	72	72	15	27	171	186
1479 H3H1W 117-118	231	346.368	60	64	15	33	157	171
1479 H3H1W 137-138	233	349.295	81	79	13	32	193	205
1479 H3H2W 7-8	235	352.319	71	82	17	34	187	204
1479 H3H2W 24-25	237	354.888	55	91	15	33	179	195
1479 H3H2W 44-45	239	357.903	52	93	12	33	178	190
1479 H3H2W 64-65	241	360.927	69	90	11	32	191	203
1479 C3H5W 112-113	243	366.023	73	63	9	28	163	172
1479 C3H6W 2-3	245	372.083	70	63	11	32	165	176
1479 C3H6W 42-43	247	378.148	69	89	17	42	200	216
1479 C3H6W 82-83	249	384.215	52	99	12	32	182	194
1479 C3H7W 22-23	251	390.439	67	95	13	27	189	202
1479 C4H1W 148-149	253	426.250	62	122	23	37	221	244
1479 C4H2W 38-39	255	432.308	57	104	15	38	199	214